

1-1-2012

# Dynamic Response Of Concrete Rectangular Liquid Tanks In Three-Dimensional Space

Ima T. Avval  
*Ryerson University*

Follow this and additional works at: <http://digitalcommons.ryerson.ca/dissertations>



Part of the [Civil Engineering Commons](#)

---

## Recommended Citation

Avval, Ima T., "Dynamic Response Of Concrete Rectangular Liquid Tanks In Three-Dimensional Space" (2012). *Theses and dissertations*. Paper 1654.

# **DYNAMIC RESPONSE OF CONCRETE RECTANGULAR LIQUID TANKS IN THREE-DIMENSIONAL SPACE**

**Ima Tavakkoli Avval**

**B.Eng., Tabriz University, Tabriz, Iran, 2007**

A Thesis

presented to Ryerson University

in partial fulfillment of the

requirements for the degree of

Master of Applied Science

in the program of

Civil Engineering

Toronto, ON, Canada, 2012

©Ima Tavakkoli Avval 2012



I hereby declare that I am the sole author of this thesis.

I authorize Ryerson University to lend this thesis or dissertation to other institutions or individuals for the purpose of scholarly research.

Ima Tavakkoli Avval 

I further authorize Ryerson University to reproduce this thesis by photocopying or by other means, in total or in part, at the request of other institutions or individuals for the purpose of scholarly research.

Ima Tavakkoli Avval 

## **ABSTRACT**

# **DYNAMIC RESPONSE OF CONCRETE RECTANGULAR LIQUID TANKS IN THREE-DIMENSIONAL SPACE**

Master of Applied Science 2012

Ima Tavakkoli Avval

Civil Engineering

Ryerson University

The effect of three-dimensional geometry on the seismic response of open-top rectangular concrete water tanks is investigated. In this study, the fluid-structure interaction is introduced incorporating wall flexibility. Numerical studies are done based on finite element simulation of the tank-liquid system. The ANSYS finite element program is used. The liquid-tank system is modelled assuming both 2D and 3D geometries. Parametric studies are conducted to investigate the effect of water level, tank plan dimensions and the nature of the ground motion on the dynamic response. Due to three-dimensional geometry, amplification of the dynamic response in the form of sloshing height, hydrodynamic pressures and resultant forces is observed. The results show that, at the corner of the tanks, the interaction of the waves generated in longitudinal and transverse directions initiates greater wave amplitude. Sensitivity of the sloshing response of the tank to the frequency content of the ground motion is observed.

## **ACKNOWLEDGEMENT**

I wish to express my deepest gratitude to my supervisor Professor Reza Kianoush whose insight, guidance, meticulous review, and criticism of the work had a significant impact on this thesis. His inspirational attitude toward research, trust in his graduate students, and insight into the problems left a significant impression on this work. I cannot thank him enough as my life will always bear an imprint of his teachings and vision.

I would also like to thank the committee for their revisions and suggestions. I also wish to thank all my colleagues in the Civil Engineering Department at Ryerson University; especially Dr. Amirreza Ghaemmaghami for his help and support.

I am very grateful for the financial support provided by Ryerson University in the form of a scholarship.

Finally, I am forever indebted to my parents for giving me the support throughout my life. Also deep gratitude is expressed to my husband Payam for his strong support and encouragement. He gave me the support that I needed whenever I asked for.



# Contents

<b>1</b>	<b>Liquid Containing Structures</b>	<b>1</b>
1.1	General Overview . . . . .	1
1.2	Objectives and Scope of Study . . . . .	5
1.3	Organization of Thesis . . . . .	7
<b>2</b>	<b>Literature Review</b>	<b>9</b>
2.1	Introduction . . . . .	9
2.2	Importance of Liquid Tanks Performance under Ground Motion . . . . .	9
2.2.1	Damages to Liquid Containing Structures under Historical Ground Motions	11
2.2.2	Failure Mechanism . . . . .	12
2.3	Previous Research Studies . . . . .	13
2.4	Other Related Studies . . . . .	18
2.4.1	Damping Properties . . . . .	18
2.4.2	Design Codes and Standards for Liquid Containing Structures . . . . .	20
<b>3</b>	<b>Mathematical Background</b>	<b>30</b>
3.1	Introduction . . . . .	30
3.2	Numerical Simulation of the Liquid Motion in a Rectangular Tank . . . . .	31
3.2.1	Governing Equations . . . . .	31

3.2.2	Solution of the Equations for a Rectangular Tank Subjected to Horizontal Motion . . . . .	34
3.3	Equivalent Mechanical Models . . . . .	39
3.3.1	Parameters for the Mass Spring Model . . . . .	41
3.3.2	Parameters for the Pendulum Model . . . . .	44
<b>4</b>	<b>Finite Element Methodology</b>	<b>46</b>
4.1	Introduction . . . . .	46
4.2	Finite Element Modelling of the Coupled Systems . . . . .	47
4.2.1	Finite Element Modelling of the Tank Structure . . . . .	47
4.2.2	Coupling Matrix of Liquid-Tank System . . . . .	50
4.2.3	Finite Element Modelling of the Liquid Domain . . . . .	54
4.2.4	Solution of the Moving Liquid-Tank System in Time Domain . . . . .	58
<b>5</b>	<b>Dynamic Response of Rectangular Tanks: FEM Modelling, Results and Discussions</b>	<b>60</b>
5.1	Introduction . . . . .	60
5.2	Application of Finite Element Program . . . . .	62
5.2.1	Mesh Sensitivity . . . . .	65
5.3	Modal Analysis . . . . .	67
5.4	Time History Analysis . . . . .	72
5.4.1	Effect of Three-Dimensional Geometry on the Sloshing Height . . . . .	73
5.4.2	Sloshing at Tank Corners . . . . .	79
5.4.3	Effect of Earthquake Frequency Content . . . . .	86
5.4.4	Effect of Earthquake Frequency Content on Wave Interference . . . . .	89
5.4.5	Comparison of FEM Sloshing Heights with other Methods . . . . .	94
5.5	Hydrodynamic Pressure on the Walls . . . . .	100
5.5.1	Vertical Pressure Distribution . . . . .	100

5.5.2	Lateral Hydrodynamic Pressure Distribution . . . . .	104
5.5.3	Comparison of FEM Hydrodynamic Pressure with Analytical Approach	106
5.6	Base Reactions . . . . .	106
5.6.1	Base Shear . . . . .	109
5.6.2	Overturning Moment . . . . .	111
<b>6</b>	<b>Summary, Conclusions, Recommendations and Future Studies</b>	<b>115</b>
6.1	Summary . . . . .	115
6.2	Conclusions . . . . .	117
6.3	Code Recommendations . . . . .	119
6.4	Future Studies . . . . .	119

# List of Tables

2.1	Response modification factor $R$ . . . . .	25
2.2	Importance factor $I$ . . . . .	25
5.1	Selected tank configurations for this study . . . . .	63
5.2	Time periods and mass ratios for 3D Shallow tanks with $H_L = 5.5m$ . . . . .	69
5.3	Time periods and mass ratios for 3D Medium tanks with $H_L = 8.0m$ . . . . .	69
5.4	Time periods and mass ratios for 3D Tall tanks with $H_L = 11.0m$ . . . . .	70
5.5	Natural frequencies, time periods and mass ratios for 2D Shallow tanks . . . . .	71
5.6	Natural frequencies, time periods and mass ratios for 2D Medium tanks . . . . .	71
5.7	Natural frequencies, time periods and mass ratios for 2D Tall tanks . . . . .	71
5.8	Maximum sloshing height of 3D models conducted by FEM . . . . .	73
5.9	Maximum sloshing height of 2D models conducted by FEM . . . . .	74
5.10	Maximum sloshing height of 3D models subjected to Northridge earthquake . . . . .	93
5.11	Analytical sloshing height . . . . .	97
5.12	Design sloshing height according to ACI 350.5-06 . . . . .	97
5.13	Peak base force and moment at base of walls for the shallow tanks ( $H_L = 5.5m$ ) . . . . .	107
5.14	Peak base force and moment at base of walls for the medium height tanks ( $H_L = 8.0m$ ) . . . . .	108
5.15	Peak base force and moment at base of walls for the tall height tanks ( $H_L = 11.0m$ ) . . . . .	108

# List of Figures

1.1	Schematic illustration of the slosh wave . . . . .	4
1.2	Non-flexible wall to base connection . . . . .	6
2.1	Dynamic equilibrium of lateral forces of the tank . . . . .	26
2.2	Hydrostatic pressure $P_h$ distribution along the tank wall . . . . .	28
2.3	Hydrodynamic pressure distribution along the tank wall . . . . .	28
3.1	Coordinate system used for derivation of sloshing equations . . . . .	32
3.2	Pendulum-mass mechanical model representing different modes . . . . .	40
3.3	Mass-spring mechanical model . . . . .	40
3.4	Single convective mass model proposed by Housner . . . . .	43
4.1	An example of a system discretized to a finite number of elements . . . . .	49
4.2	A two-dimensional element at the fluid domain and structure domain interaction boundary . . . . .	51
4.3	Schematic illustration of liquid domain and boundaries . . . . .	55
5.1	Schematic configuration of the tank . . . . .	63
5.2	(a) Schematic 3D, 8-node iso-parametric element, (b) 3D model of a partially filled rectangular tank . . . . .	65
5.3	(a) 2D acoustic element, (b) Two dimensional model of a partially filled rectangular tank . . . . .	65

5.4	Finite element discretization error: (a) 2D shallow tank model (b) 2D tall tank model . . . . .	66
5.5	Mode shape related to the first fundamental mode of sloshing for a typical 3D model	67
5.6	First three sloshing mode shapes . . . . .	68
5.7	Mode shape related to the impulsive mode for a typical 3D model . . . . .	68
5.8	Horizontal components of El-Centro earthquake: (a) N-S, (b) E-W . . . . .	72
5.9	Time history of sloshing of TX40Y40: (a) 3D model, (b) 2D model . . . . .	75
5.10	Time history of sloshing of TX40Y60: (a) 3D model, (b) 2D model . . . . .	76
5.11	Time history of sloshing of TX40Y80: (a) 3D model, (b) 2D model . . . . .	76
5.12	Time history of sloshing of SX30Y60: (a) 3D model, (b) 2D model . . . . .	77
5.13	Time history of sloshing of MX30Y60: (a) 3D model, (b) 2D model . . . . .	78
5.14	Time history of sloshing of TX30Y60: (a) 3D model, (b) 2D model . . . . .	78
5.15	Sloshing height comparison between 3D and 2D models against $L/H_L$ . . . . .	79
5.16	Free water surface when the maximum sloshing occurs for a typical shallow tank	80
5.17	Time history of sloshing height for case SX20Y40 . . . . .	82
5.18	Time history of sloshing height for case MX20Y40 . . . . .	82
5.19	Time history of sloshing height for case TX20Y40 . . . . .	82
5.20	Time history of sloshing height for SX40Y40 . . . . .	85
5.21	Time history of sloshing height for SX40Y60 . . . . .	85
5.22	Time history of sloshing height for case SX40Y80 . . . . .	85
5.23	Scaled longitudinal components of earthquake records: (a) 1994 Northridge (b) 1940 El-Centro (c) 1957 San-Francisco . . . . .	87
5.24	Acceleration response spectrum of earthquake records: (a) 1994 Northridge (b) 1940 El-Centro (c) 1957 San-Francisco . . . . .	87
5.25	PSD function: (a) Northridge (b) El-Centro (c) San-Francisco . . . . .	88
5.26	Relative sloshing height: (a) SX30Y80, (b) MX30Y80, (c) TX30Y80 . . . . .	88

5.27	Time history of sloshing height of SX30Y80 . . . . .	90
5.28	Time history of sloshing height of MX30Y80 . . . . .	90
5.29	Time history of sloshing height of TX30Y80 . . . . .	90
5.30	Time history of sloshing height of SX30Y80 - Northridge . . . . .	92
5.31	Time history of sloshing height of MX30Y80 - Northridge . . . . .	92
5.32	Time history of sloshing height of TX30Y80 - Northridge . . . . .	92
5.33	Sloshing for MX30Y80 tank model - Northridge earthquake . . . . .	94
5.34	Acceleration response spectrum of scaled (N-S) El-Centro earthquake: (a) 0.5 % damping, (b) 5% damping . . . . .	96
5.35	Sloshing height for the tanks with $L = 20$ m (Group 1) . . . . .	99
5.36	Sloshing height for the tanks with $L = 30$ m (Group 2) . . . . .	99
5.37	Sloshing height for the tanks with $L = 40$ m (Group 3) . . . . .	99
5.38	Time history of sloshing for the small tank comparing FEM and experimental results . . . . .	100
5.39	Vertical hydrodynamic pressure distribution for SX30Y60 for 2D and 3D models	101
5.40	Vertical hydrodynamic pressure distribution for MX30Y60 for 2D and 3D models	102
5.41	Vertical hydrodynamic pressure distribution for TX30Y60 for 2D and 3D models	102
5.42	Vertical hydrodynamic pressure distribution for SX20Y80 for 2D and 3D models	103
5.43	Vertical hydrodynamic pressure distribution for MX20Y80 for 2D and 3D models	104
5.44	Vertical hydrodynamic pressure distribution for TX20Y80 for 2D and 3D models	104
5.45	Increase in 3D response in comparison with 2D in the form of peak hydrodynamic pressure against $L/H_L$ . . . . .	105
5.46	Hydrodynamic pressure distribution on the 3D tank model (case SX30Y60) . . .	105
5.47	Comparison of the hydrodynamic pressure distribution: (a) Shallow tank, (b) Medium tank, (c) Tall tank . . . . .	107
5.48	Time history of the base shear of SX40Y80: (a) 3D model, (b) 2D model . . . . .	109
5.49	Time history of the base shear of MX40Y80: (a) 3D model, (b) 2D model . . . . .	110

5.50	Time history of the base shear of TX40Y80: (a) 3D model, (b) 2D model . . . .	110
5.51	3D/2D peak base shear against $L/H_L$ . . . . .	111
5.52	Time history of impulsive and convective component of moment ( $M_y$ ) of SX20Y60: (a) 3D model, (b) 2D model . . . . .	113
5.54	Time history of impulsive and convective component of moment ( $M_y$ ) of TX20Y60: (a) 3D model, (b) 2D model . . . . .	113
5.53	Time history of impulsive and convective component of moment ( $M_y$ ) of MX20Y60: (a) 3D model, (b) 2D model . . . . .	114
5.55	3D/2D peak overturning moment against $L/H_L$ . . . . .	114

# Chapter 1

## Liquid Containing Structures

### 1.1 General Overview

Liquid containing structure is one of the critical lifeline structures, which has become very popular during the recent decades. Liquid containing structures (LCS) are used for sewage treatment and storage of water, petroleum products, oxygen, nitrogen, high-pressure gas, liquefied natural gas (LNG), liquefied petroleum gas (LPG), etc. There are many types of such storage tanks depending on the construction material, structure, content, volume and storage condition. Liquid storage tanks can be constructed by steel or concrete. It should be noted that due to excessive damages reported on steel tanks, the concrete storage tanks have become profoundly popular. Concrete tanks have higher initial capital costs than steel ones, but have lower lifetime operational costs. The economic lifetime of concrete or steel tanks is usually in the range of 40 to 75 years (ALA 2001). Concrete tanks can be constructed as ground supported or pedestal-mounted structures. In addition, ground-supported liquid-containing structures are classified based on the following characteristics: general configuration that classifies rectangular, spherical, and cylindrical tanks; wall-base joint type, which can be fixed, hinged, or flexible base; and finally, method of construction in the form of reinforced or pre-stressed concrete tanks.

For the environmental engineering structures such as water reservoirs and sewage treatment tanks, reinforced concrete (RC) has been used frequently. Concrete tanks are efficient structural systems since they can be easily formed in different sizes to meet the process requirements. While the cylindrical shape tanks may be structurally best for the tanks constructions, rectangular tanks are usually preferred. This is because rectangular tanks are more efficient and easier to be separated

into sub-tanks for different process purposes.

Concrete water tanks can provide critical city services. These structures are in demand for the storage of drinking water, fire suppression, agricultural farming and many other applications. Water tanks may provide services necessary for the emergency response of a community after an earthquake. It is worth mentioning that reinforced concrete tanks are designed for functionality during the normal life cycle; besides, RC tanks should withstand the earthquake loading without any excessive cracking. Their serviceability performance during and after strong earthquakes is of crucial concern. The failure of these structures may cause some hazards for the health of the citizens due to the resulting shortage of water or difficulty in putting out fires during an earthquake's golden time. As a result, many studies have concentrated on the seismic behaviour, analysis, and design of such tanks, particularly the ground supported ones.

In recent earthquakes, on-the-ground concrete rectangular tanks have been seen to be vulnerable structural elements and they have suffered considerable destruction, because their seismic behaviour has not been appropriately predicted. It should be noted that the seismic design of liquid storage tanks requires knowledge of fluid-structure interaction, natural frequencies, hydrodynamic pressure distribution on the walls, resulting forces and moment as well as the sloshing of the contained liquid. These parameters have direct effects on the dynamic stability and performance of the excited containers. In fact, the dynamic behaviour of water tanks is governed by the interaction between the fluid and the structure. Under strong ground motion, concrete tank walls may deform significantly and produce loads which are different from those of a geometrically identical rigid tank. Structure flexibility plays an important factor that should be addressed in investigation of tanks behaviour. On the other hand, soil-structure interaction and soil properties should also be introduced in the analysis process.

The effect of fluid interaction on the seismic response of the rectangular water tanks has been the subject of many studies in the past several years. Likewise, the effect of soil-structure interaction has been covered by many researchers. However, most of the studies are concentrated on the effect of fluid interaction on the cylindrical tanks, and only a small number of them are focused on the evaluating the effect of fluid interaction on the seismic response of the rectangular water tanks. Moreover, only few studies used the finite element method to predict this behaviour. Among others, Kianoush et al. (2010) and Livaoglu (2008) conducted intensive research on both of these topics.

It is worth to note that the dynamic response of the free liquid surface mostly depends on the type of excitation, peak acceleration, effective duration of the earthquake and its frequency con-

tent. Accordingly, it is necessary to consider the earthquake loading as a non-stationary random process. Livaouglu (2008) considered two earthquake records for a rectangular tank. Ghaemmaghami (2010) also conducted some research on the seismic response of rectangular rigid tanks subjected to four different acceleration inputs. Panchal et al. (2010) also investigated the seismic response of liquid storage steel tanks under normal component of six ground motions.

Other factors such as water level and tank plan dimensions also play important roles in the dynamic response of the rectangular tanks. Three-dimensional geometry and restraint conditions are also matters of crucial concerns that need to be addressed in the design procedure of the rectangular water tank. Koh et al. (1998) directed a thorough research study on the effect of the 3D restraint condition on the dynamic behaviour of the rectangular tank using boundary element method and finite element method (BEM-FEM). They also investigated the sloshing behaviour of the externally excited rectangular tank and compared their outcome with experimental test results.

In this study, sloshing characteristics of the rectangular tanks under horizontal ground motions are investigated. Note that, sloshing is defined as any motion of the free liquid surface inside its container and it is caused by any disturbance to a partially filled liquid container. The problems of liquid sloshing effects on large dams, water reservoirs, elevated water tanks, and oil tanks always have been matters of concern of civil engineers. The sloshing displacement of the fluid is extremely critical at the service level and for the design of tank roofs. However, its effect on the dynamic response tends to be less important compared to the other response parameters. Sloshing effect is occasionally ignored in the simplified analysis. It should be noted that the liquid surface in a partially filled container can move back and forth at an infinite number of natural frequencies, but it is the lowest few modes that are most likely to be excited by the ground motion. Figure 1.1 shows a schematic illustration of the slosh wave in a tank. The shaded area indicates the expected shape of the free surface at its fundamental mode of sloshing. It should be noted that sloshing at the fundamental frequency mobilizes the largest amount of liquid, and may produce excessive structural loads that can lead to structural failure.

## **Analysis Methods**

Different methods are employed to predict the dynamic response of an externally excited tank; simplified method, response-spectrum mode superposition method and time domain analysis. In this section, these methods will be described briefly.

Simplified procedures are used for preliminary estimates of stresses and section forces due to

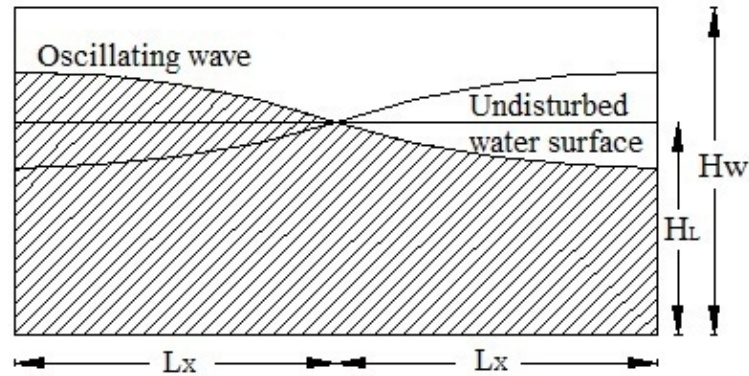


Figure 1.1: Schematic illustration of the slosh wave

earthquake loading. The traditional seismic coefficient is one such procedure employed primarily for the analysis of rigid or nearly rigid hydraulic structures. In this procedure, the inertia forces of the structures and the added mass of water due to the earthquake shaking are represented by the equivalent static forces applied at the equivalent centre of gravity of the system. Note that if the water is assumed to be incompressible, the fluid-structure interaction for a hydraulic structure can be represented by an equivalent, added mass of water. The inertia forces are simply computed from the product of the structural mass or the added mass of water, times an appropriate seismic coefficient in accordance with design codes. This assumption is generally valid in cases where the fluid responses are at frequencies much greater than the fundamental frequency of the structures. These approximations are described by Westergaard (1938), Housner (1957) and Chopra (1975).

When a structure is subjected to external ground motion, the motion is generally described by a specific response-spectrum. Response-spectrum mode superposition method is currently used in National Building Code of Canada (2010). This method provides a simplified formulation for the maximum dynamic responses and the vertical displacement of the water in a single or multi degree of freedom (DOF) system, with small damping ratio. In modal superposition method, for a multi DOF system, the response due to a base motion corresponding to each mode may be evaluated by applying the earthquake response-spectrum at the natural frequency corresponding to the mode. The modal responses can be combined using Square Root of Sum of Squared (SRSS) method or employing the Complete Quadratic Combination (CQC) method. The SRSS method provides a good estimation when the modes are well separated. Otherwise, the CQC method may be used for the correlation between closely spaced modes. Finally, the responses from each component of the ground motion can be combined employing either the SRSS or CQC method for the multi component excitations. However, there are some limitations that should be considered in the modal analysis. First of all, the time dependency characteristics of the ground motion cannot

be introduced. In addition, all the responses such as forces, moment, stress, and displacement calculated using modal analysis are positive and non-concurrent; therefore, deformed shape of the system cannot be predicted. Also, in this method, structure-foundation interaction cannot be completely addressed in this method.

Finally, the time domain analysis is used to avoid any limitation confronting in other methods. This method addresses the time dependent response of the structure and better represents the fluid-structure interaction. In this method, the external ground motion is usually presented in the form of the ground acceleration time history. Response history of the structure is also calculated in the time domain. This method is an ideal way to introduce the time dependency characteristic of the ground motion and structural responses. Parameters such as duration of the ground motion, numbers of the sub-steps, and presence of high energy pulses can be introduced in the time domain analysis.

## **1.2 Objectives and Scope of Study**

In spite of a wide range of studies on the dynamic response of the liquid containing structures, many parameters need to be addressed for a better design of the rectangular tanks. Additional factors that should be directed include wall flexibility, three-dimensional geometry, direction of the ground motion and the full time-domain simulation. In this context, the primary objectives of the present report are to investigate some of such effects to improve the design procedure of the seismically excited rectangular tanks:

1. The effect of 3D geometry on sloshing height
2. The wave amplitude at the critical locations of the three-dimensional tanks for free-board design
3. The sloshing height at the corner of the 3D tanks subjected to the multi component excitation
4. The effect of the frequency content of the ground motion on the wave amplitude in the rectangular tanks
5. The effect of three-dimensional geometry on the hydrodynamic pressure and structural responses

During strong earthquakes, flexible tank walls may deform significantly and may initiate loads higher than that of identical case of the rigid tank. Therefore, flexibility of the wall is addressed in this study to predict the dynamic response of the 3D rectangular tank. It should be noted that this study is limited to the linear elastic analysis of the open-top rectangular tanks anchored at the base and filled with water. Figure 1.2 illustrates the schematic base configurations of the fixed base tanks. In this study, tanks walls are considered to have constant thickness and the uncracked section properties are used. It should be noted that the behaviour of tank with cracked section properties result in minor changes in convective terms and the sloshing behaviour is almost independent of the flexibility characteristics of the side walls.

For this purpose, finite element method will be used to predict the response of the seismically excited rectangular tanks. The finite element program, ANSYS (ANSYS Inc., 2010), with fluid-structure interaction analysis capabilities is used for the dynamic modal and time history analysis.

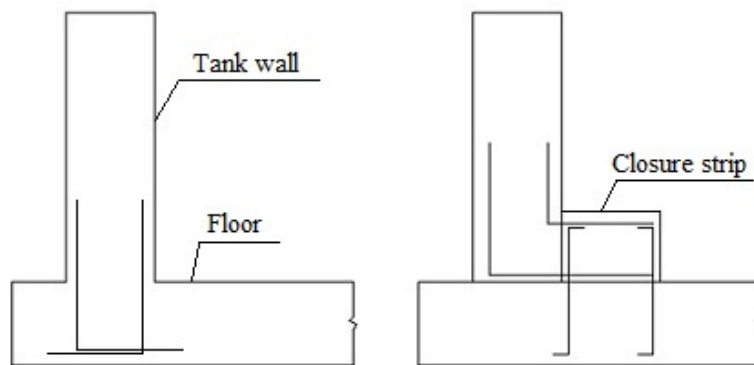


Figure 1.2: Non-flexible wall to base connection

In order to evaluate the dynamic response of the containers, several goals were set; first to introduce an improved finite element method (FEM) model; second to employ more realistic methods of representing structural behaviour, and finally to employ more reasonable simulations of transient loads. Parametric studies are conducted to investigate the effect of different factors such as tank plan configuration, water depth, and ground motion frequency content on the dynamic response of the three-dimensional water tanks. The sloshing displacements of the 3D tank models, as well as the hydrodynamic pressure and the structural reactions, are calculated. These values are also calculated, and comparisons are made with the corresponding 2D simulations. For a three-dimensional rectangular tank subjected to multi component ground motion, sloshing height is calculated at the corner of the tank, and is compared with the slosh heights at other locations. To

verify the proposed FE model, the structural responses and hydrodynamic pressures are compared with the results conducted by analytical approaches for specific cases. In addition, the sloshing profile is also compared with results of the experimental test available in the literature.

It should be noted that, in this study, small wave amplitude or linear wave theory is used for evaluating the seismic performance of the LCS. However, there are some assumptions and limitation in this theory for simulation of the actual behaviour of the sloshing. Note that the vertical component of the ground acceleration only causes an insignificant effect on the surface elevation and hydrodynamic pressure. Because of the expected stiffness of these structures in the vertical direction, the effects of the vertical component of the ground acceleration are ignored.

In the current practice, 2D models are used to evaluate the dynamic response of the tanks; however, 3D models represent a more realistic simulation and usually predict higher value of the structural responses. The result of the present work can be used for code and standard developments. It is an approach to identifying and reducing the risks of disaster, and it will aim to reduce social-economical vulnerabilities to earthquake.

### **1.3 Organization of Thesis**

This thesis is divided into 6 chapters. In chapter 1, in addition to general description of the liquid containing structures and the brief discussion on the LCS analysis methods, the scope and objectives of the present work are described.

In chapter 2, the importance of the seismic performance of the LCS, as well as some reported damages on these structures during historical earthquakes, are discussed. Reported failure mechanisms of the LCS are also discussed. Previous research studies on the dynamic responses of the LCS and other related studies such as damping characteristic of the system, as well as the current codes and standards, are presented in chapter 2.

Mathematical backgrounds on the dynamic responses of the rectangular liquid tanks are presented in chapter 3. The numerical formulation of the sloshing wave, and the solutions of the equations of the motion are described. Also, the equivalent mechanical models are described in chapter 3.

Finite element formulation of the tank structure and equation of motion for the structure domain, as well as the calculation of the coupling matrix for the tank-liquid system, are discussed in chapter 4. In addition, finite element simulation of the liquid domain and derivation of equation

of motion is offered in in chapter 4. Finally, FEM formulation of the tank-liquid system is derived in two and three-dimensional space.

Application of FEM and modelling of the system using ANSYS program and mesh sensitivity of the models are described in chapter 5. Then, the results of the modal analysis as well as time history analysis of the rectangular tanks are offered. In chapter 5, the effect of the three-dimensional geometry on the sloshing height of water is shown. The sloshing heights are presented for different tank plan configuration at critical points. The sloshing heights calculated by 3D models are compared with the corresponding sloshing height that are calculated employing 2D models. Finally, the effect of the frequency content of the ground motion on the sloshing response of the rectangular tank is discussed. Later, the comparison of the results of the 3D and 2D models inform of the hydrodynamic pressure and structural responses are discussed. A detailed comparison between current finite elements results and other available methods in literature is given in chapter 5. Three-dimensional impulsive pressure distributions are also illustrated in this chapter.

A summary and major conclusions as well as some recommendation for the design procedure of the rectangular water tanks are described in chapter 6. Some recommendations for further studies are also presented.

# **Chapter 2**

## **Literature Review**

### **2.1 Introduction**

In this chapter, a literature review on seismic response of liquid storage tanks is presented. The previous research related to dynamic behaviour of the rectangular water tank and sloshing characteristic of externally excited tanks are presented.

The performance of liquid tanks under earthquakes and some reported damages are presented hereby. The failure mechanisms of the LCS under strong ground motions are described in section 2.2.2. Significant contributions from past studies are described in section 2.3. Finally, some other related information is presented, as this subject links to many engineering fields. The design codes and other special topics including damping properties of the system are introduced in section 2.4. Overall, the intention of this chapter is to provide an overview of the dynamic behavior of liquid storage tanks under earthquakes.

### **2.2 Importance of Liquid Tanks Performance under Ground Motion**

The concept of disaster management is not a relatively new strategy in Canada. The idea historically was focused on the distribution of relief after a disaster, rather than capitalizing programs of vulnerability assessment and mitigation to reduce losses before a disaster occurs. However, the

contemporary pattern is capitalizing programs of the vulnerability assessment and moderation to reduce losses before a disaster. The contemporary pattern of disaster management and disaster risk reduction represents the latest achievements. Disaster risk reduction is defined by the United Nations International Strategy for Disaster Reduction as (UNISDR, 2004):

"The conceptual framework of elements considered with the possibilities to minimize vulnerabilities and disaster risks throughout a society, to avoid (prevention) or to limit (mitigation and preparedness) the adverse impacts of hazards, within the broad context of sustainable development."

Reinforced concrete liquid storage tank is one of the imperative life-line environmental engineering structures, which have become very widespread in recent decades. These structures are widely used for storing or treating water, waste water, or other liquids and non-hazardous materials such as solid waste, and for secondary containment of hazardous liquids or harmful solid waste. Liquid tanks are exposed to a wide range of seismic hazards and interaction with the other sectors of environment. Heavy damages can be caused by strong earthquakes; consequently the dynamic response of water tanks is the matter of special importance.

Without assured emergency water source after major earthquakes, uncontrolled fires may occur and cause more damages than the earthquake, as occurred back in 1906 in a great earthquake in San Francisco. At that time, the water mains were broken, and the fire department had few resources to fight the fires. Ninety percent of the destruction in San Francisco earthquake was caused by the fires than the earthquake itself (U.S. Geological Survey, USGS, 2012). One lesson learned from this disaster was the importance of the water supply for firefighting purposes.

In addition, safe and clean water supply is crucial instantaneously after earthquakes for preventing plague of diseases. Equally, as the case of tanks containing harmful liquids, extra attention should be given to prevent more harm to the environment and avoid catastrophes. Moreover, in nuclear power plants, sloshing displacement is one of the principal design criteria. In these structures, slosh height is profoundly critical to fix the inlet pipe levels in pressure suppression pools of boiling water reactors to prevent the escape of super-heated steam.

### **2.2.1 Damages to Liquid Containing Structures under Historical Ground Motions**

Severe damages have been reported from past earthquakes; however, little knowledge is available on the dynamic response of the rectangular concrete tanks. The major historical earthquake that caused significant damages to the liquid retaining structures that led to development of the seismic design codes and standards of tanks are discussed here.

The fire that occurred as a result of the 1964 Niigata Earthquake in Japan, lasted for more than 14 days consuming around 122 million litres of oil. Investigations about the causes of this fire led to the conclusion that friction between the roof and sidewall of the storage tank led to sparking. The seal material between the roof and the sidewall was metallic, and it was the seal that led to sparking when it scraped against the side wall. These sparks ignited the petroleum vapour contained inside the tank, leading to a huge fire (Kawasumi, 1968). In 1964, the earthquakes occurred in Alaska and the one happened in Niigata ended to significant losses of oil storage tanks (National Research Council U.S., 1968). Those events brought attention of many seismic engineering societies. Researcher concentrated to work on diverse methods to improve the performance of the oil storage tanks, specially petroleum storage tanks, under seismic loading.

Then again, another earthquake occurred in 1971 in San Fernando caused notable destruction to water and waste water treatment systems in Sylmar and Granada Hills areas. Failure of a welded steel water tank was also reported; in that case, the over loaded stresses due to foundation failure and differential settlements initiated a horizontal buckle in the shell plate. An underground water reservoir was subjected to an estimated inertial force of 0.4g and suffered severe damages in terms of the collapse of the wall. Moreover, sloshing water caused by earthquake resulted in notable movement of a steel wash water tank in Sylmar area. Mentioned damages in 1971 in San Fernando led to adoption of more strict criteria for the seismic design of liquid storage tanks. As a result, when later in 1994 similar magnitude earthquake happened in California only minor damages were reported on the lifeline structures. Also, the Northridge earthquake caused extensive damage to some major lifeline facilities in the Los Angeles area (USGS, 2012).

Some damages also reported caused by loss of foundation support as happened on January 17, 1995 near the port city of Kobe in Japan. Liquefaction was the major reason of damages at waterfront locations. Similarly, in Bhaji Indian earthquake of 2001, many elevated tanks suffered damages to their support failure (USGS, 2012).

Moreover, in Turkey after the earthquake took place in 1999, many liquid retaining tanks and

petrochemical plants were damaged due to the fires as indirect consequences of the shocking ground motion (USGS, 2012).

### **2.2.2 Failure Mechanism**

Failure mechanism reported on storage containing structures depends on different factors such as configuration of the tank, material of construction, and supporting system. Any of these factors themselves depend on various parameters. Configuration of the tank usually depends on the usage purpose while it can be circular, rectangular, cone or other shapes. About material of construction most common materials are steel and concrete. Concrete tanks can be cast-in-place, prestressed or post-tensioned, so the method of construction also matters. The next contributing factor is the supporting system, as the tank can be anchored or unanchored into the foundation. It is worth mentioning here that liquid containing concrete tanks are designed for serviceability, and leakage beyond the limit will be considered as failure of the structure.

The American Lifelines Alliance (ALA 2001) presents different modes of failure that have been observed in tanks during past earthquakes. These failure modes include:

- Buckling of the Shell: caused by axial compression due to overall bending or beam-like action of the shell that mostly happens in steel cylindrical tanks
- Roof damage: caused by excessive convective pressure due to sloshing of the upper part of the contained liquid and happens in absent of sufficient free board
- Anchorage failure: fracture of wall-base connection due to up-lift in partially restrained or unrestrained tanks
- Tank support system failure: specifically happens in case of elevated tank due to heavy mass on top of concrete frame or pedestal. The concrete frame may crack or collapse due to lateral forces caused by earthquake, moreover over turning moment can cause surplus tension force on one side of the concrete pedestal
- Foundation failure: can happen for both concrete and steel tank due to foundation failure or differential settlement
- Hydrodynamic pressure failure: seismically loaded tanks can experience excessive hydrodynamic pressure; also massive inertial forces resulting from self-weight of the structure

causes additional stresses, which may lead to leakage in concrete tanks and/or even collapse of the structures

- Leakage in the connection between the reservoir and adjoining walls and vertical cracks in expansion joints
- Loss of prestressing in prestressed concrete tanks: loss of stress in reinforcing tendons or warped wires
- Failure of connection between the tank and piping system or other accessory systems.

Earthquake damages and failure modes caused by different earthquakes were also analyzed by Kobayashi (1986) and summarized in three categories as follows:

1. For tanks with capacities more than  $5000m^3$ , more damages and failures caused by liquid sloshing and were observed in the roof and shell walls.
2. In case of tanks with less than  $5000m^3$  capacities, most of damages and failures, due to liquid sloshing, were observed in the lower parts.
3. Much damage and failures caused by inertia forces and overturning moments were reported around the corner joints of the shell wall plate and bottom plate.

Also, according to field reports, liquid storage tanks were mainly damaged either by excessive axial compression due to overall bending of the tank shell or by the sloshing of the contained liquid with insufficient free-board between the liquid surface and the tank roof.

## **2.3 Previous Research Studies**

As mentioned previously, the dynamic response of the liquid containing tanks is considerably associated with the fluid-structure as well as the soil-structure interaction. Studies on the fluid-structure interaction can be found in the literature on the seismic design of concrete gravity dams or arch dams. The seismic design of dams and that of the liquid storage tanks both involve fluid-structure interaction; however, the dam problem differs from the tank problem in the following points:

- In the dam problem, the associated fluid domain is very large, consequently, modelled as a semi-infinite region. While, the tank problem deals with a finite fluid region of relatively small volume.
- The compressibility of the fluid is known as to having significant effects on the dynamic response of dams; however, it is not the case in most tank problems.
- The surface wave effects are usually neglected in the dynamic analysis of dams; on the other hand, the sloshing response is an important consideration in the seismic analysis of the storage tanks, particularly for storage tanks of nuclear spent fuel assemblies.

The nature of sloshing dynamics in cylindrical tanks is better understood than of the prismatic tanks. Few studies on the dynamic response of rectangular containers exist; unfortunately, in those studies such as the ones by Housner (1957, 1963) and Haroun (1984), some limitations exist and the flexibility of the structure is not entirely accounted. This may be due to the fact that rectangular fluid containers are usually made of reinforced or prestressed concrete and may be considered quite rigid dynamically. Yet, as stated by Luft (1984), for very large reinforced concrete pool structures used for the storage of nuclear spent fuel assemblies or prestressed concrete water tanks, flexibility must be taken into account in the dynamic response analysis. Because, under strong ground motion, flexible tank walls may undergo significant deformation. As a result, the loads produced is different from that of rigid tank.

Housner (1963) proposed a widely used analytical model for circular and rectangular rigid tanks. In his work, the hydrodynamic pressures were separated into impulsive and convective components. The impulsive component is the portion of the contained liquid that moves unison with tank structure and convective component is the portion of the liquid that experiences sloshing. In their model, fluid was assumed incompressible and the walls were assumed to be rigid. Housner's theory has then served as a guideline for most seismic designs of liquid storage tanks. However, failures of liquid storage tanks during past earthquakes suggested that Housner's theory may not be conservative. Haroun (1984) presented a detailed, analytical method for rectangular tanks. In his work, the hydrodynamic pressures were calculated using classical potential flow approach assuming a rigid wall boundary conditions.

The first finite element method for evaluating the seismic behavior of flexible tanks was proposed by Edward (1969). Merten and Stephenson (1952), Bauer in (1958,1969), and Abramson et al (1962) also studied the liquid-elastic container coupling within the limit of the linear theory of small oscillations and determined the natural frequencies and mode shapes. Beam and Guist

(1967) also reported that, for a thin elastic tank wall, the coupled frequency for the fundamental axis-symmetric mode is much smaller than the liquid frequency with rigid walls. The influence of wall oscillations on the liquid governing equations was examined by Ohayon and Felippa (1990).

Arya et al. (1971) studied the dynamic behaviour of the tanks that are fixed at the base and free at the top. In their research, virtual mass due to the liquid was considered, but sloshing effect was ignored. Later, Veletsos (1974) and Veletsos and Yang (1976,1977) presented solutions for the dynamic pressure and impulsive mass under the assumption of certain deformation patterns of tank walls. They assumed that the tank behaves as a cantilever beam and considered a deformed shape of the tank system. The fluid-tank system was treated as a single degree of freedom system in terms of the lateral displacement of the tank at the free surface level. The fluid inertial effect was considered by an added mass concept in which an appropriate part of fluid mass is added to the structural mass. The study was limited only to the impulsive component. A comprehensive overview of the hydrodynamic forces on the tanks under the assumed deformation pattern, the vibrational behaviour of the empty tanks, and the application of those results to interacting system of water tank was also presented by Yang (1976).

Aslam (1981), presented finite element analysis to estimate the earthquake induced sloshing in axisymmetric tank. The hydrodynamic pressure in the liquid tanks subjected to ground motion was studied; however, in their study, the tank was assumed to behave as a rigid body.

Park et al. (1990) performed research studies on dynamic response of rectangular tanks. They used the boundary element method to calculate the hydrodynamic pressures and finite element method to analyze the solid wall. The governing equation for the coupled system was given. The time history analysis was used to obtain the dynamic response of fluid storage tanks. Both impulsive and convective effects were considered.

Subhash Babu and Bhattacharyya (1994) developed a numerical scheme based on finite element method to estimate the sloshing height in the seismically excited tank and to calculate the resulting pressure. They developed the numerical code introducing fluid-structure interaction in two-dimensional space.

Koh et al. (1996) developed a coupled BEM-FEM to analyze the dynamic response of 3D rectangular tanks subjected to horizontal ground excitation. They employed an approach with a detailed description of the behaviour of the structure accomplished by finite element modelling. The motion of the homogeneous fluid region was described with a very small number of degrees of freedom, by boundary element modelling (BEM). In Koh's work, the free-surface sloshing

motion was included within the limit of linearized boundary condition.

Kim et al. (1998) concluded that the effect of free-surface sloshing motion on the dynamic response of the flexible structure can be insignificant; however, the sloshing motion itself may be amplified due to the flexibility of the wall in rectangular tanks. They suggested that the 3D restraint condition has a significant effect on the dynamic response of the externally excited tanks. They concluded that the 3D geometry may cause substantial amplification on the systems responses in the forms of hydrodynamic pressures and structural reactions. However, in their study, only pair of walls orthogonal to the direction of the applied ground motion was assumed to be flexible, and the other pair was assumed rigid.

Choun and Yun (1998) also studied the sloshing response of rectangular tanks considering linear wave theory. In their study, the tanks subjected to horizontal ground motion had a submerged structure. As specified by Choun et al., the sloshing response of the fluid-structure system is very sensitive to the characteristics of the ground motion and the configuration of the system. They concluded that, for the ground excitation dominated by low-frequency contents, the sloshing response increases significantly; additionally, the contribution of the higher sloshing modes also increases.

Pal et al. (1999) were also among first to use finite element method for the numerical simulation of the sloshing response of laminated composite tanks. They applied the solution procedure to both flexible and rigid containers to demonstrate the effect of wall flexibility on the overall sloshing behaviour and structure response.

Premasiri (2000) also completed a concentrated research on the sloshing in the reservoirs subjected to multi DOF base motion. Comparing the result of experimental test on the rectangular tanks subjected to multi DOF base motion, with the analytical solution using linear superposition method.

Akyildiz et al. (2006) investigated the three-dimensional effects on the liquid sloshing loads in partially filled rectangular tanks by introducing non-linear behaviour and damping characteristic of the sloshing motion using Volume of Fluid (VOF) techniques. They observed the effect of factors such as tank plan configuration, water level, amplitude of excitation and the frequency content of the ground motion on the sloshing pressure.

Arafa (2006) developed finite element formulations to investigate the sloshing response of horizontally excited rectangular tanks. His work was limited to discretizing the liquid domain into two-dimensional four-node elements, with the liquid velocity potential being the nodal degrees

of freedom. In his work, fluid-structure interaction was included in the model to couple the liquid motion with the rigid tank walls. In order to include the rigid enclosure in the finite element formulation, three spring-supported pistons were attached to the liquid domain.

Livaoglu (2007) also investigated the effect of parameters such as fluid-structure interaction, soil-structure interaction and presence of embedment on the dynamic responses of rectangular tanks. He concluded the substantial effect of SSI on the sloshing response of the tank; especially for flexible tanks. He also noted that the flexibility of the tank wall and FSI can significantly impact the structural responses in the form of base shear.

Virella et al. (2007) also investigated both linear and nonlinear wave theory on the sloshing natural periods and their modal pressure distributions for rectangular tanks. The study was with the assumption of two-dimensional behaviour. In their study, the finite element method was employed and again the tank was assumed to be rigid; therefore, there was no elastic interaction between the tank and the liquid.

Ghaemmaghami and Kianoush (2010) conducted intensive research on the dynamic time-history responses of the rectangular tanks. In their study, the responses of the rigid tanks were compared with the identical case of flexible tank. Significant amplifications in the structural responses were perceived. They also investigated the effect of the 3D geometry for one case of shallow tank as well as a tall tank. The effect of vertical acceleration on the dynamic response of the liquid tank was found to be less significant when the horizontal and vertical, when both components of the ground motion considered together.

With a critical point of view to the previous studies, one can clearly notice that there are different factors that need to be addressed for the dynamic analysis of rectangular tanks. It is worth to explore the effect of the 3D geometry on the responses of the structure within the form of a more intense research. The effects of parameters such as variable tank plan dimensions, water level, amplitude and nature of the base motion on the sloshing profile, as well as structural responses, need further examinations.

## 2.4 Other Related Studies

### 2.4.1 Damping Properties

In liquid contained structures, the motion of the liquid decays due to damping forces created by viscous boundary layers. The damping of liquid sloshing is usually caused by the viscous dissipation at the rigid boundary of the container, viscous dissipation at the free surface associated with breaking waves, by the viscous damping in the interior fluid, and finally by capillary hysteresis at a contact line.

The reduction of the peak hydrodynamic forces due to energy dissipation is very necessary to be defined. However, calculation of viscous damping is a very difficult procedure and only can be estimated from laboratory or field tests on the structure. In most cases, modal damping is used in the computer model to visualize the nonlinear energy dissipation of the structure. Also, a very common way to introduce damping in the analysis of the structure is to assume that damping is proportional to mass and stiffness, like Rayleigh damping method. This method reduces the difficulties of applying the damping matrix based on the physical properties of the structure. It should be noted that Rayleigh damping varies with frequency; whereas, modal damping is constant for all frequencies.

Rayleigh damping is a classical method for constructing the damping matrix,  $C$ , of a numerical model, using the following equation:

$$C = \alpha M + \beta K \quad (2.1)$$

where  $C$  is called Rayleigh damping matrix and is proportional to the mass matrix,  $M$ , and to the stiffness matrix,  $K$ .

In mode superposition analysis, in order to decouple the modal equations, the damping matrix should satisfy following properties:

$$2\omega_n \zeta_n = \phi_n^T C \phi_n \quad (2.2)$$

Therefore, for Rayleigh damping, damping ratio  $\zeta$  can be defined as:

$$\zeta = \frac{\alpha}{2 \omega_c} + \frac{\beta \omega_i}{2} \quad (2.3)$$

where damping ratio  $\zeta$  is a function of the natural frequencies also the Rayleigh damping coefficients  $\alpha$  and  $\beta$ . Note that in Eqn.2.3,  $\omega_i$  and  $\omega_c$ , respectively, correspond to the natural frequencies of impulsive and convective modes.

Equation 2.3 produces a curve that can be modified for modal damping values at one or two natural frequency points. Therefore, Rayleigh damping can resemble the behaviour of the modal damping of the liquid tank, as this coupled system has two very dominant frequencies.

Notably damping characteristic of a structure has a significant effect on its response to the ground motion. The presence of small amplitude of damping can reduce the stresses, forces, and the whole seismic response of the structure. In general, reinforced concrete structures have higher damping ratio than steel structures. Because the internal damping available in elastic steel structures is largely associated with inelastic action, that occurs less in a welded steel structure, and more in reinforced concrete. Damping properties of concrete liquid tanks are generally expected to be of the order of 5% for the impulsive mode.

Essentially, damping depends on the tank geometry, kinematic viscosity of the liquid and liquid level. On the other hand, Mikishev et al. (1961) showed that, in the storage tanks with rational dimensions, viscous damping is approximately 0.5%. ACI 350.3-06 (2006) also specifies the damping of 0.5 to 1 percent of the critical damping for the sloshing water. The damping ratio of 0.5% used for the convective component is similar in all codes and standards. While, damping ratio for impulsive component of pressure in the liquid tanks is different in various codes and standards. Basically, the impulsive damping ratio depends on the type of the tank, construction, material, etc. ASCE 7 standard, the same as the ACI350.03-06 code, defines a value of 5% damping ratio for the impulsive component of all kinds of tanks. As a result, the corresponding response spectral acceleration is 1.5 times lower than that of convective components. On the other hand, Eurocode 8 defines a value of 5% damping ratio for the reinforced and prestressed concrete tanks but 2% for the steel tanks; thus, the response spectral acceleration of the impulsive component is 1.7 times lower than that of convective pressure. New Zealand Standard (NZS 3106-1986) also employs variable damping ratio for the impulsive component depending on tank material, aspect ratio of the geometry, etc.

The additional effects of radiation damping can also be considered, particularly for larger tanks resting on a soft ground. The vibration of the structure strains the foundation material near the

supports and causes stress waves to emerge into the infinite foundation. This interaction considerably reduces the level of earthquake response. In this study, the tanks are assumed to be fixed to a rigid foundation and radiational damping is not considered.

## **2.4.2 Design Codes and Standards for Liquid Containing Structures**

Canadian design standards do not directly deal with the structural design of environmental concrete structures. However, a variety of other standards is available, such as; American Concrete Institute (ACI 350.3-2006), Eurocode-8 (Eurocode-8 1998), American Water Works Association (AWWA D-115 1995), New Zealand Standard (NZS 3106 1986), British Standard 8007 (BS 8007 1987). It may be noted that some of these codes deal with only specific types of tanks. The design code presented by American Concrete Institute (ACI 350.3-06) is one of the most comprehensive and preferred standards. Hereby, the procedure to calculate the dynamic properties of the excited rectangular tank as well as the pressure distribution and resulting forces and moment will be described. It should be noted that procedures for the seismic analysis and design of storage tanks are generally based on the Housner's multi-component spring-mass analogy. This mechanical model will be described thoroughly in section 3.3.

### **American Concrete Institute Design Standards**

ACI Committee 350.3-06 provides additional comprehensive procedure, compared to ACI-318, for seismic analysis and design of liquid containing concrete structures. ACI 350 maintains ACI 318's seismic design provisions to the resistance side only. ACI 350.3-06 is based on ultimate strength design method, but the ultimate strength design of ACI is modified to account for the serviceability limit states by including durability factors in the design load combinations. Except for load combinations that include seismic loading, the environmental durability factor is applied to reduce the effective stress in non-per-stressed reinforcement to a level under service load conditions, such that stress levels are considered to be in an acceptable range for controlling the cracking.

This practice has been developed compared to traditional design provision such as ASCE 1984 and considers flexibility of the walls and its effect on amplification of the response. Also, ACI 350-06 considers the vertical acceleration effects and employs Square-Root-of-Sum-of-the-Squares method for combining the convective and impulsive responses.

## Dynamic Properties of Rectangular Tanks

The following procedure leads to defining the dynamic properties for the tank with uniform thickness. The procedure is limited to fixed-base open top tank that is filled with water to the depth of  $H_L$ . In the first step, the structural stiffness,  $k$ , for unit width of the tank wall can be computed according Eqn.2.4. This equation can be employed in the SI system. In Eqn.2.4,  $E_c$  is the modulus of elasticity of the concrete.  $t_w$  and  $h$  are thickness and height of the tank wall, respectively.

$$k = \frac{E_c}{4 \times 10^3} \left( \frac{t_w}{h} \right)^3 \quad (2.4)$$

Following, the circular frequency of impulsive mode of vibration is:

$$\omega_i = \sqrt{\frac{k}{m}} \quad (2.5)$$

where  $m$  is the total mass per unit width of rectangular wall and is the summation of the walls mass and the portion of the contained liquid that moves in unison with the tank:

$$m = m_w + m_i \quad (2.6)$$

Also, the circular frequency of oscillation of the first mode of sloshing equals to:

$$\omega_c = \frac{\lambda}{\sqrt{L}} \quad (2.7)$$

where  $\lambda = \sqrt{3.16g \tanh \left[ 3.16 \left( \frac{H_L}{L} \right) \right]}$ , and  $L$  is the length of the tank wall parallel to the direction of the ground motion.

American Concrete Committee 350 requires the liquid containing structure to be designed for the following loads:

- Force due to Hydrostatic pressure
- Inertia forces due to the wall and roof of the tank

- Both impulsive and convective hydrodynamic forces from the contained liquid
- Effect of vertical acceleration
- Dynamic earth pressures against the buried portion of the wall

This standard, adopted Housner model and separated the hydrodynamic pressure of the contained liquid into two components. First, the impulsive component that is proportional to the wall acceleration and associates with the inertia forces caused by wall acceleration. Second, the convective component that is produced by oscillation of the top part liquid. It should be noted that, for most tanks, it is the impulsive mode that dominates the loading on the tank wall. The first convective mode is usually less profound in comparison with the impulsive mode, and the higher order convective modes can as well be ignored.

As follows,  $W_i$  represents the resulting effect of impulsive pressure and  $W_c$  symbolizes that of convective pressure. In Housner's model,  $W_i$  is assumed to be rigidly attached to the tank wall at the height of  $h_i$  and  $W_c$  is attached to the walls at the height of  $h_c$  by springs. It should be noted that the force resulting from impulsive pressure first acts to stress the tank wall and the convective component of the resultant force, which depends on the tank dimension, tends to uplift the tank if there is not enough dead load. ACI 350.3-06 defines the two equivalent weight components of accelerating liquid adopting Housner's equation. These equations were also adopted by NZS 1986, ASCE 1981, and ANSI/AWWA 1995.

$$W_i = W_L \times \frac{\tanh \left[ 0.866 \left( \frac{L}{H_L} \right) \right]}{0.866 \left( \frac{L}{H_L} \right)} \quad (2.8)$$

$$W_c = W_L \times 0.264 \left( \frac{L}{H_L} \right) \tanh \left[ 3.16 \left( \frac{H_L}{L} \right) \right] \quad (2.9)$$

The centre of the gravity for the equivalent impulsive mass can be calculated as follows. First, if the base pressure is excluded the centre of gravity of accelerating liquid component can be defined as follows:

For tanks with  $\frac{L}{H_L} \leq 1.333$ :

$$h_i = H_L \times \left[ 0.5 - 0.09375 \left( \frac{L}{H_L} \right) \right] \quad (2.10)$$

For tanks with  $\frac{L}{H_L} \geq 1.333$ :

$$h_i = H_L \times 0.375 \quad (2.11)$$

Also, by including the base pressure (IBP) the height of the centre of gravity are as follows:

For tanks with  $\frac{L}{H_L} \leq 0.75$ :

$$h'_i = H_L \times 0.45 \quad (2.12)$$

For tanks with  $\frac{L}{H_L} \geq 0.75$ :

$$h'_i = H_L \times \frac{0.8666 \left( \frac{L}{H_L} \right)}{2 \tanh \left[ 0.8666 \left( \frac{L}{H_L} \right) \right]} \quad (2.13)$$

The centre of gravity of the convective component of the hydrodynamic pressure can be calculated according to Eqn. 2.14, when excluding base pressure (EBP) and according to Eqn. 2.15, by including base pressure (IBP):

$$h_c = H_L \times \left( 1 - \frac{\cosh \left[ 3.16 \left( \frac{H_L}{L} \right) \right] - 1}{3.16 \left( \frac{H_L}{L} \right) \sinh \left[ 3.16 \left( \frac{H_L}{L} \right) \right]} \right) \quad (2.14)$$

$$h'_c = H_L \times \left( 1 - \frac{\cosh \left[ 3.16 \left( \frac{H_L}{L} \right) \right] - 2.01}{3.16 \left( \frac{H_L}{L} \right) \sinh \left[ 3.16 \left( \frac{H_L}{L} \right) \right]} \right) \quad (2.15)$$

## Dynamic forces and Moments

Dynamic lateral forces above the base can be determined for the walls inertia, impulsive and convective components of the hydrodynamic pressure according to equations 2.16, 2.17 and 2.18, respectively:

$$P_W = C_i I \left[ \frac{\varepsilon W_W}{R_i} \right] \quad (2.16)$$

$$P_i = C_i I \left[ \frac{W_i}{R_i} \right] \quad (2.17)$$

$$P_c = C_c I \left[ \frac{W_c}{R_c} \right] \quad (2.18)$$

In Eqn. 2.16, Eqn. 2.17 and Eqn. 2.18,  $C_i$  and  $C_c$  are the seismic response coefficients;  $I$  is importance factor;  $R_i$ ,  $R_c$  are modification factor for rectangular tanks and can be defined as follows:

For  $T_i \leq T_s$

$$C_i = S_{DS} \quad (2.19)$$

And if  $T_i \geq T_s$

$$C_i = \frac{S_{D1}}{T_i} \leq S_{DS} \quad (2.20)$$

where

$$T_s = \frac{S_{D1}}{S_{DS}} \quad (2.21)$$

and for  $T_c \leq 1.6/T_s$

$$C_c = \frac{1.5S_{D1}}{T_c} \leq 1.5S_{DS} \quad (2.22)$$

otherwise,

$$C_c = \frac{2.4S_{DS}}{T_c^2} = \quad (2.23)$$

Note that,  $S_{D1}$  is the design spectral response acceleration, 5% damped, at a period of one second and  $S_{DS}$  is design spectral response acceleration, 5% damped, at short periods. Both are expressed as a fraction of the acceleration due to gravity  $g$ . These parameters can be calculated according to equations 2.24 and 2.25. Note that  $S_S$  and  $S_1$  are the mapped spectral response accelerations at short periods and 1 second, respectively, and can be obtained from the seismic ground motion maps of ASCE 7-05.  $F_a$  and  $F_{va}$  are the site coefficients and shall be obtained in conjunction with site classification table from ASCE 7-05.

$$S_{DS} = \frac{2}{3} S_S F_a \quad (2.24)$$

$$S_{D1} = \frac{2}{3} S_1 F_v \quad (2.25)$$

Importance factor,  $I$ , and response modification factors,  $R_i$  and  $R_c$  can be defined according to Table 2.2 and Table 2.1, respectively:

Table 2.1: Response modification factor  $R$

Type of Structure	$R_i$		$R_c$
	On or above ground	Buried*	
Anchored, flexible-base tanks	3.25†	3.25†	1.0
Fixed or hinged-base tanks	2.0	3.0	1.0
Unanchored, contained or uncontained tanks‡	1.5	2.0	1.0
Pedestal-mounted tanks	2.0	-	1.0

\*Buried tank is defined as a tank whose maximum water surface at rest is at or below ground level. For partially buried tanks, the  $R_i$  value may be linearly interpolated between that shown for on the ground and buried tank.

† $R_i = 3.25$  is the maximum  $R_i$  value permitted to be used for any liquid containing concrete structure.

‡Unanchored, uncontained tanks shall not be built in locations where  $S_s \geq 0.75$ .

Table 2.2: Importance factor  $I$

Tank Use	$I$
Tanks containing hazardous materials*	1.5
Tanks that are intended to remain usable for emergency purposes after an earthquake, or tanks that are part of lifeline systems	1.25
Tanks not listed in category 1 or 2	1.0

\*In some cases, for tanks containing hazardous material, engineering judgement may require a factor  $I \geq 1.5$

As was mentioned before, for well separated modes, lateral forces can be combined using the SRSS method. Following equations 2.16, 2.17 and 2.18, the total base shear resulted from seismic loading, for an open-top tank, shall be calculated as follows:

$$V = \sqrt{(P_i + P_w)^2 + P_c^2 + P_{eg}^2} \quad (2.26)$$

According to ACI 350.3-06 code, walls perpendicular to the direction of ground motion should be loaded perpendicular to their planes. Both the leading half and trailing half should be loaded for; wall's own inertia, one half of resulted impulsive force and one half of convective portion. Also, the buried portion of the tank on the trailing half should be loaded for dynamic earth and ground

water pressure. Note that buried tanks are not in the scope of this study. Dynamic equilibrium of the lateral forces for an on-the-ground tank is illustrated in Figure 2.1.

Walls parallel to the direction of the ground motion shall be loaded in their plane for the wall's own in-plane inertia force and the in-plane forces corresponding to the edge reactions from the abutting walls.

The wall-to-floor and wall-to-wall joints of the rectangular tanks shall be designed for the earthquake shear forces. For this purpose, walls perpendicular to the direction of the ground motion being investigated shall be analyzed as slabs subjected to the horizontal pressures calculated previously in this section. In addition, walls parallel to the direction of the ground motion being investigated shall be analyzed as shear walls subjected to the in-plane forces. The shear forces along the bottom and side joints shall correspond to the slab or the shear walls reactions.

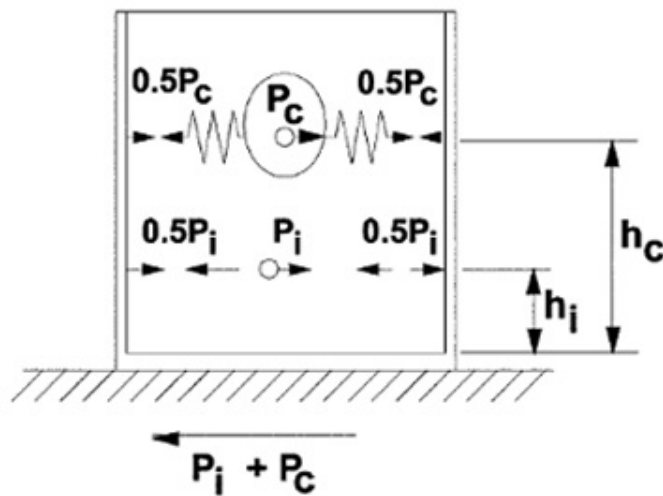


Figure 2.1: Dynamic equilibrium of lateral forces of the tank

Bending moment,  $M_b$ , on the entire tank cross-section, just above the base of the tank wall shall be determined according to equations 2.27, 2.28, 2.29 and 2.30:

$$M_W = P_W \times h_W \quad (2.27)$$

$$M_i = P_i \times h_i \quad (2.28)$$

$$M_c = P_c \times h_c \quad (2.29)$$

$$M_b = \sqrt{(M_i + M_w)^2 + M_c^2} \quad (2.30)$$

Overtopping moment,  $M_o$ , at the base of the tank, including the tank bottom and supporting structure (IBP) shall be determined according to equations 2.27, 2.31, 2.32 and 2.33:

$$M'_i = P_i \times h'_i \quad (2.31)$$

$$M'_c = P_c \times h'_c \quad (2.32)$$

$$M_o = \sqrt{(M'_i + M_w)^2 + M'_c{}^2} \quad (2.33)$$

### Pressure Distribution above the Base

Fluids exert pressure perpendicular to any contacting surface. When fluid is at rest, the pressure acts with equal magnitude in all directions. The liquid pressure  $P$  at a given depth depends only on the density of the liquid,  $\rho_l$ , and the distance below the surface of the liquid,  $h$ , and equals to:

$$P = \rho_l g h \quad (2.34)$$

Figure 2.2 shows the vertical distribution of hydrostatic pressure acting perpendicular to plane of the wall and consequently the total lateral force due to hydrostatic pressure equals to:

$$P_h = \frac{1}{2} \gamma_L H_L^2 \times B \quad (2.35)$$

In Eqn. 2.35,  $P_h$  is the pressure exerted on the wall, and  $B$  is the tank width.  $\gamma_L$  and  $H_L$  are the specific weight and height of the contained liquid, respectively.

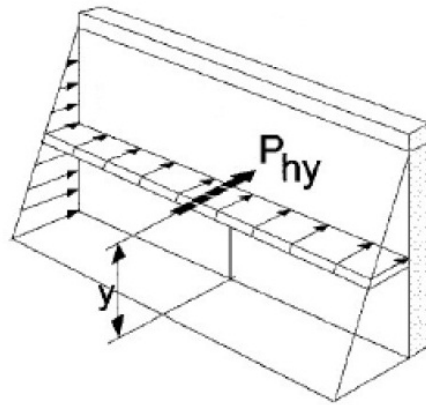


Figure 2.2: Hydrostatic pressure  $P_h$  distribution along the tank wall

$P_{iy}$  is the impulsive force and  $P_{cy}$  is the convective pressures at height  $y$  of the tank wall and can be calculated according to Eqn.2.36 and Eqn.2.37, respectively. Figure 2.3 represents the pressure distribution along the tank wall.

$$P_{iy} = \frac{\frac{P_i}{2} \left[ 4H_L - 6h_i - (6H_L - 12h_i) \left( \frac{y}{H_L} \right) \right]}{H_L^2} \quad (2.36)$$

$$P_{cy} = \frac{\frac{P_c}{2} \left[ 4H_L - 6h_c - (6H_L - 12h_i) \left( \frac{y}{H_L} \right) \right]}{H_L^2} \quad (2.37)$$

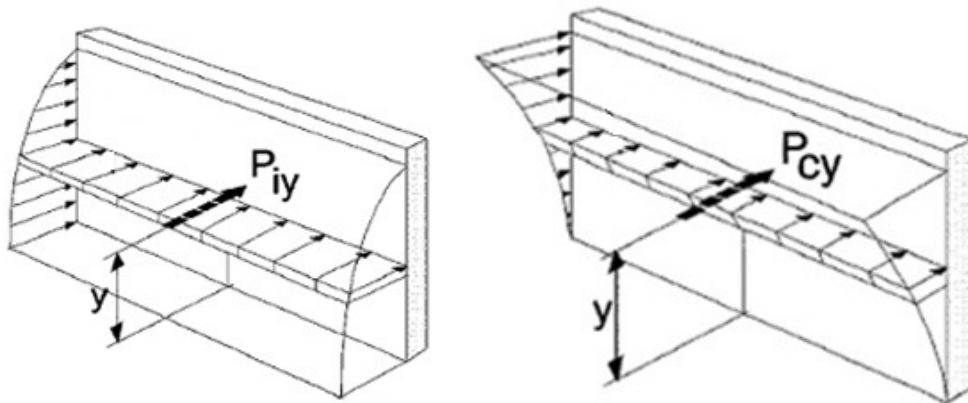


Figure 2.3: Hydrodynamic pressure distribution along the tank wall

## Wave Oscillation

In case of the storage for the toxic liquids or when overflow may result in damages to foundation materials, pipes, or roof, the structure should be designed either to have free-board allowance or an overflow spillway should be provided. Also, roof structure shall be designed to withstand the uplift pressures.

If the site specific response is employed, the maximum vertical displacement of contained liquid in the rectangular tanks can be estimated using the following equation:

$$d_{max} = \left(\frac{L}{2}\right) (C_c I) = \left(\frac{L}{2}\right) I(\eta_c) \frac{(0.667 S_D)}{g} \left(\frac{2\pi}{T_c}\right)^2 \quad (2.38)$$

In Eqn. 2.38,  $\eta_c$  accounts the influence of damping on the spectral amplification; so, if the site specific response spectrum is for damping ratio other than 5% of critical damping,  $\eta_c$  will be applied which equals to:

$$\eta_c = \frac{3.043}{2.73 - 0.45 \ln \beta} \quad (2.39)$$

# Chapter 3

## Mathematical Background

### 3.1 Introduction

The basic differential equations and boundary conditions for the lateral sloshing of the liquid-tank system are presented in this chapter. The velocity potential function for an inviscid, irrotational and incompressible fluid is described. Later, the velocity potential is derived for a rectangular tank subjected to free oscillation. The basic formulations of the fluid motion in an externally excited rectangular tank is, likewise, described in this chapter. Solution of these equations are also presented for a specific boundary condition such as rigid tank wall. As a result, the hydrodynamic pressure induced in partially filled rectangular tanks is estimated. It should be noted that most of these formulations are adopted from NASA SP-106 guideline for the Dynamic Behaviour of Liquids in Moving Containers (NASA special publications, 1966), and reviewed in such a way to be applicable for the rectangular tanks. The resulting force and moment in an excited tank is derived hereby. The equations described in section 3.2.1 can be employed as a simple procedure for calculations of the sloshing frequency as well as the maximum vertical displacement of the linear wave.

The equivalent mechanical models for the rectangular water tank in motion is reported in section 3.3. Analytical derivation of the mass-spring mechanical model and calculation of the corresponding masses, forces and moments are described. Also, the simplified single mass-spring model, proposed by Housner, is offered in section 3.3.

## 3.2 Numerical Simulation of the Liquid Motion in a Rectangular Tank

The problem of liquid sloshing interaction with the concrete container falls into two categories; first, the interaction between the free liquid surface motion and the breathing elastic modes of liquid container structure; and second, the interaction between liquid sloshing modes and the motion of the supporting elastic structure. Only the first category is within the scope of the present study, and in this study the tank is assumed to be fixed to the rigid foundation.

It is worth mentioning that the dynamic response of elastic liquid retaining structure interacting with the fluid is completely different of those when the tank is rigid. Hydrodynamic pressure induces forces on the tank walls and the developed force causes deformation of the structure, which in return modifies the hydrodynamic pressure. The interaction of the liquid sloshing dynamics with elastic deformations of the tank must be considered in studying the overall systems dynamics. These systems will be thoroughly discussed in this chapter.

For numerical simulation of the coupled system interacting with each other, which includes two or more non-linear system, it is more practical to represent the non-linear subsystem by a linear model. As the case of liquid and structure interaction, fluid domain can be represented by a linear model despite the non-linear behaviour of fluid sloshing. The linear model representing sloshing motion can be employed if the slosh motion is smaller compared to liquid depth and wave length. This method could be employed in case of dealing with small disturbances, and while the natural frequencies can be well separated.

### 3.2.1 Governing Equations

In this section, a set of equations based on physical laws will be discussed. Figure 3.1 shows a schematic diagram of the liquid-tank system under coordinate system. A rectangular water tank of  $2a$  and  $2b$  dimensions, partially filled with water to the depth of  $h$ . Owing to the three-dimensional geometry of the problem, a Cartesian coordinate system is employed to describe the position of any point belonging to the liquid domain. The container is assumed to be fixed to the rigid ground. The Cartesian co-ordinate system  $(x, y, z)$  has the origin located at the centre of the container, with  $oz$  opposing to the direction of gravity and  $z = h/2$  coinciding the free surface of water.

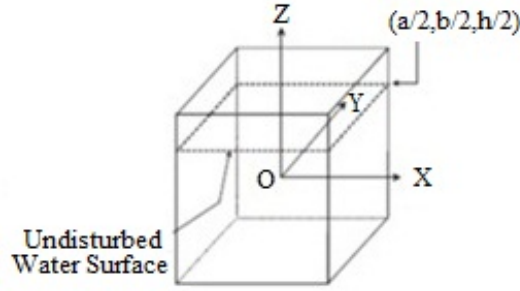


Figure 3.1: Coordinate system used for derivation of sloshing equations

If the tank is assumed to be attached to a rigid base and the contained fluid is inviscid and incompressible resulting in an irrotational flow field, the velocity potential  $\Phi$  contains  $x$ ,  $y$  and  $z$  components of  $u$ ,  $v$ ,  $w$  which are computed spatial derivation of the velocity potential:

$$u = \frac{\partial \Phi}{\partial x} \quad v = \frac{\partial \Phi}{\partial y} \quad w = \frac{\partial \Phi}{\partial z} \quad (3.1)$$

The velocity potential should satisfy the 3D Laplace equation at any point in the liquid domain respecting the assumption of the incompressible fluid:

$$\frac{\partial u}{\partial x} + \frac{\partial v}{\partial y} + \frac{\partial w}{\partial z} = 0 \quad \text{or} \quad \nabla^2 \Phi = 0 \quad (3.2)$$

The last from of Eqn. 3.2 is written in vector notation and applies to any coordinate system.

For the inviscid fluid, with either steady or unsteady flow, the equations of momentum conservation may be integrated to yield a single scalar equation referred to as Bernoulli equation:

$$\frac{\partial \Phi}{\partial t} + \frac{P}{\rho_l} + gz + \frac{1}{2} (u^2 + v^2 + w^2) = f(t) \quad (3.3)$$

In Eqn. 3.3,  $P$  is pressure,  $\rho_l$  is the fluid density, and  $g$  is the acceleration due to gravity corresponding to negative  $z$  direction.  $f(t)$  is the constant of the integration. As  $u$ ,  $v$ , and  $w$  components of velocity are assumed to be small, squared values of these quantities are also small compared to first order values and can be neglected. As a result, if the constant value of  $f(t)$  can be observed into  $\Phi$ , the Bernoulli equation will be linearized to the following form:

$$\frac{\partial \Phi}{\partial t} + \frac{P}{\rho_l} + gz = 0 \quad (3.4)$$

Assuming  $\eta(x, y, t)$  sloshing displacement to be very small and using the small wave theory, the linearized boundary condition at the free surface may also be written to Eqn. 3.5. As the natural frequencies of sloshing are involved in the time derivation of the potential flow, Eqn. 3.5 clearly shows the relationship between gravitational field and natural frequencies of sloshing.

$$\frac{1}{g} \frac{\partial^2 \Phi}{\partial t^2} + \frac{\partial \Phi}{\partial z} = 0 \quad z = h/2 \quad (3.5)$$

## Boundary Conditions

The linearized dynamic boundary conditions for the model illustrated in Figure 3.1 will be described here. For an open-top tank, the surface is free to move and  $p = \rho g \eta$  at  $z = h/2$ , so if  $\eta(x, y, z, t)$  represents the small displacement of the liquid, the unsteady Bernoulli equation can be written as:

$$\frac{\partial \Phi(x, y, z, t)}{\partial t} + g\eta(x, y, z, t) = 0 \quad \text{at} \quad z = h/2 \quad (3.6)$$

Clearly, the liquid at the free surface always remains at the free surface. Therefore, in addition to dynamic boundary condition, the kinematic boundary condition also should be satisfied. The kinematic boundary condition at the free surface relates the surface displacement to the vertical component of the velocity at the surface, and the equation is formed as:

$$\frac{\partial \eta}{\partial t} = \frac{\partial \Phi}{\partial z} = w \quad (3.7)$$

At the wet surface of the tank, the fluid velocity in the direction perpendicular to the tanks wall should be equal to the tanks velocity,  $v_n(t)$ , perpendicular to wall's own plane ( $n$  stands for the normal direction). Note that this assumption is only applicable for the cases when the tank motion is not rotational, and if the viscous stresses are negligible.

$$\frac{\partial \Phi}{\partial n} = v_n(t) \quad (3.8)$$

For the tanks with rigid walls,  $v_n(t)$  equals to ground velocity. However, for the case of flexible wall, the wall's velocity is the summation of the ground velocity and its relative velocity due to wall flexibility.

### 3.2.2 Solution of the Equations for a Rectangular Tank Subjected to Horizontal Motion

In this section, the solutions of the equation of motion for a rectangular tank is described. This method is adopted from NASA-SP-106. For simplicity, the motion of the tank is assumed to be harmonic and variant with time, as  $\exp(i\Omega t)$ , where  $\Omega$  is the frequency of the motion. In this case, the displacement can be expressed as  $X(t) = -iX_0 \exp(i\Omega t)$ .

The real displacement is equal to  $X_0 \sin \Omega t$ . The velocity components of the tank walls are  $v = w = 0$  and  $u = iX_0 \Omega \exp(i\Omega t)$ . Therefore, the boundary conditions at the wet surfaces of the tank walls are denoted as:

$$n \cdot \nabla \Phi = iX_0 \Omega e^{i\Omega t} \quad (3.9)$$

Eqn. 3.9 will be reduced to Eqn. 3.10 for the wet surface of the wall perpendicular to  $X$  axis. This equation states that, at the wall surface, the  $x$  component of the velocity is equal to the imposed horizontal velocity in  $x$  direction ( $n$  is the unit vector normal to the surface):

$$n \cdot \nabla \Phi = \frac{\partial \Phi}{\partial x} \quad (3.10)$$

As follows, solutions of Eqn. 3.10 will be used to determine the sloshing motions. Initially, the tank is considered to be stationary, and the solutions for this case are conventionally called the eigenfunctions of the problem.

The potential solutions of interest are assumed to be harmonic in time, for instance  $\exp(i\Omega t)$ . For much of this discussion, the time dependence of  $\Phi$  can be ignored, but when time derivatives are needed, they are included by multiplying the potential by  $i\Omega$ . The  $\Phi(x, y, z)$  eigenfunctions are

found by the method of separation of variables, in which  $\Phi(x, y, z)$  is assumed to be the product of three individual functions of  $\xi(x)$ ,  $\psi(y)$  and  $\zeta(z)$  of the coordinates. Therefore, Eqn.3.2 for  $\Phi = \xi \psi \zeta$  can be rewritten as:

$$\frac{1}{\xi} \frac{d^2 \xi}{dx^2} + \frac{1}{\psi} \frac{d^2 \psi}{dy^2} + \frac{1}{\zeta} \frac{d^2 \zeta}{dz^2} = 0 \quad (3.11)$$

In Eqn.3.11, each of the ratios shall be positive or negative constants. Thus, the solutions of different combination of negative and positive value should be satisfied at the boundary conditions for particular cases. Solutions of Eqn. 3.11 resulted in the determination of the natural frequency as well as the wave shape according to Eqn. 3.12 and Eqn. 3.13 respectively:

$$\omega_n^2 = \pi(2n-1) \left( \frac{g}{a} \right) \tanh \left[ \pi(2n-1) \left( \frac{h}{a} \right) \right] \quad (3.12)$$

$$\delta(x, t) = -\frac{2BF_i}{a\omega_n} (2n-1) \sinh \left[ \pi(2n-1) \left( \frac{h}{a} \right) \right] \sin \left[ \pi(2n-1) \left( \frac{x}{a} \right) \right] \quad (3.13)$$

where  $BF$  is constant value resulted from solution of the Eqn. 3.11.

On the other hand, if the tank is forced by an external motion, the boundary condition at the free surface and bottom of the tank are the same as one for the free oscillation. Therefore, once more, if the rectangular tank is forced by a horizontal motion in  $X$  direction, the boundary conditions in Eqn. 3.9 reduce to:

$$\frac{\partial \Phi}{\partial x} = \Omega X_0 e^{i\Omega t} \quad \text{for} \quad x = \pm a/2 \quad (3.14)$$

$$\frac{\partial \Phi}{\partial y} = 0 \quad \text{for} \quad y = \pm b/2 \quad (3.15)$$

$$\frac{\partial \Phi}{\partial z} = 0 \quad \text{for} \quad z = -h/2 \quad (3.16)$$

Then, satisfying Eqn. 3.14 and Eqn. 3.15, the trial solution is assumed to be:

$$\Phi = \left\{ A_0 x + \sum_{n=1}^{\infty} A_n \sin \left[ \lambda_n \frac{x}{a} \right] \left\{ \cosh \left[ \lambda_n \frac{z}{a} \right] + \tanh \left[ \lambda_n \frac{h}{2a} \right] \sinh \left[ \lambda_n \frac{z}{a} \right] \right\} \right\} e^{i\Omega t} \quad (3.17)$$

Where  $\lambda_n = (2n - 1)\pi$  and,  $BF$ , the constant value from the solution of the Eqn.3.11 is replaced by  $A_n$  ( $n$  indicates that the constant depends on the mode number). In Eqn.3.17, if  $A_0$  is equal to  $\Omega X_0$ , the potential  $\Phi$  will satisfy all the wall boundary conditions. Lastly,  $\Phi$  from Eqn.3.17 can be substitute in Eqn.3.6 to satisfy the boundary condition at the free surface, and changes to:

$$\begin{aligned} & -\Omega^2 \left\{ \Omega X_0 x + \sum_{n=1}^{\infty} A_n \sin \left( \lambda_n \frac{x}{a} \right) \left[ \cosh \left( \lambda_n \frac{h}{a} \right) + \tanh \left( \lambda_n \frac{h}{2a} \right) \sinh \left( \lambda_n \frac{h}{a} \right) \right] \right\} + \\ & g \left\{ \sum_{n=1}^{\infty} A_n \left( \frac{\lambda_n}{a} \right) \sin \left( \lambda_n \frac{x}{a} \right) \left[ \sin \left( \lambda_n \frac{x}{a} \right) + \tanh \left( \lambda_n \frac{h}{2a} \right) \cosh \left( \lambda_n \frac{h}{a} \right) \right] \right\} = 0 \end{aligned} \quad (3.18)$$

This equation, in effect, specifies the integration constants  $A_n$  in terms of  $X_0$ . But to determine them explicitly, the  $x$  in the first term of Eqn. 3.18 has to be written as a Fourier series of  $\sin(\lambda_n/a)$  terms (which is possible because the  $\sin(\lambda_n/a)$  terms are orthogonal over the interval  $-a/2 \leq x \leq a/2$ ). This process gives:

$$x = \sum_{n=1}^{\infty} \left( \frac{2a^2}{\lambda_n^2} \right) (-1)^{n-1} \sin(\lambda_n x/a) \quad (3.19)$$

By substituting Eqn.3.19 and Eqn.3.12, the final expression for the velocity potential is:

$$\Phi(x, z, t) = A_0 e^{i\Omega t} \cdot \left\{ x - \sum_{n=1}^{\infty} \frac{4a(-1)^{n-1}}{\lambda_n^2} \left( \frac{\Omega^2}{\omega_n^2 - \Omega^2} \right) \sin \left[ \lambda_n \frac{x}{a} \right] \cdot \frac{\cosh[\lambda_n(z/a + h/2a)]}{\cosh[\lambda_n(h/a)]} \right\} \quad (3.20)$$

Generally, the hydrodynamic pressure in a partially filled moving container has two separate components. One is directly proportional to the acceleration of the tank and is caused by part of the fluid moving in unison with the tank, which is known as impulsive pressure. The second is known as convective pressure and experiences sloshing at the free surface. By relating the impulsive component to the interaction between the wall and the liquid and neglecting the free surface sloshing, Eqn.3.20 should satisfy a new boundary condition as  $\frac{\partial \Phi}{\partial z} = 0$  at  $z = +h/2$ . Thus,

the impulsive potential function  $\Phi_i$  can be acquired using Eqn.3.21:

$$\Phi_i(x, z, t) = A_0 e^{i\Omega t} \left\{ x - \sum_{n=1}^{\infty} \frac{4a(-1)^{n-1}}{\lambda_n^2} \sin \left[ \lambda_n \frac{x}{a} \right] \cdot \frac{\cosh [\lambda_n (z/a + h/2a)]}{\cosh [\lambda_n (h/a)]} \right\} \quad (3.21)$$

Convective potential function can also be obtained by assuming,  $\Phi = \Phi_i + \Phi_c$ , and according to Eqn.3.22:

$$\Phi_c(x, z, t) = A_0 e^{i\Omega t} \left\{ \sum_{n=1}^{\infty} \frac{4a(-1)^{n-1}}{\lambda_n^2} \left( \frac{\Omega^2}{\omega_n^2 - \Omega^2} \right) \sin \left[ \lambda_n \frac{x}{a} \right] \cdot \frac{\cosh [\lambda_n (z/a + h/2a)]}{\cosh [\lambda_n (h/a)]} \right\} \quad (3.22)$$

The forces and moments acting on the tank can be determined by integrating the unsteady part of the liquid pressure,  $P$ , over the tank wall area. For a horizontally excited rectangular tank, the exerted force is:

$$F_x = 2 \times \int_{-h/2-b/2}^{+h/2+b/2} \int P|_{x=a/2} dydz = -2\rho b \int_{-h/2}^{+h/2} \frac{\partial \Phi}{\partial t} |_{x=a/2} dz \quad (3.23)$$

With substituting the potential function from Eqn.3.20, the linearized form of Eqn.3.23 with respect to the unsteady pressure can be rewritten as:

$$\frac{F_{x0}}{-i\Omega^2 X_0 m_{liq}} = 1 + 8 \frac{a}{h} \sum_{n=1}^N \frac{\tanh [(2n-1) \pi h/a]}{(2n-1)^3 \pi^3} \frac{\Omega^2}{\omega^2 - \Omega^2} \quad (3.24)$$

In Eqn.3.24,  $m_{liq}$  is the mass of the liquid and  $F_{x0}$  is the amplitude of the oscillating force.

It should be noted that Eqn.3.24 is derived with the assumption of viscous effect and damping to be ignored. Therefore, according to Eqn.3.24, in cases that the frequency of the motion is close to the frequency of the sloshing, extreme forces will be exerted. Besides, when the frequency of the motion is very small, the summation in Eqn.3.24 reaches the value of zero. In that case, the force is the only product of the liquid mass and the tank acceleration, as if the liquid is frozen.

In addition, for the  $\Omega \gg \omega_n$ , the summation is independent of the  $\omega$  and again moves as a rigid

body with a mass that is less than the total mass of the contained liquid. This indicates that some portion of the liquid (near the free surface) moves separately from the tank. Accordingly, by neglecting the free surface sloshing, the exerted force can be calculated according Eqn. 3.25:

$$\frac{F_{x0}}{-i\Omega^2 X_0 m_{liq}} = 1 - 8 \frac{a}{h} \sum_{n=1}^N \frac{\tanh[(2n-1)\pi h/a]}{(2n-1)^3 \pi^3} \quad (3.25)$$

Exerted moment acting about  $Y$  axis on the tank is computed as follows:

$$M_y = -2b\rho \times \int_{-h/2}^{+h/2} z \frac{\partial \Phi}{\partial t} \Big|_{x=a/2} dz - 2b\rho \times \int_{-a/2}^{a/2} x \frac{\partial \Phi}{\partial t} \Big|_{z=-h/2} dx \quad (3.26)$$

After performing the indicated integrations, simplifying the result with various algebraic and hyperbolic transformations, and rearranging the results to make for easy comparisons with the force, it is found that the moment is:

$$\frac{M_{y0}}{-i\Omega^2 X_0 m_{liq} h} = \frac{1}{12} (a/h)^2 + 8(a/h) \sum_{n=1}^{\infty} \frac{\tanh[(2n-1)(\pi h/a)]}{(2n-1)^3 \pi^3} \cdot \left\{ \frac{1}{2} - \frac{2(a/h) \tanh[(2n-1)(\pi h/2a)]}{(2n-1)\pi} + \frac{g}{h\omega_n^2} \right\} \frac{\Omega^2}{\omega^2 - \Omega^2} \quad (3.27)$$

Similarly, by neglecting the free surface sloshing for the cases that  $\Omega \gg \omega_n$ , the moment acting about  $Y$  axis is computed as follows:

$$\frac{M_{y0}}{-i\Omega^2 X_0 m_{liq} h} = \frac{1}{2} + 8(a/h) \sum_{n=1}^{\infty} \frac{\tanh[(2n-1)(\pi h/a)]}{(2n-1)^3 \pi^3} \quad (3.28)$$

When a rectangular tank is subjected to an external horizontal motion, the excitation causes the contained liquid to experience vertical displacement, which is referred to as sloshing height. If the equation of motion (Eqn. 3.20) satisfies the free surface boundary condition, the wave amplitude can be calculated as follows:

$$\delta = -\frac{i\Omega^2 X_0 e^{i\Omega t}}{g} \left\{ \sum_{n=1}^{\infty} \frac{4a(-1)^{n-1}}{(2n-1)^2 \pi^2} \left( \frac{\omega_n^2}{\omega_n^2 - \Omega^2} \right) \sin \left[ (2n-1) \pi \frac{x}{a} \right] \right\} \quad (3.29)$$

### 3.3 Equivalent Mechanical Models

A realistic representation of the liquid dynamics inside its closed containers can be approximated by an equivalent mechanical system. The technique of equivalent mechanical models is a very useful mathematical tool for solving the complete dynamic problem of complicated systems. The principals for constructing a mechanical model are based on the following conditions:

- The equivalent masses and moments of inertia must be preserved and the centre of gravity must remain the same for small oscillations.
- The system must possess the same modes of oscillations and produce the same damping forces.
- The force and moment components under certain excitation of the model must be equivalent to the ones produced by the actual system.

Historically, mechanical models were first developed for tanks with rigid walls. Housner (1963) was the first to propose such a mechanical model for circular and rectangular rigid tanks. Wozniak and Mitchell (1978) have generalized the Housner's model for short and slender tanks. Veletsos and Yang (1977) have used a different approach to arrive at a similar type of mechanical model for circular rigid tanks. Subsequently, Haroun and Housner (1981) and Veletsos (1984) have developed mechanical models for flexible tanks. Malhotra et al. (2000) have further simplified the flexible tank model of Veletsos (1984).

For the case of rectangular tank under ground motion, when the flexible wall is interacting with the contained liquid, it is more practical to substitute the non-linear behaviour of the sloshing surface with a linearized equivalent mechanical system representing the sloshing motion. As mentioned previously, for constructing a mechanical model the equivalent masses should be the same as the liquid mass. Preserving the first principle, the liquid in the tank can be replaced by a set of mass-spring-dashpot systems or by a set of pendulums. Figures 3.2 and 3.3 show two different mechanical systems that can be used to represent the motion of liquid in the seismically excited tank.

If the fluid free surface remains planar without rotation of its nodal diameter, the system can be described by a linear equation for the first antisymmetric mode, that is equivalent to a pendulum describing small oscillations. As illustrated in Figure 3.2, each pendulum represents one sloshing mode, also a rigidly attached mass is chosen to represent the effect of the liquid that moves in

unison with the tank as impulsive component. As previously was described, the first antisymmetric wave represents the first fundamental convective mode and possesses the lowest natural frequency. Waves with two or more peaks with higher natural frequencies can also occur. The mechanical model shown in Figure 3.2 can constitute these higher order waves by incorporating additional pendulums for each mode. It should be noticed that the magnitudes of the pendulum for higher order modes are very small compared with the fundamental mode; thus, higher order modes are usually of little concern. As follows, derivation of the parameters corresponding to each of these mechanical models will be described.

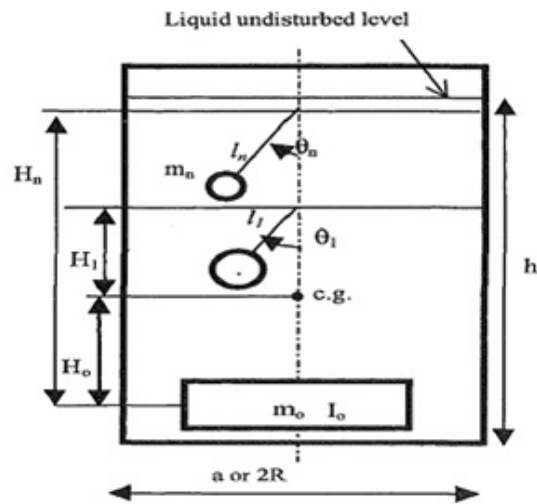


Figure 3.2: Pendulum-mass mechanical model representing different modes

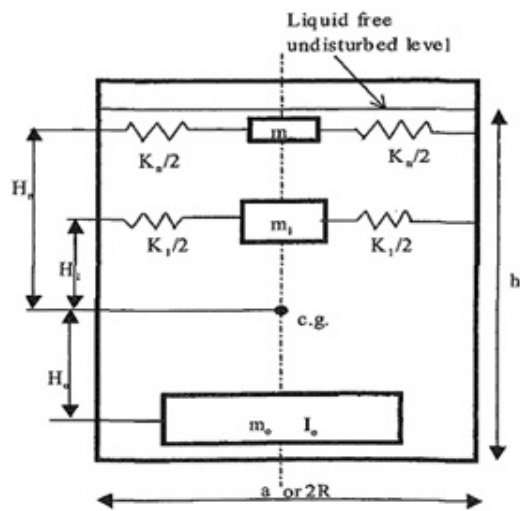


Figure 3.3: Mass-spring mechanical model

### 3.3.1 Parameters for the Mass Spring Model

To preserve the static properties of the liquid contained rectangular tanks, the summation of rigidly attached component of the liquid and different sloshing modes of liquid should be the same as liquid mass:

$$m_o + \sum m_n = m_{liq} \quad (3.30)$$

In both mechanical models present in Fig. 3.2 and Fig. 3.3,  $m_o$  represents the mass of the liquid for the impulsive component of the pressure and  $m_n$  symbolizes the mass of the liquid corresponding to  $n$ th modes of sloshing. Again, to satisfy the static properties, the centre of gravity of the model must be the same elevation as the liquid:

$$m_o H_o + \sum m_n H_n = 0 \quad (3.31)$$

It should be noted that  $H_o$  and  $H_n$  represent the centre of gravity of the impulsive mass and the one for the  $n$ th modes of sloshing, respectively. In addition to static properties of the tank, the mechanical model should duplicate identical modes of oscillation, equivalent sloshing forces, moments, and natural frequencies. In order to preserve the natural frequencies of sloshing modes, the stiffness characteristic of the spring, which is attached to  $n$ th modes of sloshing, should satisfy the following equation:

$$\sqrt{\frac{k_n}{m_n}} = \omega_n \quad (3.32)$$

Where  $\omega_n$  represents the natural frequency of the  $n$ th mode of sloshing.

Respecting the third principles of the mechanical model, the forces exerted in the  $+X$  direction by the mechanical model should be the same as the lateral forces exerted on the tank walls by sloshing of the liquid for a horizontal excitation. The net force in the  $+X$  direction produced by the mechanical model is given by the reverse inertia forces:

$$-F = m_o \ddot{X}_o + \sum m_n (\ddot{X}_o + \ddot{x}_n) \quad (3.33)$$

and the moment exerted on the tank can be computed according to Eqn. 3.34 (the second part of

equation represents the moment caused by vertical offset of masses):

$$-M = \sum m_n h_n \ddot{x}_n - g \sum m_n \ddot{x}_n \quad (3.34)$$

Accordingly, the equation of the motion for each spring-mass is expressed as:

$$m_n(\ddot{X}_o + \ddot{x}_n) + K_n x_n = 0 \quad (3.35)$$

So, if the tank was excited by the frequency of  $\Omega$ , and ground displacement of  $X(t) = -iX_o \exp(i\Omega t)$ , Eqn. 3.35 shall be rewritten as:

$$x_n = -\frac{i\Omega^2 X_o}{\omega_n^2 - \Omega^2} \quad (3.36)$$

With these equations, the amplitudes of the force and moment on the tank can be expressed analytically as:

$$\frac{F_{amp}}{i\Omega^2 m_{liq}} = -\left[1 + \sum \frac{m_n}{m_{liq}} \left(\frac{\Omega^2}{\omega^2 - \Omega^2}\right)\right] X_o \quad (3.37)$$

$$\frac{M_{amp}}{i\Omega^2 X_o m_{liq}} = \sum \frac{m_n}{m_{liq}} \left(\frac{H_n \Omega^2 + g}{\omega^2 - \Omega^2}\right) \quad (3.38)$$

Thus, if  $m_{cn}$  and  $k_{cn}$ , respectively, represent the equivalent mass and spring stiffness of the  $n$ th mode, they can be calculated by comparing with the lateral forces exerted on the tank by sloshing liquid, and according to Eqn. 3.39 and Eqn. 3.40:

$$m_n = \frac{8m_{liq}a/h}{\pi^3(2n-1)^3} \tanh\left[(2n-1)\frac{\pi h}{a}\right] \quad (3.39)$$

$$k_n = \frac{8m_{liq}g}{h\pi^2(2n-1)^2} \left(\tanh\frac{\pi(2n-1)h}{a}\right)^2 \quad (3.40)$$

Likewise, if the moment created by  $x$ -translation of the tank is duplicated by the mechanical

system, the axial elevation of the masses also is defined by:

$$H_n = \frac{h}{2} - 2a \frac{\tanh \left[ (2n-1) \frac{\pi h}{2a} \right]}{(2n-1)\pi} \quad (3.41)$$

The simplified single-spring-mass model was extended by Housner (1957) for application in the liquid tank system, and is shown in Figure 3.4. In this mechanical model, the force exerted by the sloshing water would correspond to  $M_c$ , and  $M_i$  stands for the mass that is rigidly attached to the tank wall and bottom experiencing the same acceleration as the tank.

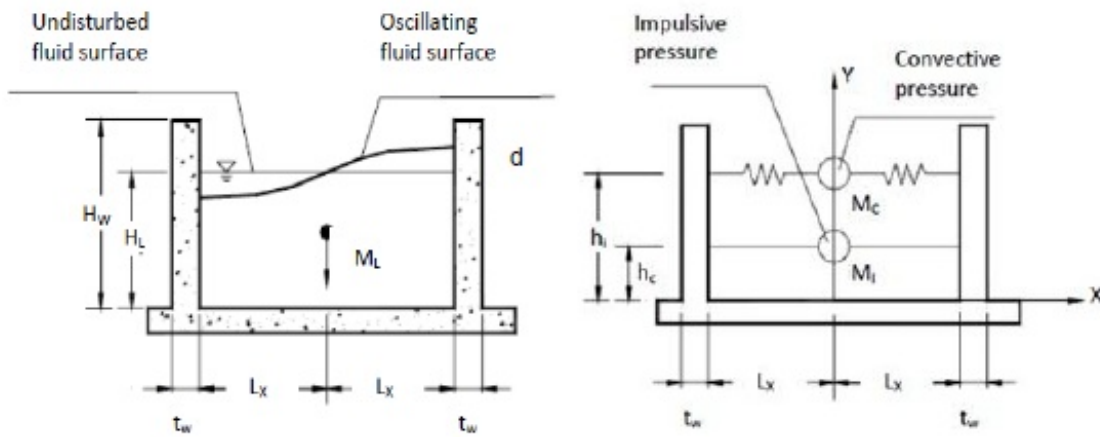


Figure 3.4: Single convective mass model proposed by Housner

Generally, a single convective mass is used, as higher modes of sloshing have negligible influence on the force exerted in the container, even if the fundamental frequency of the structure is close to the natural frequency of sloshing. According to Housner's method, the equivalent mass for the impulsive component and the corresponding height as well as the ones for convective component can be calculated using Eqn. 3.42 and Eqn. 3.43 respectively:

$$M_i = M \frac{\tanh 0.85 L/h}{1.7L/h} \quad (3.42)$$

$$h_i = \frac{3}{8}h \left\{ 1 + \alpha \left[ \frac{M}{M_c} \left( \frac{L}{h} \right)^2 - 1 \right] \right\}$$

$$M_c = M \frac{(0.83) \tanh 1.6 h/L}{1.6h/L} \quad (3.43)$$

$$h_c = h \left[ 1 - \frac{1}{3} \frac{M}{M_c} \left( \frac{L}{h} \right)^2 - 0.63\beta \frac{L}{h} \sqrt{0.28 \left( \frac{M L}{M_c h} \right)^2 - 1} \right]$$

where  $\alpha = 1.33$  and  $\beta = 2.0$ .

In Housner's model, if the tanks is assumed to behave rigidly under ground motion, the maximum value of horizontal movement of the convective mass relative to the tank wall, corresponds to the maximum vertical oscillation of the free surface. In addition, corresponds to the maximum horizontal convective force exerted on the tank wall. In Figure 3.4,  $d$ , shows the vertical displacement of the water. If the tank is excited by the initial displacement of the convective mass as  $x = A_c \sin \Omega t$ , the maximum sloshing height for the rectangular tank is:

$$d = \frac{0.527 L \coth(1.58 \frac{h}{L})}{\frac{g}{\Omega^2 \theta_h L} - 1} \quad (3.44)$$

Where  $\theta_h$  represents the angular amplitude of free oscillation at the fluid surface, based on the assumption of a plane water surface and equals to:

$$\theta_h = 1.58 \frac{A_c}{L} \tanh \left( 1.58 \frac{h}{L} \right) \quad (3.45)$$

The maximum vertical displacement of the free surface can be re-written as follows:

$$d = \frac{0.84 A_c \left( \frac{k_c g}{M_c g} \right)}{1 - \frac{A_c}{L} \left( \frac{k_c L}{M_c g} \right)} \quad (3.46)$$

and

$$k_c = 3 \frac{M_c^2 g h}{M L^2} \quad (3.47)$$

### 3.3.2 Parameters for the Pendulum Model

In the pendulum model shown in Figure 3.2, each pendulum represents one sloshing mode. A rigidly attached mass is also chosen to duplicate the effect of the liquid that moves unison with the

structure. Matching the hydrodynamic forces due to horizontal excitation, to the total forces due to the mechanical model consisting of pendulums and rigid mass, the following characteristics will be defined for the system:

The equivalent masses for each sloshing mode ( $m_n$  represents the  $n$ th modes pendulum mass and  $l_n$  represents  $n$ th modes pendulum length):

$$m_n = \frac{8\rho_l B L^2}{(2n-1)^3 \pi^3} \tanh(2n-1) \frac{\pi H_L}{L} \quad (3.48)$$

$$l_n = \frac{L}{(2n-1)\pi} \coth(2n-1) \frac{\pi H_L}{L} \quad (3.49)$$

$$H_n = l_n + H_L/2 - \frac{2L}{(2n-1)\pi} \tanh(2n-1) \frac{\pi H_L}{L} \quad (3.50)$$

Accordingly, the rigid mass is:

$$m_o = m_{liq} - \sum m_n \quad (3.51)$$

# Chapter 4

## Finite Element Methodology

### 4.1 Introduction

Finite Element Method (FEM) is among the methods that can be used for the analysis and design of civil and mechanical engineering structures. Application of finite element method in simulations of dynamic events has become very practical. Due to cost effectiveness and practical procedure, this method is used to have the highest possible confidence in the computed results. This chapter presents the theories of finite element method used for dynamic analysis of concrete rectangular LCS. The results of analysis based on the full finite element models will be discussed later in chapter 5.

The appropriate mathematical model was chosen for the fluid-structure interaction in the rectangular tank and was discussed in chapter 3. Now, in chapter 4, the finite element solution of the model will be discussed. Derivation of FEM formulation for the system is discussed hereby. In this chapter, the solutions of the differential equation for the coupled fluid-structure system will be described. Derivation of Finite Element formulation for the structure domain is discussed in section 4.2.1. Formation of the coupling matrix for the coupled system of Tank-Fluid is also prescribed in section 4.2.2. Modelling of the fluid domain is described in section 4.2.3. Finally, the solution of the coupled system in time-domain is discussed in section 4.2.4.

## 4.2 Finite Element Modelling of the Coupled Systems

For a coupled system, such as the one of concern in this study, there are unknown forces at the interface; therefore, neither of the domains can be solved independently of the other. In a partially filled water tank, coupling occurs on domain interfaces via the boundary conditions. In these cases, physically different problems interact; but, it is possible to consider coupling between the domains that are physically similar. In this chapter, derivation of the coupling matrix, which relates the pressure of the liquid element at the interface to the equivalent structural force and reverse, will be discussed. Also, derivation of the equation of motion by finite element method, for the tank structure as well as the one for the contained fluid is described hereby.

In this study, direct integration method will be employed. Note that, for the case of multi or single DOF system that the acceleration of the ground motion varies arbitrarily with time, analytical solution is nearly impossible. Therefore, the dynamic response of the rectangular tank will be solved by numerical time-stepping method for integration of differential equations. Note that the time stepping is not an exact procedure. However, if this method meets requirement such as convergence, stability and accuracy, can be used with confidence. Among different time-stepping methods, Newmark method will be employed in this study.

### 4.2.1 Finite Element Modelling of the Tank Structure

For the tank structure, formulation of the equation of motion by finite element method can be summarized in the following steps:

- Idealize the system as an assemblage of a finite number of elements that are only connected at nodes
- Define the degree of freedom at each node, and DOF of the whole system
- For each finite element, form the stiffness matrix,  $K$ , and form the stiffness matrix for the whole system
- Create the mass matrix,  $M$ , for each individual element; then, assemble the mass matrix for the system
- Form the damping matrix,  $C$

- Form the force-displacement and inertia force-acceleration relation for each element
- Then assemble the transformation matrix that relates the force and displacement for each element to the force and displacement of the assemblage
- Assemble the element matrices to determine the stiffness and mass matrices and applied force vector for the system
- Finally, formulate the equation of motion for the finite element assemblage

Figure 4.1 represents a system that contains a finite number of element having one DOF at each node. In this system,  $M_n$  represents the mass of each element.

The mass matrix for the structure is:

$$[M] = \begin{bmatrix} M_1 & \cdot & \cdot & \cdot & \cdot & \cdot \\ \cdot & M_2 & \cdot & \cdot & \cdot & \cdot \\ \cdot & \cdot & M_3 & \cdot & \cdot & \cdot \\ \cdot & \cdot & \cdot & \cdot & \cdot & \cdot \\ \cdot & \cdot & \cdot & \cdot & M_{n-1} & \cdot \\ \cdot & \cdot & \cdot & \cdot & \cdot & M_n \end{bmatrix} \quad (4.1)$$

The mass matrix  $[M]$  is a diagonal matrix and in general it can be a non-diagonal symmetric matrix.

Similarly, the stiffness matrix is also assembled as:

$$[K] = \begin{bmatrix} K_{11} & K_{12} & K_{13} & \cdot & \cdot & K_{1n} \\ K_{21} & K_{22} & \cdot & \cdot & \cdot & \cdot \\ K_{31} & \cdot & K_{33} & \cdot & \cdot & \cdot \\ \cdot & \cdot & \cdot & \cdot & \cdot & \cdot \\ \cdot & \cdot & \cdot & \cdot & K_{n-1} & \cdot \\ K_{n1} & \cdot & \cdot & \cdot & \cdot & K_n \end{bmatrix} \quad (4.2)$$

Damping matrix for the tank structure is:

$$[C] = \begin{bmatrix} C_{11} & C_{12} & C_{13} & \cdot & \cdot & C_{1n} \\ C_{21} & C_{22} & \cdot & \cdot & \cdot & \cdot \\ C_{31} & \cdot & C_{33} & \cdot & \cdot & \cdot \\ \cdot & \cdot & \cdot & \cdot & \cdot & \cdot \\ \cdot & \cdot & \cdot & \cdot & C_{n-1} & \cdot \\ C_{n1} & \cdot & \cdot & \cdot & \cdot & C_n \end{bmatrix} \quad (4.3)$$

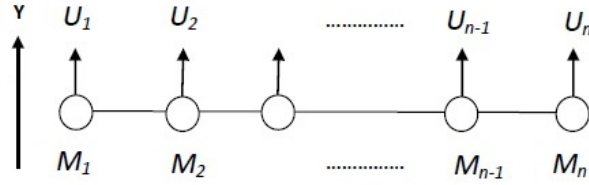


Figure 4.1: An example of a system discretized to a finite number of elements

Therefore, the inertia forces are,  $F_I = [M] [\ddot{u}]$ :

$$F_I = \begin{bmatrix} F_{I1} \\ F_{I2} \\ \cdot \\ \cdot \\ F_{I(n-1)} \\ F_{I(n)} \end{bmatrix} = \begin{bmatrix} M_1 & \cdot & \cdot & \cdot & \cdot & \cdot \\ \cdot & M_2 & \cdot & \cdot & \cdot & \cdot \\ \cdot & \cdot & \cdot & \cdot & \cdot & \cdot \\ \cdot & \cdot & \cdot & \cdot & \cdot & \cdot \\ \cdot & \cdot & \cdot & \cdot & M_{n-1} & \cdot \\ \cdot & \cdot & \cdot & \cdot & \cdot & M_n \end{bmatrix} \times \begin{bmatrix} \ddot{u}_1 \\ \ddot{u}_2 \\ \cdot \\ \cdot \\ \ddot{u}_{n-1} \\ \ddot{u}_n \end{bmatrix} \quad (4.4)$$

Damping forces can be written as,  $F_D = [C] [\dot{u}]$ :

$$F_D = \begin{bmatrix} F_{D1} \\ F_{D2} \\ \cdot \\ \cdot \\ F_{D(n-1)} \\ F_{D(n)} \end{bmatrix} = \begin{bmatrix} C_{11} & C_{12} & C_{13} & \cdot & \cdot & C_{1n} \\ C_{21} & C_{22} & \cdot & \cdot & \cdot & \cdot \\ C_{31} & \cdot & C_{33} & \cdot & \cdot & \cdot \\ \cdot & \cdot & \cdot & \cdot & \cdot & \cdot \\ \cdot & \cdot & \cdot & \cdot & C_{n-1} & \cdot \\ C_{n1} & \cdot & \cdot & \cdot & \cdot & C_n \end{bmatrix} \times \begin{bmatrix} \dot{u}_1 \\ \dot{u}_2 \\ \cdot \\ \cdot \\ \dot{u}_{(n-1)} \\ \dot{u}_n \end{bmatrix} \quad (4.5)$$

Similarly, the forces due to elasticity are,  $F_s = [K] [u]$ :

$$F_C = \begin{bmatrix} F_{S1} \\ F_{S2} \\ \cdot \\ \cdot \\ F_{S(n-1)} \\ F_{S(n)} \end{bmatrix} = \begin{bmatrix} K_{11} & K_{12} & K_{13} & \cdot & \cdot & K_{1n} \\ K_{21} & K_{22} & \cdot & \cdot & \cdot & \cdot \\ K_{31} & \cdot & K_{33} & \cdot & \cdot & \cdot \\ \cdot & \cdot & \cdot & \cdot & \cdot & \cdot \\ \cdot & \cdot & \cdot & \cdot & K_{n-1} & \cdot \\ K_{n1} & \cdot & \cdot & \cdot & \cdot & K_n \end{bmatrix} \times \begin{bmatrix} u_1 \\ u_2 \\ \cdot \\ \cdot \\ u_{(n-1)} \\ u_n \end{bmatrix} \quad (4.6)$$

In order to have the system satisfying the dynamic equilibrium, the external forces applied on the system shall be equal to the internal forces. As a result, the equation of motion for the tank structure shall be written according to Eqn.4.7:

$$[f_t] = [M][\ddot{u}] + [C][\dot{u}] + [K][u] \quad (4.7)$$

and if the system is subjected to base acceleration, the equation of motion is:

$$[f_t] - [M][\ddot{u}_g] = [M][\ddot{u}] + [C][\dot{u}] + [K][u] \quad (4.8)$$

In the coupled system such as water tank, the external load acting on the system may be separated to two components. First,  $f$ , as the force due to hydrodynamic pressure, and  $f_1$ , as the resultant of any other forces acting on the system. Therefore, Eqn.4.8 shall be re-written as:

$$[f] + [f_1] - [M][\ddot{u}_g] = [M][\ddot{u}] + [C][\dot{u}] + [K][u] \quad (4.9)$$

If in Eqn.4.9,  $[F_1] = [f_1] - [M][\ddot{u}_g]$ , equation of motion for the tank structure derived by finite element method can be expressed as:

$$[M][\ddot{u}] + [C][\dot{u}] + [K][u] = [F_1] + [f] \quad (4.10)$$

## 4.2.2 Coupling Matrix of Liquid-Tank System

As mentioned previously, at the interface of the coupled domains, there are some unknown forces induced by the interacting boundary elements. Likewise, in the coupled liquid-tank system, the hydrodynamic pressure of the liquid in motion exerts equivalent of structural force at the wet

surface of the wall. The coupling matrix  $[Q]$  that relates the pressure to the force is:

$$[Q] \times [P] = [f] \quad (4.11)$$

In Eqn.4.11,  $P$  is the pressure and  $f$  is its equivalent structural force. The coupling matrix can be found by the virtual work theory. Accordingly, the work done by the pressure at the interface element of the fluid domain and the structure shall be equal to the work done by equivalent nodal forces on the interface boundary element. The virtual work theory, for a line element on the interaction boundary in 2D model, as demonstrated in Figure 4.2, shall be expressed as:

$$\int P^e U_n ds = [f_e]^T [\delta] = \begin{bmatrix} f_{x1} & f_{y1} & f_{x2} & f_{y2} \end{bmatrix} \begin{bmatrix} u_1 \\ v_1 \\ u_2 \\ v_2 \end{bmatrix} \quad (4.12)$$

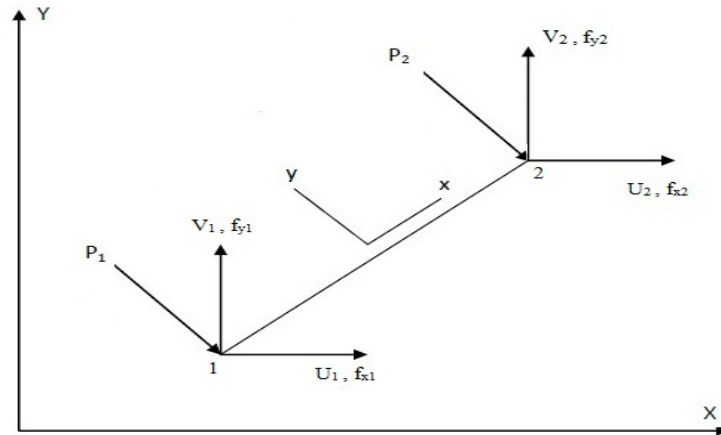


Figure 4.2: A two-dimensional element at the fluid domain and structure domain interaction boundary

In Eqn.4.12,  $P^e$  and  $U_n$  are the pressure and the normal displacement along the element interface, respectively. Node that,  $e$  refers to the element at the interaction boundary.  $[f_e]$  is the force vector of the element and  $[\delta]$  is the displacement of the element. Moreover,  $f_{x1}$  and  $f_{y1}$  represent the nodal forces at node 1 in  $X$  and  $Y$  directions, respectively. Similarly, for node 2, the nodal forces are shown by  $f_{x2}$  and  $f_{y2}$ . For the interface element,  $u$  and  $v$  symbolize the  $X$  and  $Y$  components of the nodal displacement. Therefore, by introducing shape function  $N_i$  at each node, the following equation shall be written to relate nodal displacement to element displacement:

$$u = N_1 u_1 + N_2 u_2 \quad (4.13)$$

$$v = N_1 v_1 + N_2 v_2 \quad (4.14)$$

According to Eqn.4.13 and Eqn.4.14, the normal displacement along the interface element surface is:

$$U_n = u_n + v_n = \eta N_1 u_1 + \eta N_2 u_2 + \beta N_1 v_1 + \beta N_2 v_2 \quad (4.15)$$

Where in Eqn.4.15,  $\eta$  and  $\beta$  are the absolute values of the normal vector on the boundary in the global directions of  $X$  and  $Y$ . Eqn.4.15 can be written as:

$$U_n = \begin{bmatrix} \eta N_1 & \beta N_1 & \eta N_2 & \beta N_2 \end{bmatrix} \begin{bmatrix} u_1 \\ v_1 \\ u_2 \\ v_2 \end{bmatrix} \implies U_n = \left[ N_n^s \right]^T \left[ \delta \right] \quad (4.16)$$

In addition, fluid shape function can relate the pressure at each node of the interface element to the element pressure. Thus, if  $[N^f]$  is the fluid shape function, the relation between the nodal pressure and the element pressure can be expressed as:

$$P = \left[ N^f \right]^T \left[ P^e \right] = \begin{bmatrix} N_1^f & N_2^f \end{bmatrix} \begin{bmatrix} P_1 \\ P_2 \end{bmatrix} \quad (4.17)$$

By substituting Eqn.4.16 and Eqn.4.17 in Eqn.4.12, the virtual work equilibrium can be expressed as:

$$\left[ f^e \right] = \int_{se} \left[ N_n^s \right] \left[ N^f \right]^T ds \left[ P^e \right] = \left[ Q^e \right] \left[ P^e \right] \quad (4.18)$$

In Eqn.4.18,  $[Q^e]$  is the coupling matrix that relates the element pressure  $[P^e]$  to structural forces  $[f^e]$  at the interface element. For a two-dimensional interface element, the coupling matrix can be expressed as follows:

$$\begin{aligned}
[Q^e] &= \int_{se} [N_n^s] [N^f]^T ds \\
[Q^e] &= \int_{se} \begin{bmatrix} \eta N_1^s \\ \beta N_1^s \\ \eta N_2^s \\ \beta N_2^s \end{bmatrix} \begin{bmatrix} N_1^f & N_2^f \end{bmatrix} ds \\
[Q^e] &= \int_{se} \begin{bmatrix} \eta N_1^s N_1^f & \eta N_1^s N_2^f \\ \beta N_1^s N_1^f & \beta N_1^s N_2^f \\ \eta N_2^s N_1^f & \eta N_2^s N_2^f \\ \beta N_2^s N_1^f & \beta N_2^s N_2^f \end{bmatrix} ds \tag{4.19}
\end{aligned}$$

Eqn.4.19 is valid for a typical two-dimensional coupled system of fluid-structure, and for the elements that have two DOF at each node. Two-dimensional modelling of the system is a very simple and practical method in engineering problems. However, as mentioned before, for a more realistic simulation of the fluid-structure system, a three-dimensional model is preferred. The coupling matrix for a 3D system with a four node interface element that has three degrees of freedom of  $x$ ,  $y$ , and  $z$  at each node, can be written as:

$$[Q^e] = \omega \int_{-1}^1 \int_{-1}^1 \begin{bmatrix} \alpha_1 N_1^s N_1^s N_1^f & \alpha_1 N_1^s N_1^s N_2^f & \alpha_1 N_1^s N_1^s N_3^f & \alpha_1 N_1^s N_1^s N_4^f \\ \beta_1 N_1^s N_1^s N_1^f & \beta_1 N_1^s N_1^s N_2^f & \beta_1 N_1^s N_1^s N_3^f & \beta_1 N_1^s N_1^s N_4^f \\ \gamma_1 N_1^s N_1^s N_1^f & \gamma_1 N_1^s N_1^s N_2^f & \gamma_1 N_1^s N_1^s N_3^f & \gamma_1 N_1^s N_1^s N_4^f \\ \cdot & \cdot & \cdot & \cdot \\ \cdot & \cdot & \cdot & \cdot \\ \cdot & \cdot & \cdot & \cdot \\ \alpha_4 N_4^s N_1^s N_1^f & \alpha_4 N_4^s N_1^s N_2^f & \alpha_4 N_4^s N_1^s N_3^f & \alpha_4 N_4^s N_1^s N_4^f \\ \beta_4 N_4^s N_1^s N_1^f & \beta_4 N_4^s N_1^s N_2^f & \beta_4 N_4^s N_1^s N_3^f & \beta_4 N_4^s N_1^s N_4^f \\ \gamma_4 N_4^s N_1^s N_1^f & \gamma_4 N_4^s N_1^s N_2^f & \gamma_4 N_4^s N_1^s N_3^f & \gamma_4 N_4^s N_1^s N_4^f \end{bmatrix}_{24 \times 4} \times \|t_\xi \times t_\eta\| d\xi d\eta \tag{4.20}$$

In which:

$$t_\xi = \left\{ \frac{\partial x}{\partial \xi}, \frac{\partial y}{\partial \xi}, \frac{\partial z}{\partial \xi} \right\}$$

$$t_\eta = \left\{ \frac{\partial x}{\partial \eta}, \frac{\partial y}{\partial \eta}, \frac{\partial z}{\partial \eta} \right\}$$

$$\bar{\omega} = \frac{\int_{A_e} \|t_\xi \times t_\eta\| d\xi d\eta}{\sum_{i=1}^8 \int_{A_e} N_i^s N_i^s \|t_\xi \times t_\eta\| d\xi d\eta}$$

In Eqn.4.20,  $N_i^f$  is the shape function for the liquid and  $N_i^s$  is the shape function of the structure. Moreover,  $\alpha_i$ ,  $\beta_i$  and  $\gamma_i$  are the direction cosines of the nodes of the interface element at the interaction boundary.

### 4.2.3 Finite Element Modelling of the Liquid Domain

The governing equation of motion for the liquid in a moving rectangular tank was described in Chapter 3. Moreover, the boundary conditions at the interface of the fluid and structure domain as well as the one at the free water surface were discussed. Moreover, it was stated that the velocity potential,  $\Phi$ , should satisfy the wave equation at any point in the liquid domain, respecting the assumption of incompressible fluid as:

$$\frac{\partial \Phi(x, y, z, t)}{\partial n} = v_n(t) \quad \text{at boundary } \Gamma_1 \quad (4.21)$$

In Eqn.4.21,  $v_n(x, y, z, t)$  is the component of velocity on the boundary along the direction of the outward normal  $n$ . Then:

$$\nabla^2 \Phi(x, y, z, t) = 0 \quad (4.22)$$

Figure 4.3 represents the schematic illustration of the liquid domain and the boundaries. In cases that the tank motion is not rotational, and if the viscous stresses are negligible, the boundary condition at the wet surface of the tank wall is:

$$v_n = \frac{\partial w}{\partial t} \quad (4.23)$$

where  $w$  is the normal displacement of the structure.

Under horizontal ground motion, the linearized dynamic boundary conditions for the 3D model illustrated in Figure 3.1 is written in the form of Eqn.4.24 at the free surface of the liquid.

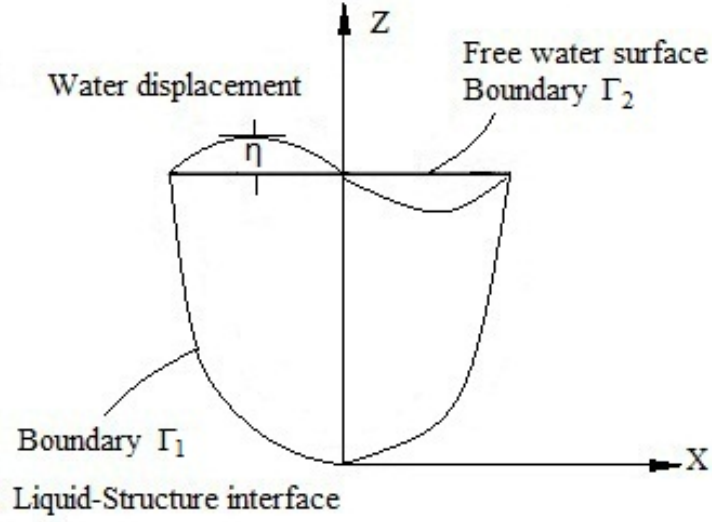


Figure 4.3: Schematic illustration of liquid domain and boundaries

$$\frac{1}{g} \frac{\partial^2 \Phi}{\partial t^2} + \frac{\partial \Phi}{\partial z} = 0 \quad \text{at boundary } \Gamma_2 \quad (4.24)$$

At the boundary  $\Gamma_2$ , if the sloshing displacement is denoted by  $\eta$ , pressure,  $P$ , in terms of sloshing can be calculated according to Eqn. 4.25. Note that in Eqn. 4.25,  $\rho$  is the fluid density.

$$\frac{P}{\rho} = -g\eta - \frac{\partial \Phi}{\partial t} \quad (4.25)$$

Using finite element formulation, the velocity potential,  $\Phi$ , is:

$$\Phi = \sum_{i=1}^n N_i(x, y, z) \cdot \Phi_i(t) \quad (4.26)$$

where  $N_i$  are the shape functions at the boundary element. Substituting equations 4.22, 4.21, 4.24 and 4.26, the weighted residual form of the governing equation might be expressed as:

$$\begin{aligned} & \int_V N_i \left[ \frac{\partial^2}{\partial x^2} + \frac{\partial^2}{\partial y^2} + \frac{\partial^2}{\partial z^2} \right] \sum N_j \Phi_j dV - \int_{\Gamma_1} N_i \frac{\partial}{\partial n} \sum N_j \Phi_j d\Gamma_1 \\ & + \int_{\Gamma_1} N_i v_n d\Gamma_1 - \int_{\Gamma_2} \left[ \frac{N_i}{g} \frac{\partial^2}{\partial t^2} \sum N_j \Phi_j + N_i \frac{\partial}{\partial z} \sum N_j \Phi_j \right] d\Gamma_2 = 0 \end{aligned} \quad (4.27)$$

And this equation can be expanded to Eqn.4.28:

$$\begin{aligned}
& \int_{\Gamma} N_i \left[ \sum \frac{\partial N_j}{\partial x} l_x \Phi_j + \sum \frac{\partial N_j}{\partial y} l_y \Phi_j + \sum \frac{\partial N_j}{\partial z} l_z \Phi_j \right] d\Gamma \\
& - \int_V \left[ \frac{\partial N_i}{\partial x} \sum \frac{\partial N_j}{\partial x} \Phi_j + \frac{\partial N_i}{\partial y} \sum \frac{\partial N_j}{\partial y} \Phi_j + \frac{\partial N_i}{\partial z} \sum \frac{\partial N_j}{\partial z} \Phi_j \right] dV \\
& = \int_{\Gamma_1} N_i \sum \frac{\partial N_j}{\partial n} \Phi_j d\Gamma_1 - \int_{\Gamma_1} N_i v_n d\Gamma_1 + \frac{1}{g} \int_{\Gamma_2} N_i \sum N_j \frac{\partial^2 \Phi_j}{\partial t^2} d\Gamma_2 + \int_{\Gamma_2} N_i \sum \frac{\partial N_j}{\partial z} \Phi_j d\Gamma_2 \quad (4.28)
\end{aligned}$$

Moreover,  $V$  is the element volume,  $\Gamma_1$  and  $\Gamma_2$  are the area across the boundaries as shown in Figure 4.3, and  $\Gamma^e = \Gamma_1 + \Gamma_2$ . If the small slopes are assumed at the interface of the liquid and structure, the following equation shall be formed:

$$\frac{\partial N_j}{\partial n} = \frac{\partial N_j}{\partial z} \quad \text{at} \quad \Gamma_2 \quad (4.29)$$

As a result, Eqn.4.28 can be rewritten as:

$$\begin{aligned}
& \int_V \left[ \frac{\partial N_i}{\partial x} \sum \frac{\partial N_j}{\partial x} \Phi_j + \frac{\partial N_i}{\partial y} \sum \frac{\partial N_j}{\partial y} \Phi_j + \frac{\partial N_i}{\partial z} \sum \frac{\partial N_j}{\partial z} \Phi_j \right] dV \\
& + \frac{1}{g} \int_{\Gamma_2} N_i \sum N_j \frac{\partial^2 \Phi_j}{\partial t^2} d\Gamma_2 = \int_{\Gamma_1} N_i v_n d\Gamma_1 \quad (4.30)
\end{aligned}$$

Therefore, using finite element formulation of the fluid domain and using the discretized formulation of Eqn.4.22, the wave equation can be written in the following form:

$$[G] [\ddot{P}] + [H] [P] = [F] \quad (4.31)$$

In Eqn.4.31,  $G_{i,j} = \sum G_{i,j}^e$  and  $H_{i,j} = \sum H_{i,j}^e$  are constant coefficient for each element. Those

coefficients can be calculated according to Eqn. 4.32 and Eqn. 4.33, respectively. Coefficient  $F_i = \sum F_i^e$  can be calculated from Eqn. 4.34, at each step of the analysis for individual element. Again,  $P$  is also the pressure vector.

$$G_{i,j}^e = \frac{1}{g} \int_{\Gamma^e} N_i \sum N_j d\Gamma \quad (4.32)$$

$$H_{i,j}^e = \int_{V^e} \left( \frac{\partial N_i}{\partial x} \sum \frac{\partial N_j}{\partial x} + \frac{\partial N_i}{\partial y} \sum \frac{\partial N_j}{\partial y} + \frac{\partial N_i}{\partial z} \sum \frac{\partial N_j}{\partial z} \right) dV \quad (4.33)$$

$$F_i^e = \int_{\Gamma^e} N_i \frac{\partial P}{\partial n} d\Gamma \quad (4.34)$$

Note that in Eqn. 4.31,  $F$  is the force acting on the liquid domain. As was mentioned before, this force depends on the boundary condition and at the interface element,  $F$  can be calculated obtained from Eqn. 4.35 as:

$$[F] = -\rho [Q]^T (\{\ddot{U}\} + \{\ddot{U}_g\}) \quad (4.35)$$

In Eqn. 4.35,  $[Q]$  is the coupling matrix that relates the pressure of the liquid to the equivalent nodal structural forces and reverse.  $\{\ddot{U}\}$  is the acceleration vector of the nodes at the boundary element in the structural domain, and  $\{\ddot{U}_g\}$  is the ground acceleration vector applied to the system. Therefore, equation of the motion for the interface element in the fluid domain can be written as:

$$[G] [\ddot{P}] + [C'] [\dot{P}] + [H] [P] = -\rho [Q]^T (\{\ddot{U}\} + \{\ddot{U}_g\}) \quad (4.36)$$

If in Eqn. 4.36,  $[F_2] = -\rho [Q]^T \{\ddot{U}_g\}$ , the equation of motion for the fluid domain can be expressed as:

$$[G] [\ddot{P}] + [C'] [\dot{P}] + [H] [P] = [F_2] - \rho [Q]^T \{\ddot{U}\} \quad (4.37)$$

#### 4.2.4 Solution of the Moving Liquid-Tank System in Time Domain

Now that the equation of motion for the liquid domain, the equation of motion for the structure domain, as well as the coupling matrix for this coupled system, is identified, displacement and pressure can be obtained for each time step. For much of this conversation, Eqn.4.9 and Eqn.4.37 has been combined to create a matrix formulation as Eqn.4.39:

$$\begin{bmatrix} M & 0 \\ \rho Q^T & G \end{bmatrix} \begin{bmatrix} \ddot{U} \\ \ddot{P} \end{bmatrix} + \begin{bmatrix} C & 0 \\ 0 & C' \end{bmatrix} \begin{bmatrix} \dot{U} \\ \dot{P} \end{bmatrix} + \begin{bmatrix} K & -Q \\ 0 & H \end{bmatrix} \begin{bmatrix} U \\ P \end{bmatrix} = \begin{bmatrix} F_1 \\ F_2 \end{bmatrix} \quad (4.38)$$

This equation can be expressed as:

$$[M] \begin{bmatrix} \ddot{U} \\ \ddot{P} \end{bmatrix} + [C] \begin{bmatrix} \dot{U} \\ \dot{P} \end{bmatrix} + [K] \begin{bmatrix} U \\ P \end{bmatrix} = \begin{bmatrix} F_1 \\ F_2 \end{bmatrix} \quad (4.39)$$

Among different time-stepping method, Newmark's method will be employed. Accordingly, parameters from Eqn.4.39 and their derivations can be solved based on following equations:

$$\begin{bmatrix} \dot{U} \\ \dot{P} \end{bmatrix}_{i+1} = \begin{bmatrix} \dot{U} \\ \dot{P} \end{bmatrix}_i + [(1-\gamma)\Delta t] \begin{bmatrix} \dot{U} \\ \dot{P} \end{bmatrix}_i + (\gamma\Delta t) \begin{bmatrix} \dot{U} \\ \dot{P} \end{bmatrix}_{i+1} \quad (4.40)$$

$$\begin{bmatrix} U \\ P \end{bmatrix}_{i+1} = \begin{bmatrix} U \\ P \end{bmatrix}_i + (\Delta t) \begin{bmatrix} \dot{U} \\ \dot{P} \end{bmatrix}_i + [(0.5-\beta)(\Delta t)^2] \begin{bmatrix} \ddot{U} \\ \ddot{P} \end{bmatrix}_i + [\beta(\Delta t)^2] \begin{bmatrix} \ddot{U} \\ \ddot{P} \end{bmatrix}_{i+1} \quad (4.41)$$

Where typical selection for  $\gamma$  is  $1/2$  and  $\frac{1}{6} \leq \beta \leq \frac{1}{4}$ . To avoid iteration and to use incremental quantities, equations 4.40 and 4.41 can be rewritten. As follows, the steps for this method will be explained:

$$\Delta \begin{bmatrix} U \\ P \end{bmatrix} \equiv \begin{bmatrix} U \\ P \end{bmatrix}_{i+1} - \begin{bmatrix} U \\ P \end{bmatrix}_i \quad \Delta \begin{bmatrix} \dot{U} \\ \dot{P} \end{bmatrix} \equiv \begin{bmatrix} \dot{U} \\ \dot{P} \end{bmatrix}_{i+1} - \begin{bmatrix} \dot{U} \\ \dot{P} \end{bmatrix}_i \quad (4.42)$$

$$\Delta \begin{bmatrix} \ddot{U} \\ \ddot{P} \end{bmatrix} \equiv \begin{bmatrix} \ddot{U} \\ \ddot{P} \end{bmatrix}_{i+1} - \begin{bmatrix} \ddot{U} \\ \ddot{P} \end{bmatrix}_i \quad \Delta \begin{bmatrix} F_1 \\ F_2 \end{bmatrix} \equiv \begin{bmatrix} F_1 \\ F_2 \end{bmatrix}_{i+1} - \begin{bmatrix} F_1 \\ F_2 \end{bmatrix}_i \quad (4.43)$$

1.  $a = \frac{1}{\beta \Delta t} [M] + \frac{\gamma}{\beta} [C] \quad b = \frac{1}{2\beta} [M] + \Delta t \left( \frac{\gamma}{2\beta} - 1 \right) [C]$
2.  $\Delta \begin{bmatrix} \hat{F}_1 \\ \hat{F}_2 \end{bmatrix}_i = \Delta \begin{bmatrix} F_1 \\ F_2 \end{bmatrix}_i + a \begin{bmatrix} \dot{U} \\ \dot{P} \end{bmatrix}_i + b \begin{bmatrix} \ddot{U} \\ \ddot{P} \end{bmatrix}_i$
3.  $\Delta \begin{bmatrix} U \\ P \end{bmatrix}_i = \Delta \begin{bmatrix} \hat{F}_1 \\ \hat{F}_2 \end{bmatrix}_i / [\hat{K}]$
4.  $\Delta \begin{bmatrix} \dot{U} \\ \dot{P} \end{bmatrix}_i = \frac{\gamma}{\beta \Delta t} \Delta \begin{bmatrix} U \\ P \end{bmatrix}_i - \frac{\gamma}{\beta} \begin{bmatrix} \dot{U} \\ \dot{P} \end{bmatrix}_i + \Delta t \left( 1 - \frac{\gamma}{2\beta} \right) \begin{bmatrix} \ddot{U} \\ \ddot{P} \end{bmatrix}_i$
5.  $\Delta \begin{bmatrix} \ddot{U} \\ \ddot{P} \end{bmatrix}_i = \frac{1}{\beta (\Delta t)^2} \Delta \begin{bmatrix} U \\ P \end{bmatrix}_i - \frac{1}{\beta \Delta t} \begin{bmatrix} \dot{U} \\ \dot{P} \end{bmatrix}_i - \frac{1}{2\beta} \begin{bmatrix} \ddot{U} \\ \ddot{P} \end{bmatrix}_i$
6.  $\begin{bmatrix} U \\ P \end{bmatrix}_{i+1} = \begin{bmatrix} U \\ P \end{bmatrix}_i + \Delta \begin{bmatrix} \dot{U} \\ \dot{P} \end{bmatrix}_i + \frac{\Delta^2}{2} \begin{bmatrix} \ddot{U} \\ \ddot{P} \end{bmatrix}_i \quad \begin{bmatrix} \dot{U} \\ \dot{P} \end{bmatrix}_{i+1} = \begin{bmatrix} \dot{U} \\ \dot{P} \end{bmatrix}_i + \Delta \begin{bmatrix} \ddot{U} \\ \ddot{P} \end{bmatrix}_i \quad \begin{bmatrix} \ddot{U} \\ \ddot{P} \end{bmatrix}_{i+1} = \begin{bmatrix} \ddot{U} \\ \ddot{P} \end{bmatrix}_i + \Delta \begin{bmatrix} \dddot{U} \\ \dddot{P} \end{bmatrix}_i$

This implicit method shall be started from the time step ( $i = 1$ ), as the tank is in the stationary position, to calculate the initial parameters. Then, repetition shall be done for the next time step, ( $i + 1$ ). It should be noted that, for the Newmark formulation, parameters of  $\beta = 0.505$  and  $\gamma = 0.252$  are used in ANSYS program. These values are satisfactory within the scope of this study in term of stability and accuracy. Further information on the direct integration method can be found in studies reported by Bathe(1999) and Zienkiewisc (1977). Also, other methods for the time stepping analysis are discussed by Chopra (1995).

# Chapter 5

## Dynamic Response of Rectangular Tanks: FEM Modelling, Results and Discussions

### 5.1 Introduction

This chapter is divided into seven sections. In this chapter, the effects of three-dimensional geometry on the dynamic response of the partially filled rectangular water tanks are discussed. Parametric studies are conducted to investigate the effect of different factors such as tank plan dimensions, water level, and ground motion frequency content on the dynamic response of the 3D water tanks. The results of finite element analysis are presented for twenty seven rectangular tank configurations.

In this study, ANSYS (version 12.1) finite element program is used for the analysis purposes. Finite element implementation of the partially filled rectangular tank in ANSYS program, for both two-dimensional and three-dimensional geometries, are presented in section 5.2. Mesh sensitivity of the model is discussed in section 5.2.1.

In section 5.3, the results of modal analysis on the flexible 2D and 3D rectangular tanks are presented. The modal analysis of free liquid oscillations in a partially filled container is employed to determine the free surface natural frequencies and the corresponding free surface mode shapes. The fundamental frequencies of impulsive mode of vibration are also calculated. The values of natural frequencies and effective mass ratios are conducted and compared with those according to current practice.

In section 5.4, time history analysis are conducted on both 2D and 3D tank models using finite element method (FEM). The sloshing heights of water are calculated at the critical locations. To investigate the effects of 3D geometry on the response of externally excited tanks, the results of 3D models are compared with the corresponding 2D simulations and are presented.

Moreover, in the 3D models, in order to investigate the effects of interaction of waves at the corner, the sloshing height is also calculated at the corner of the rectangular tanks and are compared with the sloshing heights at other locations. Two comparisons are made for each tank model: First, in order to introduce a practical method for design free-board, the peak sloshing height at the corner of the tank is compared with the peak sloshing heights at the middle of the walls. Second, to investigate the occurrence of constructive or destructive interference, at the time that the peak sloshing height occurs at the corner of the tank, that value is compared with the sloshing heights in  $X$  and  $Y$  directions.

Later, the effects of the frequency content of the ground motion on the sloshing response of the 3D tank models are investigated. For this purpose, time history analysis are conducted on three rectangular tanks by applying three different ground motions. Moreover, by subjecting the rectangular tank models to two different external excitation, the effects of the frequency content of the earthquake on the amplification of the sloshing height at the corners relative to those at the middle of the walls are investigated. Finally, sloshing heights calculated in this study are compared with available methods in literature and to the results of the ACI 350.3-06 code.

In section 5.5, by introducing flexible boundary condition, the hydrodynamic pressure distribution is calculated along the wall height of 3D tank models. The results are compared with corresponding 2D models to determine the effect of 3D restraint condition on the hydrodynamic pressure. Pressure distributions are also estimated for the 2D rigid tanks. The lateral distribution of the hydrodynamic pressure is also presented. For 2D rigid tanks, distribution of the impulsive component of the hydrodynamic pressure is compared with the analytical method.

Moreover in section 5.6, the resulting base shear and base moments are computed using FEM. Time histories of the impulsive and convective components of the base shear and the overturning moment at the ground level are presented and are compared with the results of the 2D models.

## 5.2 Application of Finite Element Program

There are different methods available to apply finite element approach to simulate liquid motion in tanks. First, to model the sections assuming plane strain behaviour. In that case, two-dimensional grids can be employed to model the cross section of the tank parallel to  $X$  direction as well as the one parallel to  $Y$  direction, separately. Second method is the subdivision of the total liquid into small volumes, which produces a three-dimensional mesh. In this study, the liquid-tank system is modelled in both 2D and 3D geometries.

The rectangular concrete water tank shown in Figure 5.1 is the subject of the study. The cross section parallel to the short side wall is adopted for  $X$  direction, along with the cross section parallel to the long side as  $Y$  direction. Twenty seven tank configurations are modelled in ANSYS (version 12.1) program. Different tank configurations and their symbols are presented in Table 5.1. As follows, in this thesis,  $H_w$  and  $t_w$  represent the height and thickness of the tank wall, respectively.  $2L_x$  and  $2L_y$  represent inside dimension of the tank wall for shorter and longer side wall, respectively.  $H_L$  is also the water depth, and  $H_{top}$  is the height of the empty portion of the tank. Points  $A$  and  $B$  are located at the water surface at the middle cross section of longer and shorter side walls, respectively. Point  $C$  is at free water surface at the corner of the rectangular tank between points  $A$  and  $B$ .

Tank identifying symbols summarized in Table 5.1 contain three items. First parameter is a letter such as  $S$ ,  $M$  and  $T$ , symbolizing tanks with water level of 5.5, 8.0, and 11.0m, respectively. Second parameter starts with letter  $X$ , followed by a two digit number, demonstrating dimension of the tank wall parallel to  $X$  direction and the third parameter starts with letter  $Y$  representing the dimension of the tank wall parallel to  $Y$  direction followed by a two digit number.

Tanks are divided into three groups. Group 1, Group 2 and Group 3 of tanks, which contain tanks with shorter side wall dimension of 20m, 30m and 40m, respectively. It should be noted that tanks in groups 1 and 2 have a wall thickness of 600mm and tanks in group 3, 1200mm. Moreover, tank height,  $H_w$ , in groups 1, 2 and 3 are 6.0, 8.5 and 12.0m, respectively.

Material properties for the structure domain and the fluid domain are as follows:

$$\text{Structure domain: } \quad \rho_c = 2300 \text{ kg/m}^3 \quad E_c = 2.644 \times 10^{10} \text{ Pa} \quad \nu = 0.17$$

$$\text{Fluid domain: } \quad \rho_l = 1000 \text{ kg/m}^3 \quad B_l = 2.1 \times 10^9 \text{ Pa}$$

Where  $\rho_c$ ,  $E_c$  and  $\nu$  are density, modulus of elasticity and Poisson's ratio for the tank structure.

$\rho_l$  and  $B_l$  are density and bulk modulus of the fluid domain.

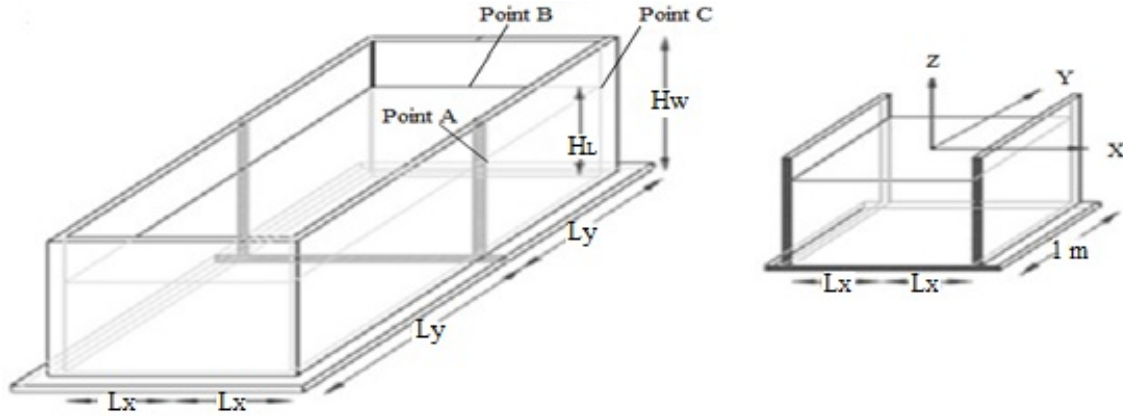


Figure 5.1: Schematic configuration of the tank

Table 5.1: Selected tank configurations for this study

	Shallow ( $H_L = 5.5\text{ m}$ )		Medium ( $H_L = 8.0\text{ m}$ )		Tall ( $H_L = 11\text{ m}$ )				
	$H_w = 6.0\text{ m}, t_w = 0.6\text{ m}$		$H_w = 8.5\text{ m}, t_w = 0.6\text{ m}$		$H_w = 12\text{ m}, t_w = 1.2\text{ m}$				
	$2L_x$	$2L_y$	$2L_x$	$2L_y$	$2L_x$	$2L_y$			
Group 1	SX20Y40	20	40	MX20Y40	20	40	TX20Y40	20	40
	SX20Y60	20	60	MX20Y60	20	60	TX20Y60	20	60
	SX20Y80	20	80	MX20Y80	20	80	TX20Y80	20	80
Group 2	SX30Y40	30	40	MX30Y40	30	40	TX30Y40	30	40
	SX30Y60	30	60	MX30Y60	30	60	TX30Y60	30	60
	SX30Y80	30	80	MX30Y80	30	80	TX30Y80	30	80
Group 3	SX40Y40	40	40	MX40Y40	40	40	TX40Y40	40	40
	SX40Y60	40	60	MX40Y60	40	60	TX40Y60	40	60
	SX40Y80	40	80	MX40Y80	40	80	TX40Y80	40	80

For three-dimensional modelling, the tank is assumed to be a symmetric structure with four side flexible walls. It is also assumed that the tank is anchored at its base, and the effect of uplift pressure is ignored. Tanks are assumed to be rigidly attached to rock foundation, and the soil-structure interaction effect is neglected. Tank walls are modelled as iso-parametric solid elements (Solid 45 - ANSYS program) with eight nodes, which have three degrees of freedom (DOF) at each node. The liquid domain is also modelled by three-dimensional iso-parametric fluid elements (Fluid 80 - ANSYS program) having three DOF at each of eight nodes.

It should be noted that Fluid 80 elements include special surface effects, which may be thought of as gravity springs used to hold the surface in place. This is performed by adding springs to each node, with the spring constants being positive on the top of the element, and negative on the bottom. Note that gravity springs are located only on the face of elements located at the free surface plane. Gravitational acceleration is applied on the tanks used in this study, since they are open top tanks. It should be noted that fluid elements at a boundary are not attached directly to structural elements; but, they have separate, coincident nodes that are coupled only in the direction normal to the interface. Couplings are applied at the wet surface of the wall as well as the bottom of the tank. Figure 5.2 shows the schematic illustration of a 3D iso-parametric solid/fluid element as well as the finite element simulation of the whole tank in 3D space.

It is observed that the accuracy of the finite element method depends on the number of elements. In order to achieve a reasonable mesh size for the dynamic analysis, length of the walls are divided into 30 elements in  $X$  direction. The walls parallel to  $Y$  direction are also divided into 60 number of elements. This discretizing is employed for both structure and fluid domain. In both  $X$  and  $Y$  directions, mesh ratio of 15 is employed; therefore, the size of the elements closer to walls are smaller than those in the middle of the tank. Moreover, the water depth is divided into 22 segments, and the portion of the wall that is in contact with the contained water is also divided into 22 elements.  $H_{top}$  is also divided into two elements for groups 1 and 2, where  $H_{top}$  is also divided to four elements for group 3. Wall thickness and the bottom slab are divided into two elements for groups 1 and 2, where they are divided into four elements for tanks in group 3.

Additionally, in order to obtain two-dimensional modelling, the structure is simulated using four-node elements (Plane 42 - ANSYS program) with two DOF; translations in  $X$  and  $Y$  direction at each node. In 2D models, tanks are assumed to have plane strain behaviour. To get more accurate results in 2D plane strain models, fluid domain is modelled with both four-node iso-parametric element (Fluid 79 - ANSYS program) as well as the four node acoustic element (Fluid 29 - ANSYS program). The 4-node acoustic element has the DOF of pressure at each node. Acoustic element is used to calculate the resulting forces and moments, as well as the hydrodynamic pressure distribution along the height of the walls. On the other hand, iso-parametric elements are employed to estimate the sloshing height. It should be noted that Fluid 79 element similarly includes surface effects.

In 2D models, when the Fluid 79 element is used for introducing the fluid domain, the length of the tank is divided to 240 elements. In those cases, finer mesh is used to calculate more accurate value for the sloshing height. However, as the acoustic element has the DOF of pressure at each

node, coarser mesh is used to reduce the computational effort. In this case, both liquid domain and the structure are divided into 60 elements in the horizontal direction. Other parameters such as  $H_{top}$ ,  $H_L$ ,  $H_f$  and  $t_w$  are following the same divisions as the 3D models, as was described earlier. Figure 5.3 illustrates the finite element simulation of the tank for 2D geometries as well as the schematic figure for a 2D acoustic element.

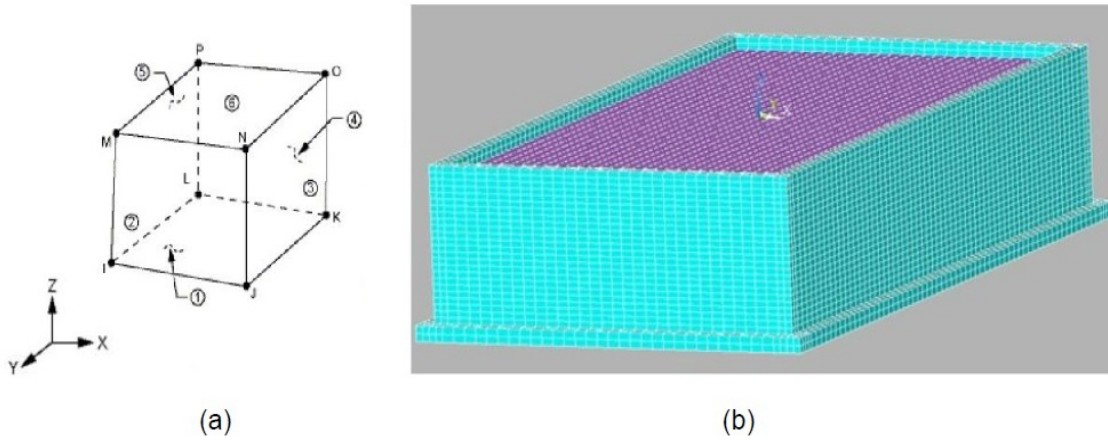


Figure 5.2: (a) Schematic 3D, 8-node iso-parametric element, (b) 3D model of a partially filled rectangular tank

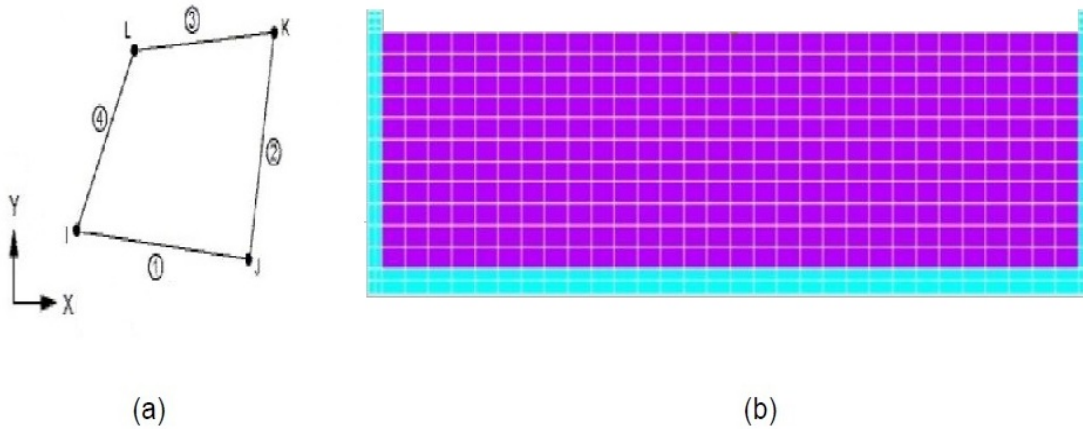


Figure 5.3: (a) 2D acoustic element, (b) Two dimensional model of a partially filled rectangular tank

### 5.2.1 Mesh Sensitivity

Finite element methods have been used for many years with success in the analysis of complex structures. Accuracy and convergence properties of these models should be investigated when

these models are used to represent a structure. Accuracy studies are usually based on the numerical solution for restricted problems for comparison with known results. Convergence studies are carried out to investigate the numerical results as the number of elements increase.

As the first step of this study, the possible error is to be estimated by selecting the appropriate mathematical model to represent the object being analyzed. The mathematical model for this study is derived in Chapter 3 for a rigid rectangular tank. Same model is used to calculate the maximum pressure at the bottom of rigid tank. The analysis goal is to compute the exact solution of bottom pressure named  $P_{ex}$  and then calculate its value using FEM which is  $P_{fem}$ . It should be noted that the term  $P_{ex}$  depends only on the definition of the mathematical model and not on the method used for finding an approximate solution. Therefore, it does not depend on mesh quality, type, and size of elements. The FE pressure at the bottom of two rigid tank models are compared with the exact solutions. It should be noted that the convergence study is done on cases SX30Y60 and TX20Y60.

FEM error can be found according to:

$$error = \frac{P_{ex} - P_{fem}}{P_{ex}} \quad (5.1)$$

The variations of ratio of the FE bottom pressure to the analytical pressure with the number of mesh divisions are shown in Figure 5.4 for 2D rigid shallow and tall tank models. It is found that the discretization errors are equal to 1.66 and 0.03 percent for the proposed 2D models with water level of 5.5 and 11.0m, respectively. This range of error is acceptable for numerical analysis. A detailed comparison between analytical and FE results will be discussed later in Section 5.5.

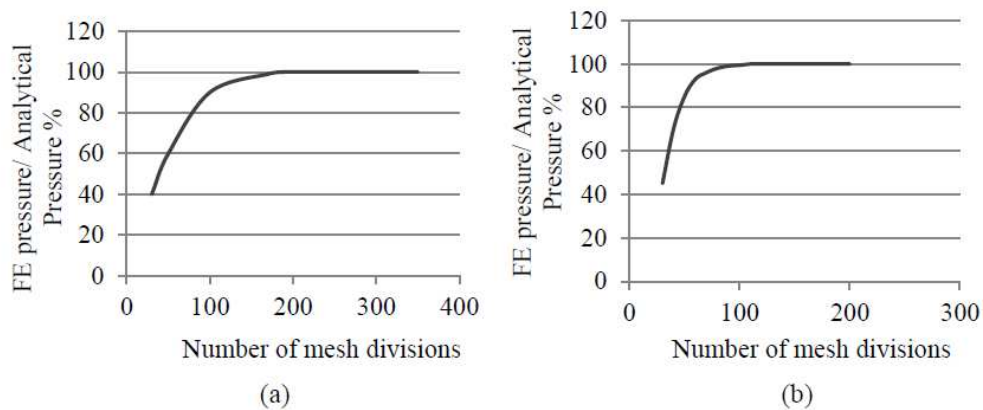


Figure 5.4: Finite element discretization error: (a) 2D shallow tank model (b) 2D tall tank model

### 5.3 Modal Analysis

Sloshing is defined as any motion of the free liquid surface inside its container, and it is caused by any disturbance to a partially filled liquid container. It should be noted that the liquid surface in a partially filled container can move back and forth at infinite number of natural frequencies, but it is the lowest few modes that are most likely to be excited by the ground motion.

In this section, modal analysis is employed to determine the free surface natural frequencies and the corresponding free surface mode shapes. Figure 5.5 represents the mode shape related to the first fundamental mode of sloshing for a typical 3D tank model. This figure shows the fundamental anti-symmetric wave. This mode has the lowest natural frequency. It is worth mentioning that, at the first anti-symmetric mode, the wave has zero amplitude at the centre of the tank ( $x = 0$ ). This leads to a positive peak at one wall, and a negative peak at the apposite wall. For higher sloshing modes, there are intermediate peaks, and the number of peaks increases with number of modes.

Figure 5.6 shows a sketch of the first three modes and the relative shift of the centre of gravity of the contained liquid. It is noticed that for the same maximum wave amplitude, the centre of gravity shift, for the fundamental mode ( $n = 1$ ), is substantially greater than that of the other modes. Since the centre of mass oscillation is the source of the slosh-induced forces, the wave corresponding to the first mode of sloshing produces a much greater force than any other modes.

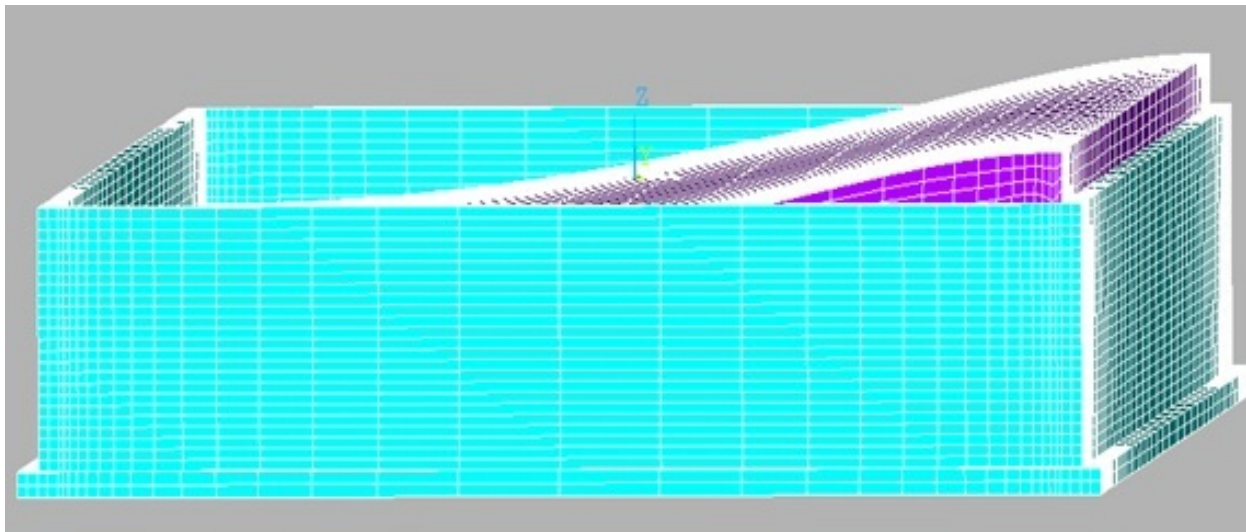


Figure 5.5: Mode shape related to the first fundamental mode of sloshing for a typical 3D model

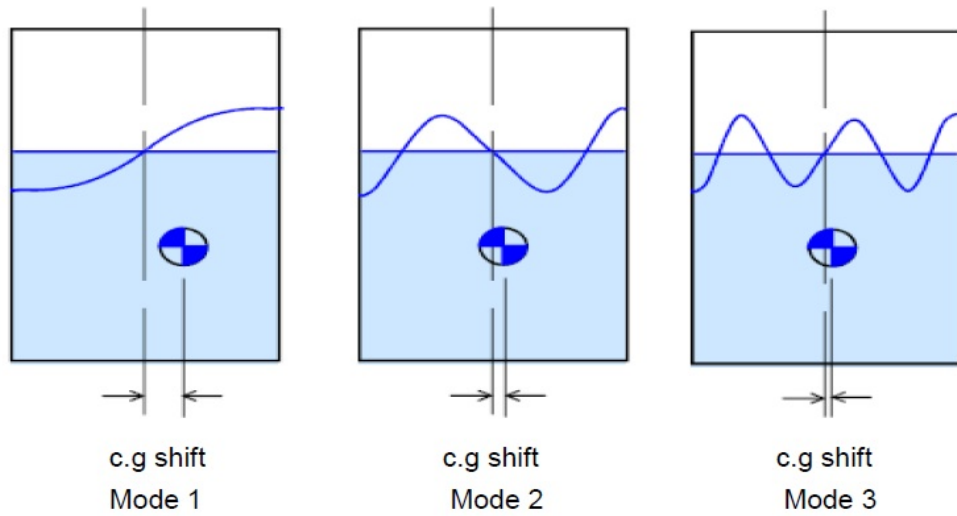


Figure 5.6: First three sloshing mode shapes

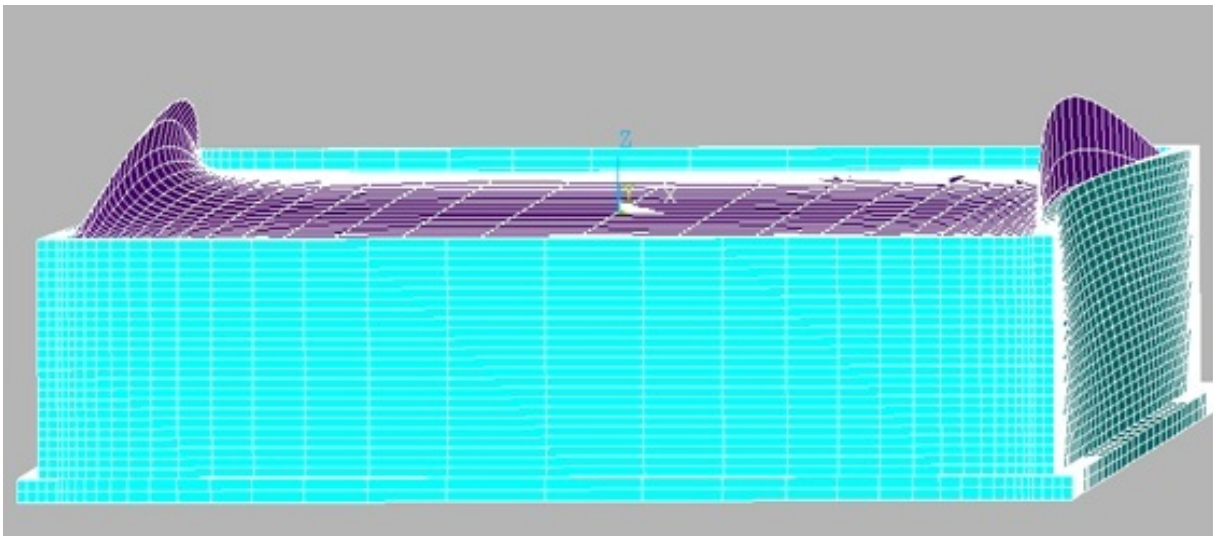


Figure 5.7: Mode shape related to the impulsive mode for a typical 3D model

In this study, natural frequencies and mode shapes for the impulsive modes are also calculated. Figure 5.7 is the mode shape for the impulsive mode.

The natural periods of the first mode of sloshing and the impulsive mode, as well as the mass ratios corresponding to those modes are calculated using FEM. Results are summarized in Tables 5.2, 5.3 and 5.4 for the 3D models of shallow, medium and tall tanks, respectively. More detailed discussions on the calculations of the natural frequencies are described in Chapter 3.

Table 5.2: Time periods and mass ratios for 3D Shallow tanks with  $H_L = 5.5m$

Case	Convective		Impulsive		Convective		Impulsive	
	X				Y			
	$T_c$	$m_c/m$	$T_i$	$m_i/m$	$T_c$	$m_c/m$	$T_i$	$m_i/m$
	<i>sec</i>		<i>sec</i>		<i>sec</i>		<i>sec</i>	
SX20Y40	6.05	0.433	0.147	0.158	11.22	0.507	0.117	0.058
SX20Y60	6.05	0.442	0.153	0.162	16.56	0.535	0.119	0.052
SX20Y80	6.05	0.446	0.155	0.164	21.96	0.546	0.118	0.0341
SX30Y40	8.56	0.504	0.147	0.110	11.22	0.527	0.139	0.081
SX30Y60	8.56	0.515	0.153	0.113	16.56	0.556	0.137	0.039
SX30Y80	8.56	0.520	0.155	0.114	21.96	0.568	0.139	0.041
SX40Y40	11.22	0.534	0.147	0.079	11.22	0.534	0.147	0.079
SX40Y60	11.22	0.549	0.153	0.086	16.56	0.567	0.147	0.056
SX40Y80	11.22	0.554	0.155	0.087	21.96	0.580	0.148	0.013

Table 5.3: Time periods and mass ratios for 3D Medium tanks with  $H_L = 8.0m$

Case	Convective		Impulsive		Convective		Impulsive	
	X				Y			
	$T_c$	$m_c/m$	$T_i$	$m_i/m$	$T_c$	$m_c/m$	$T_i$	$m_i/m$
	<i>sec</i>		<i>sec</i>		<i>sec</i>		<i>sec</i>	
MX20Y40	5.49	0.387	0.293	0.212	9.60	0.51	0.196	0.091
MX20Y60	5.49	0.396	0.318	0.215	13.95	0.55	0.204	0.070
MX20Y80	5.50	0.400	0.328	0.217	18.38	0.57	0.200	0.050
MX30Y40	7.50	0.487	0.294	0.150	9.60	0.53	0.265	0.110
MX30Y60	7.50	0.498	0.319	0.153	13.95	0.58	0.261	0.058
MX30Y80	7.50	0.503	0.329	0.155	18.37	0.60	0.264	0.057
MX40Y40	9.60	0.484	0.295	0.115	9.60	0.48	0.295	0.115
MX40Y60	9.60	0.551	0.320	0.118	13.95	0.59	0.295	0.076
MX40Y80	9.60	0.557	0.329	0.119	18.37	0.61	0.299	0.015

Table 5.4: Time periods and mass ratios for 3D Tall tanks with  $H_L = 11.0m$

Case	Convective		Impulsive		Convective		Impulsive	
	X				Y			
	$T_c$	$m_c/m$	$T_i$	$m_i/m$	$T_c$	$m_c/m$	$T_i$	$m_i/m$
	<i>sec</i>		<i>sec</i>		<i>sec</i>		<i>sec</i>	
TX20Y40	5.22	0.251	0.227	0.258	8.57	0.374	0.126	0.128
TX20Y60	5.23	0.260	0.262	0.261	12.17	0.433	0.135	0.096
TX20Y80	5.23	0.265	0.275	0.263	15.88	0.460	0.130	0.069
TX30Y40	6.85	0.352	0.230	0.194	8.57	0.400	0.196	0.143
TX30Y60	6.86	0.365	0.265	0.198	12.17	0.463	0.188	0.080
TX30Y80	6.86	0.372	0.278	0.201	15.88	0.493	0.193	0.077
TX40Y40	8.57	0.412	0.229	0.150	8.57	0.412	0.229	0.150
TX40Y60	8.57	0.430	0.264	0.156	12.17	0.480	0.231	0.099
TX40Y80	8.57	0.430	0.279	0.158	15.88	0.493	0.226	0.059

Modal analysis is also conducted for the 2D models. The periods are calculated for the fundamental convective and impulsive modes using FEM. These values are as well estimated according to ACI 350.3-06 code for seismic design of concrete LCS and according to the Potential Function (PF) approach. They are summarized in Tables 5.5, 5.6 and 5.7 for the shallow, medium and tall 2D tank models, respectively. It should be noted that the code values are very similar to those of analytical results.

For the 2D models, comparison of the results from FEM and ACI code and potential function (PF) approach shows that the FE results are in a good agreement with the analytical value for the convective component. This is mainly because in this study, the linearized wave equation is used in FE method similar to PF method and ACI code. Although the value of the convective mode periods calculated by FEM are slightly higher than PF method and ACI code, which is due to flexibility of the wall.

On the other hand, the impulsive components are calculated based on lumped mass assumption according to ACI code and fluid is assumed to be rigidly attached to the cantilever wall; however, in the FEM, the coupled systems (as discussed in chapter 4) are solved with flexible wall boundary conditions. As a result, some discrepancies are observed between the natural frequencies and the mass ratios for the impulsive responses.

More details on the calculation of the sloshing frequencies and mass ratios are available in literature by Karamanos et al. (2006) and Patkas and Karamanos (2007).

Table 5.5: Natural frequencies, time periods and mass ratios for 2D Shallow tanks

		Convective					Impulsive				
		PF		FEM		ACI		FEM		ACI	
$L$	$T_c$	$f_c$	$T_c$	$m_c/m$	$T_c$	$m_c/m_l$	$f_i$	$T_i$	$m_i/m$	$T_i$	$m_i/m_l$
$m$	<i>sec</i>	<i>Hz</i>	<i>sec</i>		<i>sec</i>		<i>Hz</i>	<i>sec</i>		<i>sec</i>	
20	6.06	0.17	6.06	0.46	6.03	0.67	6.42	0.156	0.036	0.10	0.79
30	8.60	0.12	8.62	0.52	8.56	0.75	6.42	0.156	0.028	0.10	0.81
40	11.22	0.09	11.22	0.57	11.17	0.79	6.42	0.156	0.019	0.10	0.82
60	16.56	0.06	16.57	0.60	16.48	0.81	6.42	0.155	0.023	0.10	0.11
80	21.95	0.05	21.96	0.62	21.84	0.82	6.42	0.156	0.046	0.10	0.08

Table 5.6: Natural frequencies, time periods and mass ratios for 2D Medium tanks

		Convective					Impulsive				
		PF		FEM		ACI		FEM		ACI	
$L$	$T_c$	$f_c$	$T_c$	$m_c/m$	$T_c$	$m_c/m_l$	$f_i$	$T_i$	$m_i/m$	$T_i$	$m_i/m_l$
$m$	<i>sec</i>	<i>Hz</i>	<i>sec</i>		<i>sec</i>		<i>Hz</i>	<i>sec</i>		<i>sec</i>	
20	5.49	0.18	5.50	0.42	5.47	0.56	2.97	0.34	0.28	0.22	0.45
30	7.49	0.13	7.51	0.52	7.46	0.68	2.96	0.34	0.20	0.22	0.31
40	9.59	0.10	9.61	0.58	9.55	0.74	2.96	0.34	0.15	0.22	0.23
60	13.93	0.07	13.95	0.63	13.86	0.79	2.96	0.34	0.11	0.22	0.15
80	18.35	0.05	18.37	0.65	18.26	0.81	2.96	0.33	0.08	0.22	0.12

Table 5.7: Natural frequencies, time periods and mass ratios for 2D Tall tanks

		Convective					Impulsive				
		PF		FEM		ACI		FEM		ACI	
$L$	$T_c$	$f_c$	$T_c$	$m_c/m$	$T_c$	$m_c/m_l$	$f_i$	$T_i$	$m_i/m$	$T_i$	$m_i/m_l$
$m$	<i>sec</i>	<i>Hz</i>	<i>sec</i>		<i>sec</i>		<i>Hz</i>	<i>sec</i>		<i>sec</i>	
20	5.22	0.19	5.23	0.28	5.21	0.45	3.25	0.31	0.35	0.18	0.58
30	6.85	0.15	6.86	0.39	6.83	0.59	3.22	0.31	0.26	0.19	0.42
40	8.57	0.12	8.57	0.46	8.53	0.67	3.21	0.31	0.21	0.19	0.32
60	12.16	0.08	12.17	0.53	12.10	0.75	3.21	0.31	0.15	0.36	0.21
80	15.87	0.06	15.88	0.57	15.97	0.79	3.21	0.31	0.11	0.36	0.16

## 5.4 Time History Analysis

In this section, the seismic responses of partially filled rectangular tanks under external excitations in both longitudinal and transverse directions are investigated. Time history analyses are conducted to calculate the response of the systems at each time step. FEM is employed to calculate sloshing heights for the 2D and 3D models. In this section, the variations of the wave amplitude with time are discussed.

For the three-dimensional tank model, the cross-section parallel to the short side wall is adopted for  $X$  direction and N-S component of El-Centro (1940) earthquake is applied. The direction parallel to the long side wall is also adopted for  $Y$  direction and is subjected to the E-W component of El-Centro (1940) earthquake. The components of the El-Centro (1940) earthquake record are scaled in such a way that the peak ground acceleration of the N-S component is  $0.4g$ , and that of E-W component is  $0.27g$  and are shown in Figure 5.8. To reduce the computational efforts, analyses are done for the first 20 seconds of the excitation, with time intervals of 0.02 seconds.

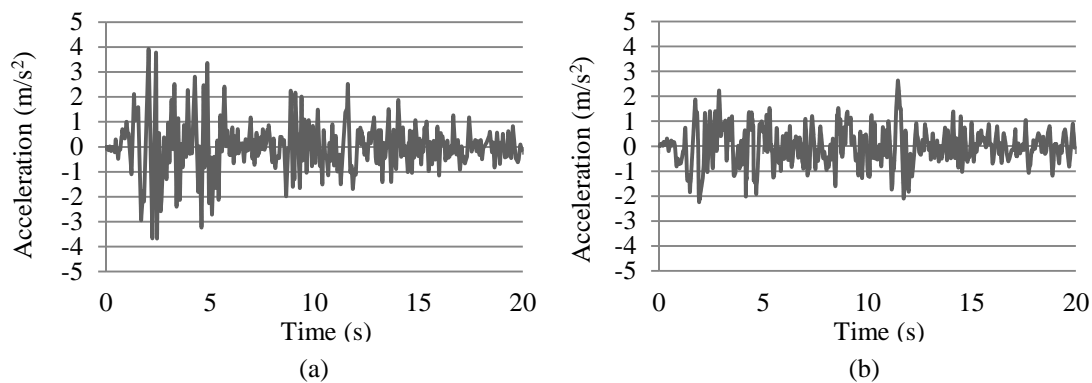


Figure 5.8: Horizontal components of El-Centro earthquake: (a) N-S, (b) E-W

For the 2D analysis, the same division is employed separately for the  $X$  and  $Y$  directions of the tank models. Note that, for each rectangular tank, two different 2D models are prepared. For the cross sections parallel to the shorter and longer side walls, adopted for analysis in  $X$  and  $Y$  directions, respectively.

For the 3D models, the sloshing heights are calculated at the free surface of the water at the middle cross section of the walls in  $X$  and  $Y$  directions and at the corner of the tank, which are called points  $A$ ,  $B$  and  $C$ , respectively. For the 2D models, the critical point at the free water surface interfacing with the wet surface of the wall is named point  $A$  when the analysis is conducted on

the cross section parallel to the short side wall. Likewise, the point under investigation is named point *B* when the E-W component of the ground motion is applied parallel to the long side wall. Note that 2D models are unable to predict sloshing height at the corner of the rectangular tanks.

### 5.4.1 Effect of Three-Dimensional Geometry on the Sloshing Height

It should be noted that, in cases where the length to width ratio of the rectangular container is quite large, as used in current practice, a 2D model based on the cross-section parallel to the short side wall may be used to determine the sloshing response of the container for the ground motion acting parallel to the cross section. On the other hand, 3D modelling of the tank represents a more realistic simulation of the tank behaviour and predicts higher values for the wave heights at the middle of the short and long side walls in comparison with 2D models. As follows, the differences between calculated sloshing heights for 2D and 3D models as well as the effect of factors such as tank plan dimensions and water level are discussed in this section. Values of sloshing heights calculated using FEM are summarized in Tables 5.8 and 5.9, for the 3D and 2D tank models, respectively.

Table 5.8: Maximum sloshing height of 3D models conducted by FEM

Maximum Sloshing height (mm) - (Group 1)											
Point	A	B	C		A	B	C		A	B	C
SX20Y40	673	475	1067	SX20Y60	661	524	620	SX20Y80	662	468	878
MX20Y40	518	679	953	MX20Y60	521	576	705	MX20Y80	520	573	788
TX20Y40	539	750	1007	TX20Y60	564	639	735	TX20Y80	566	636	741
Maximum Sloshing height (mm) - (Group 2)											
Point	A	B	C		A	B	C		A	B	C
SX30Y40	654	480	696	SX30Y60	653	532	863	SX30Y80	652	473	517
MX30Y40	774	682	1071	MX30Y60	783	583	860	MX30Y80	772	581	622
TX30Y40	894	757	1355	TX30Y60	904	659	965	TX30Y80	900	658	760
Maximum Sloshing height (mm) - (Group 3)											
Point	A	B	C		A	B	C		A	B	C
SX40Y40	383	479	668	SX40Y60	385	535	583	SX40Y80	384	474	563
MX40Y40	459	683	927	MX40Y60	500	598	830	MX40Y80	518	595	687
TX40Y40	744	750	878	TX40Y60	675	741	817	TX40Y80	667	651	832

Table 5.9: Maximum sloshing height of 2D models conducted by FEM

Maximum Sloshing height (mm) - (Group 1)								
Point	A	B		A	B		A	B
SX20Y40	627	478	SX20Y60	627	525	SX20Y80	627	467
MX20Y40	522	676	MX20Y60	522	592	MX20Y80	522	583
TX20Y40	532	726	TX20Y60	532	683	TX20Y80	532	678
Maximum Sloshing height (mm) - (Group 2)								
Point	A	B		A	B		A	B
SX30Y40	498	477	SX30Y60	498	526	SX30Y80	498	467
MX30Y40	770	676	MX30Y60	770	592	MX30Y80	770	583
TX30Y40	846	726	TX30Y60	846	683	TX30Y80	846	678
Maximum Sloshing height (mm) - (Group 3)								
Point	A	B		A	B		A	B
SX40Y40	335	477	SX40Y60	335	526	SX40Y80	335	467
MX40Y40	510	676	MX40Y60	510	592	MX40Y80	510	583
TX40Y40	608	726	TX40Y60	608	683	TX40Y80	608	678

In this study, according to Tables 5.8 and 5.9, it can be observed that in both 2D and 3D tank models, for the tanks with the same plan dimensions, the peak sloshing heights in both directions increase with water level. Basically, when the water level increases in the tank, the period of sloshing mode decreases and becomes closer to that of the external excitation; therefore, results in higher sloshing height. It is observed that the sloshing heights are more profound in tall tank models in comparison with medium and shallow tank models; although, it should be noted that the normalized sloshing height against the water depth is more profound for the shallow tank models in comparison with the tank models with the same plan dimensions and greater water level.

Moreover, according to Tables 5.8 and 5.9, respectively for the sloshing height of 3D and 2D tank models, it is observed that in shallow tanks, the peak sloshing height at the middle cross section of the wall parallel to  $X$  direction decreases when the length of the wall increases. Same trend is observed for the sloshing height at the middle cross section of the wall parallel to  $Y$  direction. Similarly, for medium height and tall height tank models, sloshing decreases as the length of the wall increases. Because, as are shown in Tables 5.2, 5.2 and 5.7, the period of the sloshing mode increases when the length of the walls increases; and as a result, the sloshing height decreases. It

should be noted that when the natural frequency of the tank is higher, its value becomes closer to the frequency of the ground excitation; and as a result, the sloshing height increases.

To describe the effect of the tank plan dimensions on the sloshing height, the peak sloshing heights are presented for three cases of tall tank models. All of them have water depth of  $11.0\text{m}$  and the length of walls parallel to  $X$  direction is  $40.0\text{m}$ . These tanks are referred to as TX40Y40, TX40Y60 and TX40Y80, with the corresponding lengths of the walls parallel to  $Y$  direction equal to  $40.0$ ,  $60.0$  and  $80.0\text{m}$ , respectively. For case TX40Y40, the time histories of sloshing heights for both 2D and 3D models are shown in Figure 5.9. For the 3D model, the peak wave height at the middle cross section of the long side wall, point A, is  $744\text{mm}$ . This value is  $22\%$  higher than the value conducted by the 2D model ( $608\text{mm}$ ). If  $B$  and  $L$ , respectively, represent the length of the wall perpendicular and the one parallel to the direction under investigation, for this case,  $B/L$  ratio equals to  $1.0$ .

For case TX40Y60, time histories of slosh heights of both 3D and 2D models are shown in Figure 5.10. Note that, the  $B/L$  ratio for case TX40Y60 is  $1.5$ . For the 3D model of tank TX40Y60, the peak wave amplitude at point A is  $675\text{mm}$ , similarly, it is  $11\%$  higher than that of 2D model. Similarly, as is demonstrated in Figure 5.11, for the 3D model of case TX40Y80, the sloshing height at point A is  $666\text{mm}$  and is  $10\%$  higher than the  $608\text{mm}$  slosh height obtained using the 2D model. The  $B/L$  ratio for case TX40Y80 is  $2.0$ .

It can be observed that the three-dimensional geometry has a significant effect on the sloshing characteristics. The amplification of sloshing response of the 3D model in comparison with 2D response is more significant when  $B/L$  ratio is smaller.

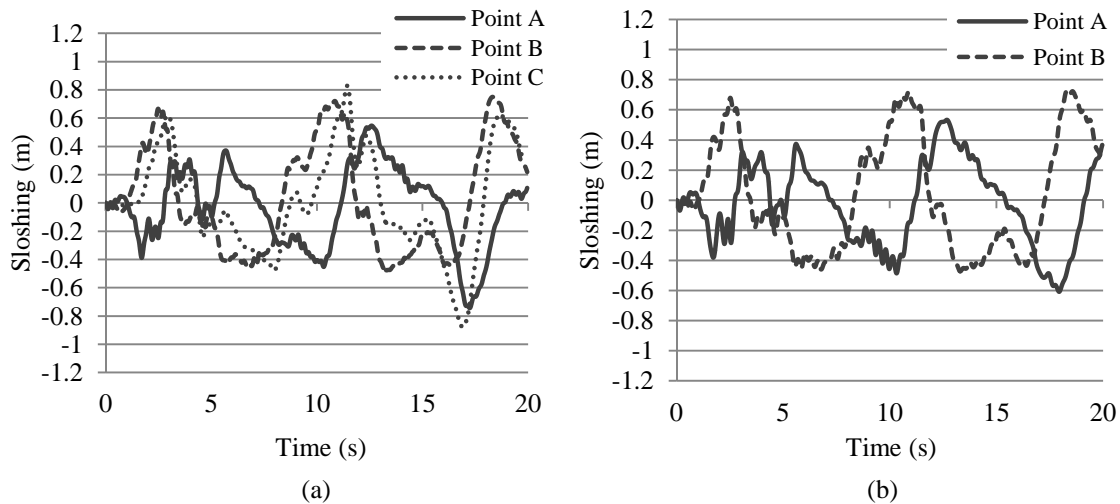


Figure 5.9: Time history of sloshing of TX40Y40: (a) 3D model, (b) 2D model

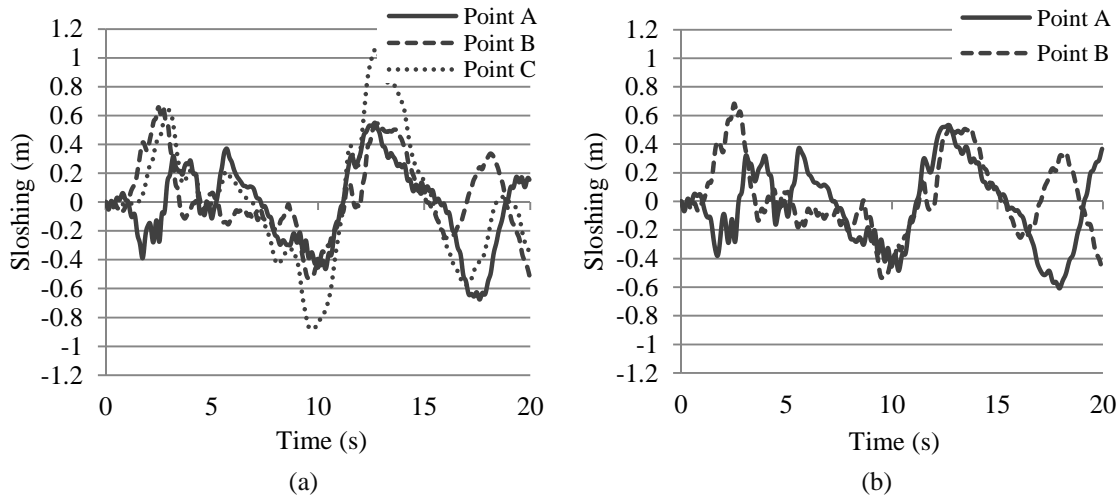


Figure 5.10: Time history of sloshing of TX40Y60: (a) 3D model, (b) 2D model

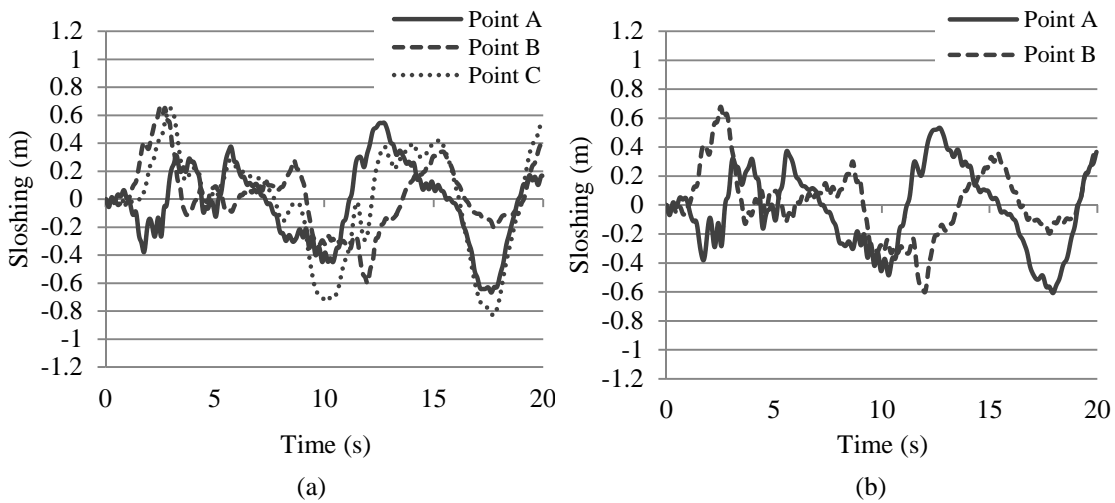


Figure 5.11: Time history of sloshing of TX40Y80: (a) 3D model, (b) 2D model

The relative increase of sloshing height in 3D model in comparison with 2D model seems to be very sensitive to water level as well. To demonstrate this relation, time histories of sloshing heights are also presented for three other tank size configurations. These tanks have plan dimension of  $30m \times 60m$ . These tanks are referred to as SX30Y60, MX30Y60 and TX30Y60, with water depth of 5.5, 8.0 and 11.0m, respectively.

Figure 5.12 shows the time history of sloshing height of case SX30Y60 for both 3D and 2D models. The peak sloshing height at middle cross section of the long side wall, point A, is 653 mm for the 3D model and is 31% higher than the 498 mm sloshing height at point A for the 2D model.

It should be noted that, for this case,  $L/H_L$  and  $B/L$  ratios are 5.45 and 2.0, respectively. Sloshing height at point  $B$  is 532 mm for the 3D model and is 1% higher than that of the 2D model. It should be noted that when the sloshing height is being calculated at point  $B$ , the E-W component of the ground motion is applied parallel to  $Y$  direction, and the 2D model is formed based on the cross section parallel to the  $Y$  direction. In this case,  $L/H_L$  and  $B/L$  ratios are 10.91 and 0.5, respectively.

Figure 5.13 shows the variation of the slosh height with time for tank model MX30Y60. It is observed that the maximum sloshing height at point  $A$  is 783 mm for the 3D models. This value is 2% higher the sloshing height of 770 mm for the 2D model. In this case, the difference is insignificant. It should be note that, for this medium height tank,  $L/H_L$  and  $B/L$  ratios are 3.75 and 2.0, respectively.

The time history of sloshing height, for both 3D and 2D models, are presented in Figure 5.14 for the tall tank, TX30Y60. As is shown, the peak sloshing height at point  $A$  for the 3D model is 904 mm and is 6% higher than the 846 mm sloshing height obtained from the 2D model. In this case,  $L/H_L$  and  $B/L$  ratios are 2.73 and 2.0, respectively.

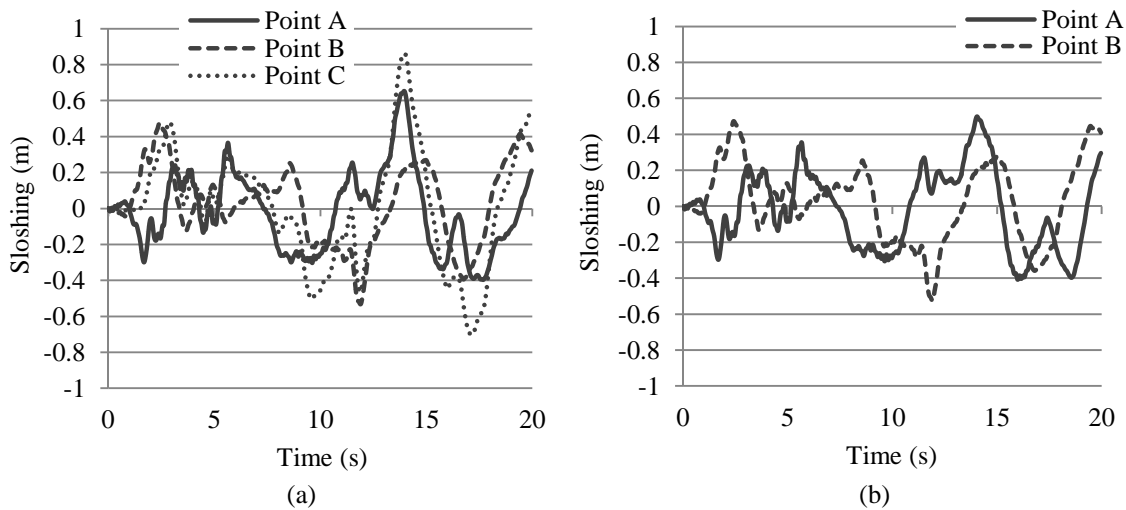


Figure 5.12: Time history of sloshing of SX30Y60: (a) 3D model, (b) 2D model

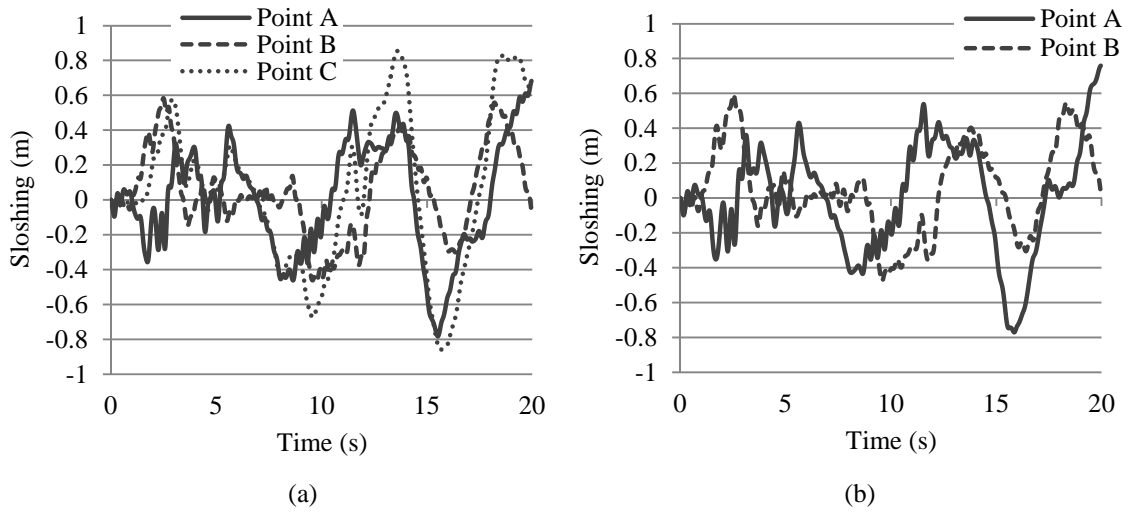


Figure 5.13: Time history of sloshing of MX30Y60: (a) 3D model, (b) 2D model

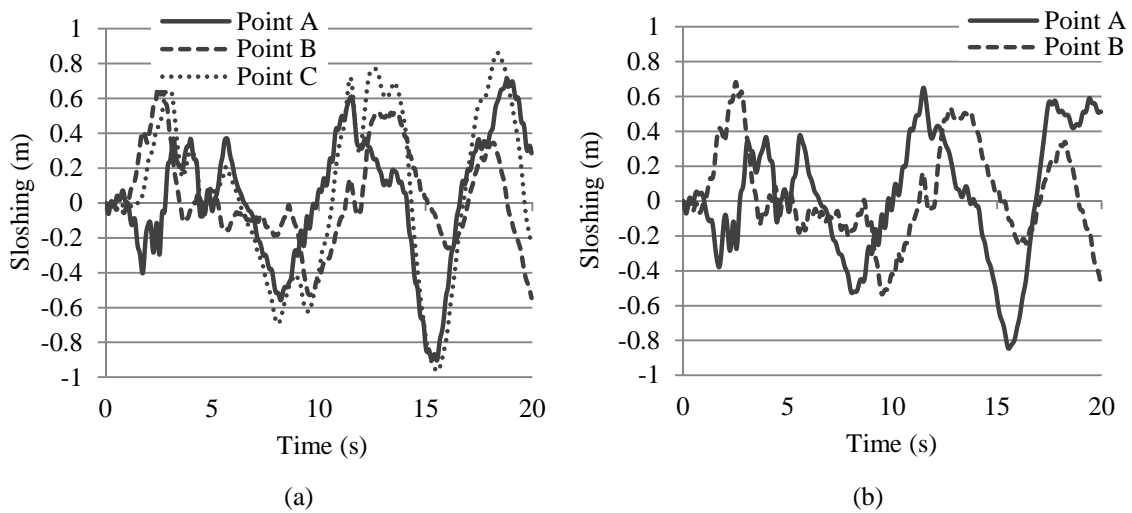


Figure 5.14: Time history of sloshing of TX30Y60: (a) 3D model, (b) 2D model

Summarizing the results, the sloshing height is compared for all of tank configurations summarized in Table 5.1. It is observed that the effect of the walls parallel to the direction of excitation cannot be ignored for the cases with smaller values of  $B/L$  ratios. For these cases, the differences in wave height obtained from 3D and 2D models are more profound. Figure 5.15 shows the ratios of sloshing height in 3D models in comparison with the 2D models, against  $L/H_L$  ratio. It can be concluded that, in general, 3D models estimate slightly higher values for the sloshing height in comparison with the 2D models. The maximum difference between the results of 3D and 2D tank models are 7%, 31% and 22% for groups 1, 2 and 3, respectively.

As discussed previously and according to Figure 5.15, it can be concluded that the sloshing response is sensitive to  $L/H_L$  ratio. However, as this ratio reaches the value of 10, the response of the 3D models becomes very close to that of 2D models. A similar trend to sloshing response was reported by Kim et al. (1998). As discussed previously, for the tanks with ratio of  $B/L$  greater than 2.0, the response of 2D and 3D models approaches to similar values. This fact may justify the use of 2D models for the tanks that have  $B/L$  and  $L/H_L$  ratios greater than 2.0 and 10, respectively.

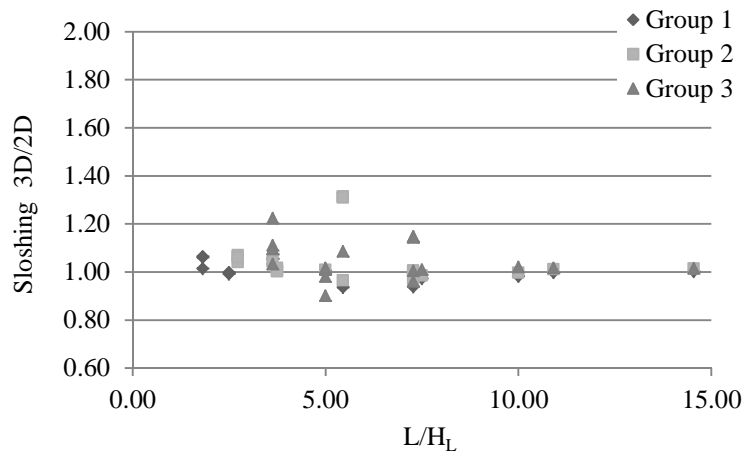


Figure 5.15: Sloshing height comparison between 3D and 2D models against  $L/H_L$

In order to consider the effect of three-dimensional geometry, the amplification coefficient  $\alpha$ , may be applied to the sloshing height obtained from 2D models:

- For  $B/L \geq 2.0$  and  $L/H_L \geq 10.0$ ,  $\alpha = 1.0$
- For  $B/L \geq 2.0$  and  $L/H_L < 10.0$ ,  $\alpha = 1.2$
- For  $B/L < 2.0$  and  $L/H_L < 10.0$ ,  $\alpha = 1.3$

### 5.4.2 Sloshing at Tank Corners

Wave interference is a phenomenon that occurs when two waves meet while travelling along the same medium. The interference of waves causes the medium to take on a shape that results from the net effect of the two individual waves upon the particles of the medium. Wave interference can be constructive or destructive in nature. Constructive interference occurs at any location along the medium where the two interfering waves have a displacement in the same direction.

Destructive interference occurs at any location along the medium where the two interfering waves have displacement in the opposite directions. Figure 5.16 displays the free water surface profile of the maximum sloshing for a typical shallow tank model. Due to the constructive interaction of the waves in  $X$  and  $Y$  directions, the peak height is at the corner of the tank. Note that, in current practice, two-dimensional models are used to calculate the sloshing height of the seismically excited tank; however, 2D models are unable to predict the slosh height at the corner of the tank, which is significantly higher than other locations.

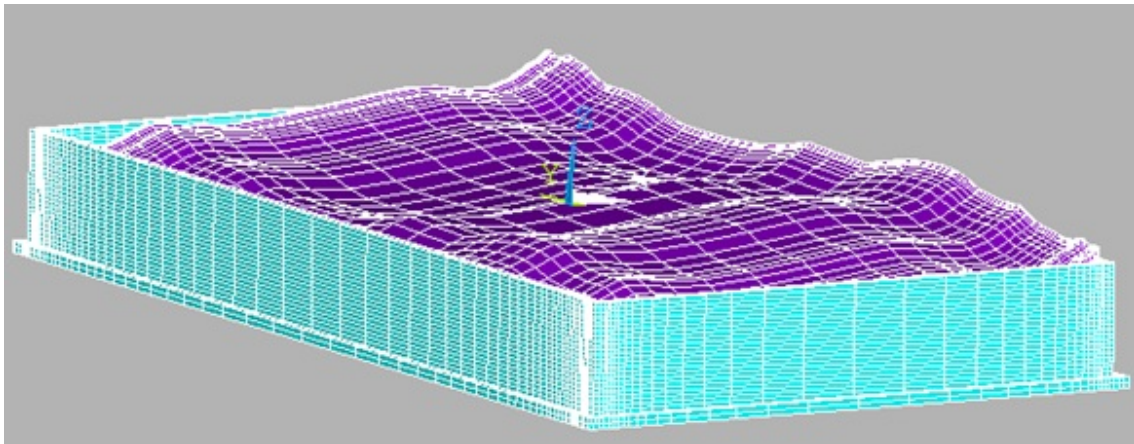


Figure 5.16: Free water surface when the maximum sloshing occurs for a typical shallow tank

In this section, two different investigations are made on the 3D tank models: First, the maximum sloshing at the corner of the tanks are compared with the maximum sloshing heights at points  $A$  and  $B$ . Second, for each case under discussion, at the time that the maximum sloshing occurs at point  $C$ , the amplifications of the wave heights at the corners relative to those at points  $A$  and  $B$  are calculated. The purpose of the first investigation is to find a practical method that is applicable for design application, and the second investigations are made to determine the formation of constructive and destructive wave interference.

The sloshing height at the corner of the tank is compared to the sloshing height at the middle cross section of the walls, in both  $X$  and  $Y$  directions. Three different tank configurations having plan dimensions of  $20m \times 40m$  are discussed. The depth of water for these tanks are  $5.5m$ ,  $8.0m$  and  $11.0m$  and are referred to as SX20Y40 (shallow), MX20Y40 (medium) and TX20Y40 (tall), respectively.

Figure 5.17 shows the time history of the sloshing behaviour of the 3D model for tank SX20Y40. It can be observed that the maximum sloshing height of the free surface water in the direction

perpendicular to longer dimension (at point *A*) is  $673\text{ mm}$ . The value of the maximum sloshing in the direction parallel to the long side wall (at point *B*) is  $475\text{ mm}$ . It is observed that due to applying both longitudinal and transverse component of the earthquake, interaction of the waves initiates a major movement of the surface water at the corner of the tank. The water surface at the corner of the tank shifts about  $1067\text{ mm}$ . This value is  $58\%$  higher than the peak displacement at point *A*. The maximum sloshing height at the corner of the shallow tank is  $124\%$  higher than that at point *B*. The maximum sloshing at points *A*, *B* and *C* respectively happen at  $17.7\text{ sec}$ ,  $2.44\text{ sec}$  and  $11.46\text{ sec}$  of the analysis, and phase differences are observed.

It should be noted that, at  $11.46\text{ s}$  of the analysis, when the sloshing height reaches its peak value of  $1067\text{ mm}$ , the sloshing height at point *A* is higher than the one at point *B* and equals to  $623\text{ mm}$ . It is observed that at the same time, sloshing height at the corner of this shallow tank model is  $71\%$  higher than that at point *A*. It should be noted that for 3D model of case SX20Y40, the natural frequency of first sloshing mode in *X* direction is  $0.165\text{ Hz}$  and in *Y* direction is  $0.089\text{ Hz}$ . The difference between the natural frequencies in *X* and *Y* direction is  $49\%$ . As a result, the waves in *X* and *Y* directions form in different phases.

Figure 5.18 shows the time history of sloshing height for the case MX20Y40. The 3D model estimates the maximum sloshing height of  $518\text{ mm}$  at point *A* and  $679\text{ mm}$  at point *B*. The absolute maximum wave shift of  $953\text{ mm}$  at the corner of the medium tank occurs at  $11.44\text{ s}$ . This value is  $84\%$  more than the peak sloshing height at middle cross section of the long wall at point *A*. In addition, it is  $41\%$  more than the peak displacement at the middle cross section of the short wall at point *B*. For MX20Y40, the maximum sloshing heights at points *A* and *B* respectively happens at  $13.28\text{ sec}$  and  $16.7\text{ sec}$ .

On the other hand, at the time that the maximum sloshing occurs at the corner of the tank, the sloshing height at point *B* is higher than that at point *A* and is  $637\text{ mm}$ . At  $11.44\text{ s}$  of analysis, the sloshing height at the corner of the tank is  $49\%$  higher than the sloshing height at point *B*. It should be noted that the natural frequencies of sloshing mode in *X* and *Y* directions are  $0.182\text{ Hz}$  and  $0.104\text{ Hz}$ . It should be noticed that the difference between natural frequencies in *X* and *Y* directions is  $42\%$  for tank model MX20Y40.

As shown in Figure 5.19, for the 3D model of the tall tank model (TX20Y40), the free water surface at the middle cross section of the long side wall (Point *A*) shifts up to  $539\text{ mm}$ . The maximum slosh height at point *B* is  $750\text{ mm}$ . For this tall tank model, wave height at the corner of the tank reaches the value of  $1007\text{ mm}$ . This value is  $86\%$  more than peak slosh height at point *A* and  $34\%$  more than that at point *B*. The peak sloshing heights at points *A*, *B* and *C* respectively

happen at 9.12 sec, 18.28 sec and at 18.2 s of excitation.

In addition to the peak sloshing height at 18.2 s, there is another peak height happening at 8.12 s of analysis and is 814 mm. At the same time, the sloshing height at point A is 539 mm. It is observed that, for this case, the sloshing height at the corner of the tank is 51% higher than that at point A. It should be noted that the natural frequencies of sloshing in X and Y directions are 0.191 Hz and 0.117 Hz, respectively. The difference between those frequencies is 38%.

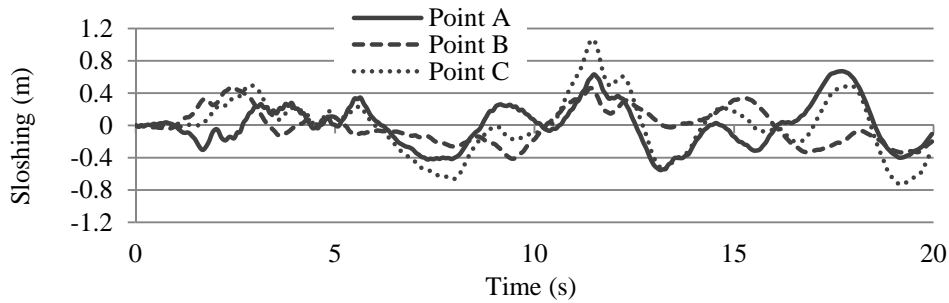


Figure 5.17: Time history of sloshing height for case SX20Y40

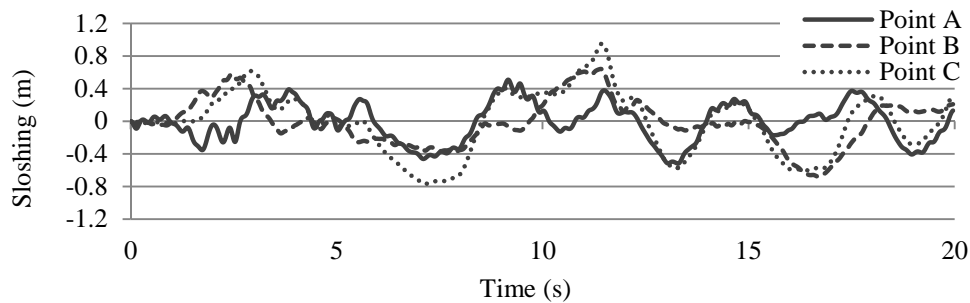


Figure 5.18: Time history of sloshing height for case MX20Y40

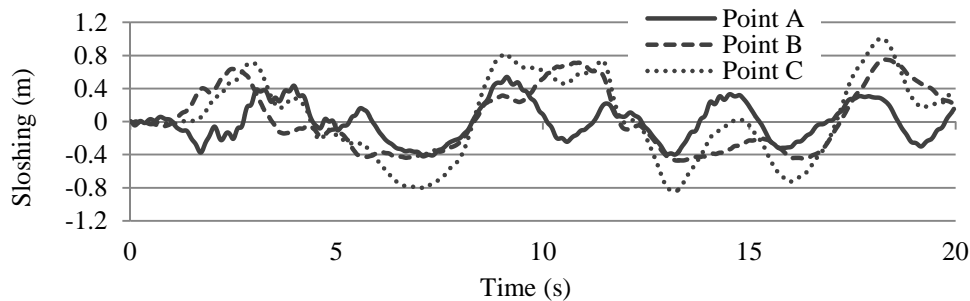


Figure 5.19: Time history of sloshing height for case TX20Y40

In this study, it is observed that for the tanks of the same plan dimensions, the amplification of slosh wave at the corner of the tank relative to those at the middle of the walls is more profound for the tanks with greater water depth. In tall and medium tanks, by comparing the differences between sloshing frequencies in  $X$  and  $Y$  directions, it is observed that the difference is lower for the tall tank; and as a result, the possibility of constructive waves interference at the corner of the tank may be higher for the taller tank.

On the other hand, for the shallow tanks, the difference between sloshing frequencies in  $X$  and  $Y$  direction is higher in comparison with medium and tall height tank. However, as shallow tanks have lower natural frequencies for the sloshing modes in comparison with the medium and tall height tank, it is possible that the waves in  $X$  and  $Y$  directions both are forming with greater time periods between peaks. As a result, the possibility of constructive waves interference at the corner of the tanks may be higher for shallow tanks, in comparison with medium and tall tanks.

In addition to water level, tank plan dimension has a significant effect on the sloshing behaviour of rectangular tanks. To investigate this effect, time history responses of sloshing height are presented for three shallow tanks having different plan dimensions. Figure 5.20 shows the sloshing height for a three-dimensional shallow tank having plan dimension of  $40\text{ m} \times 40\text{ m}$  which is named SX40Y40. It may be noticed that  $B/L$  ratio is 1.0. For this square tank, the maximum sloshing heights at points  $A$  and  $B$  are  $383\text{ mm}$  and  $479\text{ mm}$ , respectively. The maximum responses occur at  $10.38\text{ sec}$  and  $2.44\text{ sec}$  for  $X$  and  $Y$  directions, respectively. On the other hand, the peak sloshing height at the corner of this square tank is  $668\text{ mm}$ . It should be noted that maximum sloshing height at the corner of this tank model is 75% higher than that at point  $A$ , and is 39% more than the maximum sloshing height at point  $B$ .

It should be noted that, for this square shallow tank, the natural frequencies of sloshing modes are identical in  $X$  and  $Y$  direction. As a result, the waves perpendicular to each other interact with similar phase at the corner of the tank. It is observed that at  $15.38\text{ s}$  of the excitation, at the time the peak sloshing height occurs at the corner of the tank, the sloshing height at point  $A$  is  $336\text{ mm}$ . At that time, the sloshing height is increased by 98% at the corner of the tank in comparison with the middle of the wall.

The sloshing height is also calculated at points  $A$ ,  $B$  and  $C$  for case SX40Y60. In this case, the tank has plan dimension of  $40\text{ m} \times 60\text{ m}$  and the  $B/L$  ratio for this tank is 1.5. Time history of sloshing is presented in Figure 5.21. It is observed that the maximum sloshing height at points  $A$  and  $B$  are  $385\text{ mm}$  and  $535\text{ mm}$ , respectively. The maximum sloshing height at the corner of the tank is  $583\text{ mm}$ , which is 52% and 9% more than the maximum sloshing height at points  $A$  and

$B$ , respectively. The maximum sloshing heights at points  $A$ ,  $B$  and  $C$  occur at 10.38, 11.9 and 10.49 *sec*, respectively.

For the 3D model of SX40Y60, at 10.49 *s* of the analysis, when the peak sloshing happens at the corner of the tank, the sloshing heights at points  $A$  and  $B$  are 360 *mm* and 222 *mm*, respectively. The sloshing height at the corner at the same time is 61% more than the one at point  $A$ . It should be noted that the natural frequencies of sloshing in  $X$  and  $Y$  direction for this tank differ by 32%. As a result, in comparison with the square tank, the possibility of formation of the wave of the water in those directions is less to be in a similar phase.

Figure 5.22 shows the time history of sloshing at points  $A$ ,  $B$  and  $C$  for the shallow tank SX40Y80. Length of the tank walls parallel to  $X$  and  $Y$  directions are 40 and 80 *m*, respectively. The  $B/L$  ratio for this tank is 2.0. It is observed that the maximum sloshing height at point  $A$  is 384 *mm*. The sloshing height at point  $B$  is 474 *mm*. For points  $A$  and  $B$ , the maximum sloshing height is at 10.38 *sec* and 2.44 *sec*, respectively. On the other hand, the maximum sloshing height at the corner of the tank is 563 *mm* and happens at 10.46 *sec*, which is 47% and 19% higher than the ones at points  $A$  and  $B$ , respectively.

For SX40Y80, the frequencies of sloshing are 0.089 and 0.046 *Hz* in  $X$  and  $Y$  directions, respectively; and, the difference is 48%. As a result, at 18.2 *s* of the excitation, the sloshing height is 181 *mm* in  $X$  direction, while the sloshing height in  $Y$  direction is 360 *mm*. Therefore, at 18.2 *s* of the excitation, the sloshing height at the corner of the tank reaches a maximum of 474 *mm* and is 58% higher than that at point  $B$ .

It is observed that the amplification of wave height at the corner of the tank as compared to the middle of the wall is profoundly related to the tank plan dimensions. If  $B$  and  $L$ , symbolize the length of the tank wall perpendicular and parallel to the direction of the ground motion, respectively; the higher amplifications at the corners relative to the middle of the walls happen for the case with a smaller value of  $B/L$  ratio. Because when the  $B/L$  ratio is relatively small, the natural sloshing frequencies of the tank in  $X$  and  $Y$  directions are closer values; and as a result, there is a higher chance that the waves in  $X$  and  $Y$  directions reach to a higher level at closer time, and cause constructive interference. As a result, when the waves interact at the corner of the tank, there is a profound increase in the wave height. As was mentioned, the peak wave height at the corner of a square tank, with  $B/L$  ratio of 1.0, is increased by 75% in comparison with the maximum sloshing height at the middle of the wall. It should be noticed that, for the square tank, the peak sloshing happens at the corner of the tank, and at the exact time, this value is 98% higher than the sloshing height at the middle of the wall. This increase happens for the cases that

are subjected to different excitation in  $X$  and  $Y$  directions. It should be noted that cases that are subjected to exactly the same earthquake in both  $X$  and  $Y$  directions will be covered in section 5.4.3.

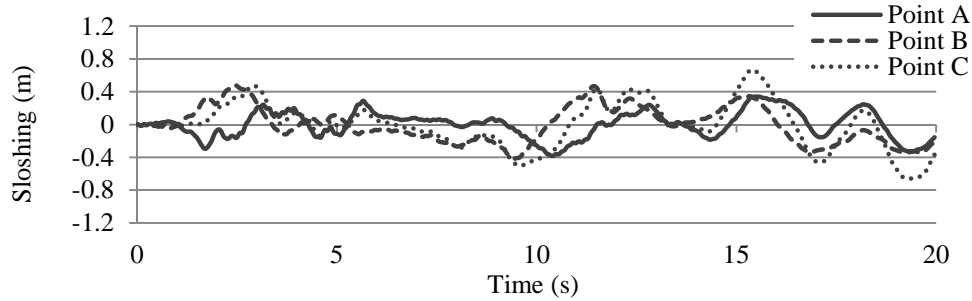


Figure 5.20: Time history of sloshing height for SX40Y40

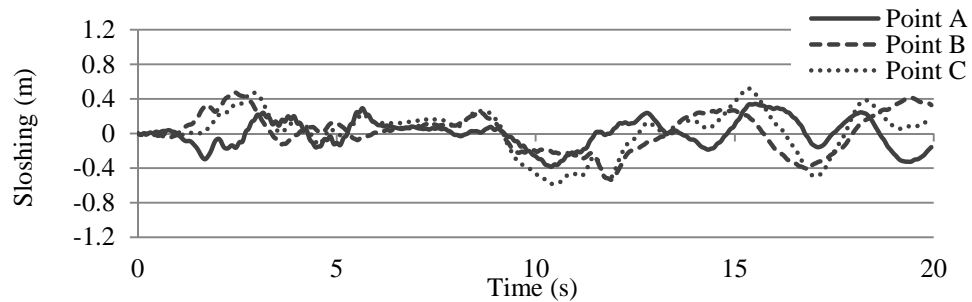


Figure 5.21: Time history of sloshing height for SX40Y60

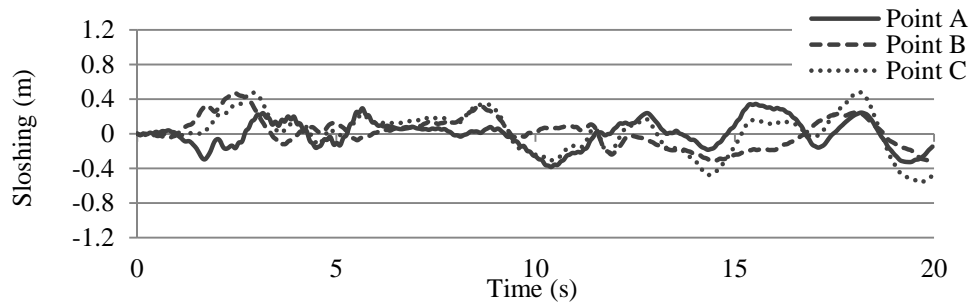


Figure 5.22: Time history of sloshing height for case SX40Y80

From the results of the sloshing heights of the rectangular water tank models subjected to the El-Centro earthquake, it is observed that in order to calculate the peak sloshing height at the corner of a rectangular tank, amplification coefficient  $\beta$  may be applied to the maximum sloshing height at the middle of the tank wall. Note that the coefficient,  $\beta$ , shall be applied to the greater value of the sloshing heights in  $X$  and  $Y$  directions:

- For  $B/L \geq 2.0$ ,  $\beta = 1.4$
- For  $B/L < 2.0$ ,  $\beta = 1.6$

### 5.4.3 Effect of Earthquake Frequency Content

As previously mentioned, the sloshing behavior of the water tank is profoundly effected by factors such as tank plan dimensions and water level, as well as the frequency content and the peak acceleration of the earthquake. The effects of earthquake frequency content on the sloshing characteristic of the 3D rectangular tank are discussed in this section.

In this section, three rectangular tanks, are subjected to three different ground motion records. The sloshing heights at point *A* are calculated for SX30Y80, MX30Y80 and TX30Y80. Note that the longitudinal components recorded for 1994 Northridge, 1940 El-Centro and 1957 San-Francisco earthquakes are used as excitations of the tank-liquid system. The components are scaled in such a way that the peak ground acceleration in the longitudinal direction reaches 0.4g, as shown in Figure 5.23. The acceleration response spectrum are also shown in Figure 5.24.

A good indicator of the frequency content of the ground motion is the ratio of peak ground acceleration (PGA), which is expressed in units of *g*, to peak ground velocity (PGV), expressed in units of (*m/s*). Earthquake records may be classified according to the frequency content ratio into three categories; high *PGA/PGV* ratio when  $PGA/PGV > 1.2$ , intermediate *PGA/PGV* ratio when  $1.2 > PGA/PGV > 0.8$ , and low *PGA/PGV* ratio when  $PGA/PGV < 0.8$ . The Northridge record has low frequency content; the El-Centro has intermediate frequency contents and the San-Francisco record has the high frequency content. It should be noted that the predominant period for Northridge record is 0.708sec and for the El-Centro and San-Francisco earthquakes are 0.50sec and 0.22sec, respectively.

In addition, the power spectral density (PSD) functions for the three ground motions are shown in Figure 5.25. Power spectral density function (PSD) shows the strength of the variations (energy) as a function of frequency. The centre of the masses of the PSD functions are located at 2.04Hz, 3.20Hz and 6.21Hz for Northridge, El-Centro and San-Francisco records, respectively. These values correspond with natural periods of 0.48sec, 0.31sec and 0.16sec, respectively. According to PSD concept, the significant amount of energy of the ground motion is concentrated at the centre of the mass of PSD function. As a result, the maximum response of the structure is expected under the ground motion record which has the nearest centre of mass location to the fundamental

natural period or frequency of the structure.

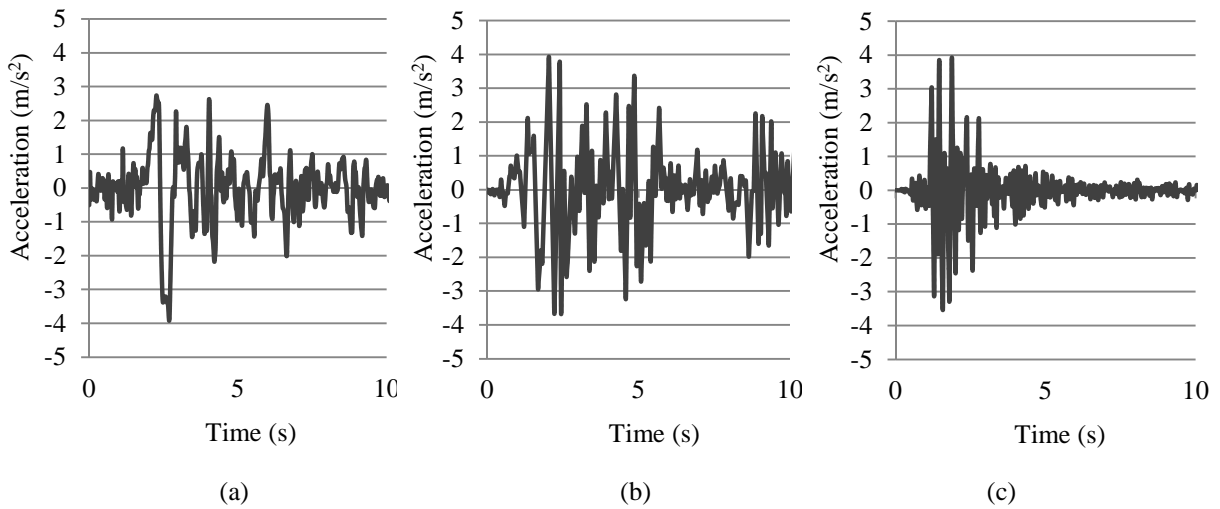


Figure 5.23: Scaled longitudinal components of earthquake records: (a) 1994 Northridge (b) 1940 El-Centro (c) 1957 San-Francisco

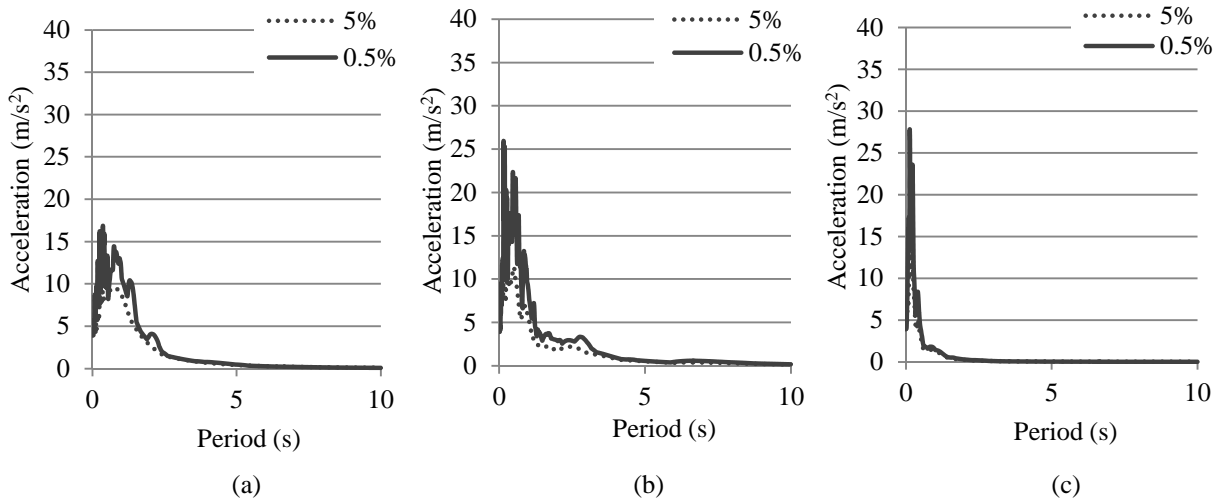


Figure 5.24: Acceleration response spectrum of earthquake records: (a) 1994 Northridge (b) 1940 El-Centro (c) 1957 San-Francisco

Figure 5.26 represents the comparison of the sloshing height conducted for three tanks that are subjected to three earthquake records that have the same peak acceleration but different frequency content. For the first ten seconds of the record, the sloshing heights are calculated at point A and compared for SX30Y80, MX30Y80 and TX30Y80. It is observed that the frequency content of

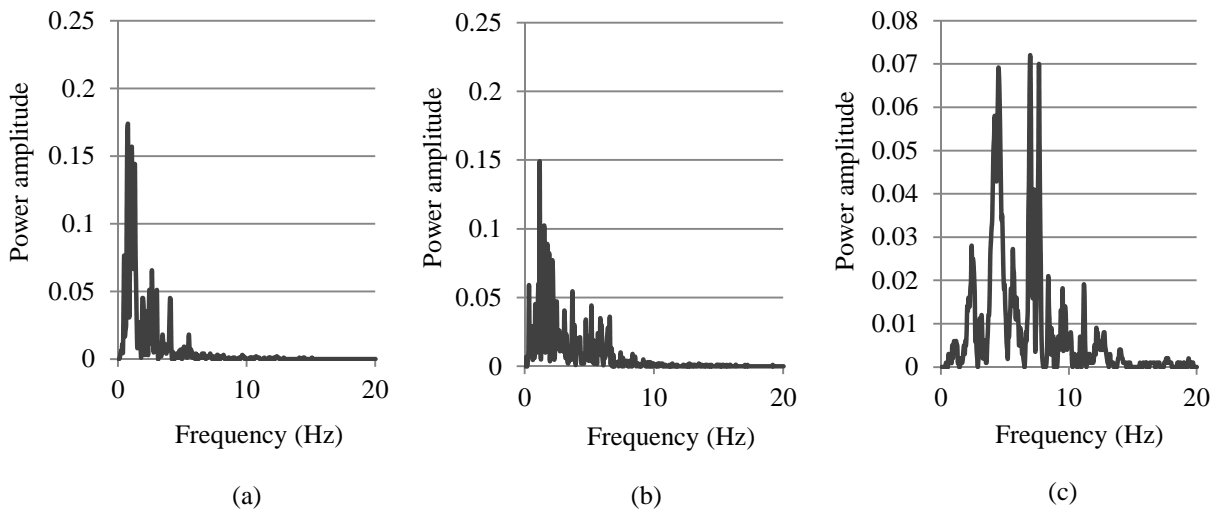


Figure 5.25: PSD function: (a) Northridge (b) El-Centro (c) San-Francisco

the earthquake has a significant effect on the sloshing height. As is shown, although the three records have the same peak acceleration, the sloshing height is higher when the centre of the mass of PSD functions of the record is at lower frequency.

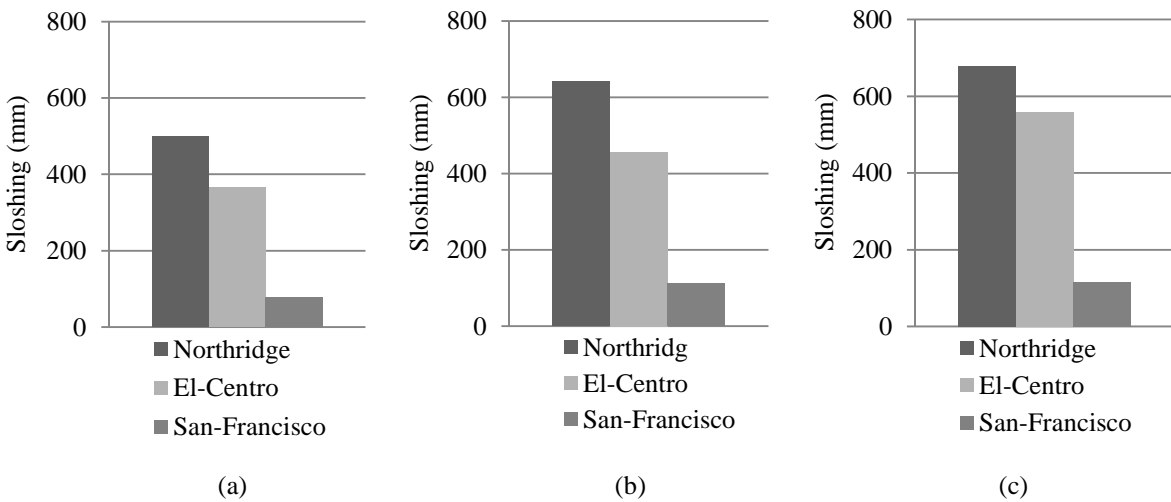


Figure 5.26: Relative sloshing height: (a) SX30Y80, (b) MX30Y80, (c) TX30Y80

#### 5.4.4 Effect of Earthquake Frequency Content on Wave Interference

In section 5.4.2, it was observed that, for some tanks, the maximum sloshing heights at the corner of the 3D tanks are smaller than the peak sloshing height at the middle of the wall. For instance; in the 3D models of cases SX30Y80, MX30Y80 and TX30Y80. The time histories of sloshing are presented for these tank models, in Figures 5.27, 5.28 and 5.29, respectively. It should be noted that the N-S component of the excitation is applied in  $X$  direction, and the E-W component is applied in  $Y$  direction. As a result, the direction and the peak accelerations are different in  $X$  and  $Y$  directions.

For the 3D model of case SX30Y80, time history of sloshing height is shown in Figure 5.27. It can be observed that the maximum sloshing in  $X$  direction is  $652\text{ mm}$  and happens at  $13.96\text{ sec}$  of the analysis. At that time, the slosh height in  $Y$  direction is negative  $228\text{ mm}$ . As a result, at  $13.96\text{ sec}$  of the analysis, the sloshing height at the corner of the tank is lower relative to that at point  $A$  and is  $424\text{ mm}$ . Clearly, the phase difference between sloshing in  $X$  and  $Y$  directions caused the decrease in the sloshing height at the corner of the tank. On the other hand, the negative peak at the corner of the tank is  $517\text{ mm}$  and happens at  $15.68\text{ sec}$  of the excitation. At the same time, the absolute sloshing height in  $X$  and  $Y$  directions are  $332\text{ mm}$  and  $187\text{ mm}$ , respectively. It is observed that when the maximum sloshing height happens at the corner of the tank, the sloshing height at point  $C$  is  $56\%$  higher than that at point  $A$ .

It should be noted that the El-Centro earthquake is considered as an intermediate frequency earthquake, and the predominant period for this record is  $0.5\text{ sec}$ . When such an earthquake is applied to the tank, especially when the  $B/L$  ratio is high, the chance that wave may cause constructive interference is less. Because, when the  $B/L$  ratio is high, the phase difference between the sloshing in  $X$  and  $Y$  direction may be large.

For the medium tank, MX30Y80, the sloshing height variation with time is presented in Figure 5.28. It can be observed that beside the peak sloshing height at time  $19.96\text{ sec}$ , there is another peak in the sloshing height which happens at  $15.68\text{ sec}$  of the excitation. In that case, the peak negative sloshing height in  $X$  direction is  $767\text{ mm}$  while the sloshing height in  $Y$  direction is positive  $149\text{ mm}$ . Interaction of these waves at the corner of the tank causes slosh height of  $543\text{ mm}$ . Again, phase difference causes a reduction in sloshing height and destructive interference happens. It should be noticed that, at  $2.92\text{ sec}$ , sloshing height at the corner has a relatively higher value and reaches  $581\text{ mm}$ . At the same time, the sloshing height at point  $B$  is  $403\text{ mm}$ . In this case, the sloshing height at the corner is  $44\%$  higher than the one at the middle of the wall.

The time history sloshing response of the tall tank, TX30Y80, is shown in Figure 5.29. It is observed that, at 15.58 sec of the analysis, the sloshing height reaches its peak negative value of 872 mm in  $X$  direction. However, at the same time, the sloshing height in  $Y$  direction has positive value of 297 mm. As a result, the absolute sloshing at the corner of the tank is 545 mm and lower than those at the middle of the wall. Similarly, the phase difference between sloshing in  $X$  and  $Y$  direction causes a decrease in sloshing height. On the other hand, the peak sloshing height at the corner of the tank is 760 mm happening at 19.4 sec. At the same time, the sloshing height in  $X$  and  $Y$  directions are 571 mm and 218 mm, respectively. In this case, the sloshing height at the corner is 33% higher than that at the middle of the wall.

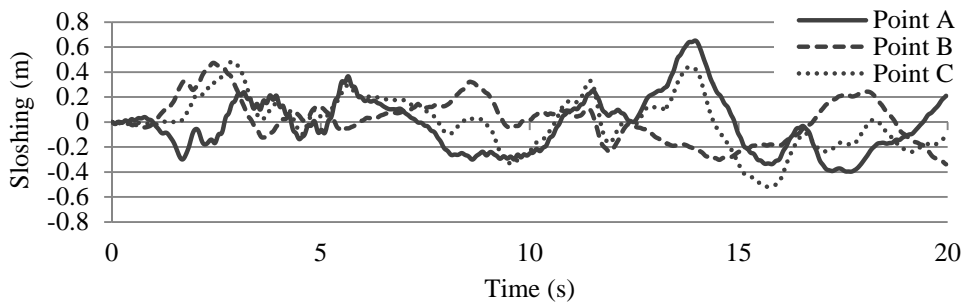


Figure 5.27: Time history of sloshing height of SX30Y80

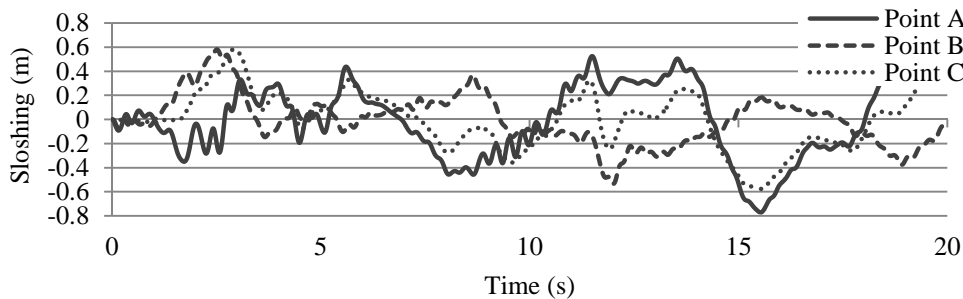


Figure 5.28: Time history of sloshing height of MX30Y80

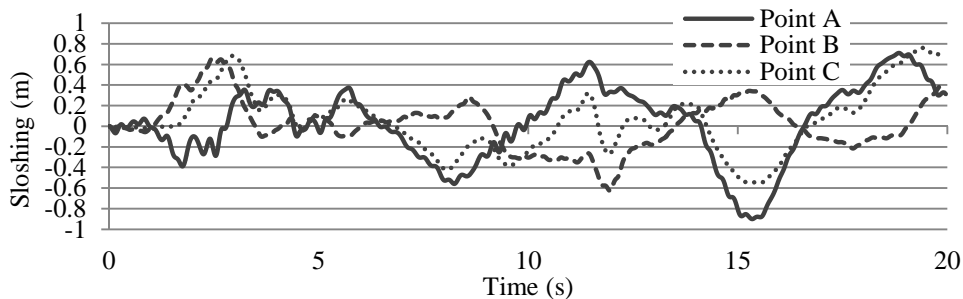


Figure 5.29: Time history of sloshing height of TX30Y80

To investigate the interaction of waves subjected to similar ground motions, 3D tank models are also subjected to similar earthquake in  $X$  and  $Y$  directions. For this purpose, some of the tanks described in Table 5.1, are subjected to the longitudinal components recorded for 1994 Northridge earthquake. The components are scaled in such a way that the peak ground acceleration in the longitudinal directions reach  $0.4g$ , as shown in Figure 5.23(a). It should be noted the peak acceleration is at 2.69 seconds after the start of the excitation, obviously, there is high energy pulse at 2.69 *sec*. This earthquake record is considered as a low frequency content ground motion, and the predominant period for this record is higher than the one for the El-Centro record and equals to 0.708 *sec*. Note that, points  $A$ ,  $B$  and  $C$ , as defined in previous sections, are located at the free water surface at the middle cross section of the walls perpendicular to  $X$  and  $Y$  directions and at the corner of the tank, respectively. Preliminary, analysis was conducted for the first 15 *sec* of the excitation, and it was observed that the peak sloshing happens during the first 5 *sec* of the analysis. Therefore, the results are presented for the first 10 *sec* of the analysis with time intervals of 0.01 *sec*.

Time histories of sloshing are presented for three tanks having plan dimension of  $30m \times 80m$ . Figure 5.30 represents the time history of sloshing height at three critical points, for shallow tank model SX30Y80. It is observed that when the scaled longitudinal components of Northridge earthquake is applied on the tank, both in  $X$  and  $Y$  directions, the sloshing heights at points  $A$  and  $B$  are 501 *mm* and 493 *mm*. The absolute peak sloshing heights at points  $A$  and  $B$  happen, respectively, at 2.51 *sec* and 2.53 *sec* of the analysis. It should be noticed that the peak sloshing height at points  $A$  and  $B$  are happening with a very small phase difference. It is observed that the peak absolute sloshing height at the corner of the tank happens at 2.53 *sec* after the start of analysis and is 979 *mm*. The sloshing height at point  $C$  is 95% and 98% higher than those at points  $A$  and  $B$ , respectively. It is observed that, in this case, constructive interference occurs.

For medium height tank model, MX30Y80, subjected to 1994 Northridge earthquake, time history of sloshing height is presented in Figure 5.31. In this case, the peak negative sloshing heights at points  $A$  and  $B$  are 642 *mm* and 612 *mm* and happen at 2.56 and 2.54 seconds of the excitation, respectively. Similar to the shallow tank model, the peak sloshing height in  $X$  and  $Y$  directions happen with a very small phase difference. On the other hand, the peak negative sloshing height at the corner of medium height tanks happens at 2.55 *sec* after the start of analysis and is 1100 *mm*. The sloshing height at point  $C$  is 71% and 79% higher than those at points  $A$  and  $B$ , respectively.

Figure 5.32 shows the time history of sloshing heights for tall tank model, TX30Y80. For this tank model, the peak sloshing height at point  $A$  is 681 *mm* and happens at 2.55 *s*. At point  $B$ , the

peak sloshing height is 607 mm and happens at 2.54 s. Similarly, in this tank model, the peak slosh heights in  $X$  and  $Y$  directions happen almost at the same time. As a result, water waves interact with each other with their peak sloshing heights and initiate 1187 mm vertical displacement at the corner of the tank at 2.56 s. At the time, the sloshing height at point  $C$  is 75% greater than that at point  $A$ .

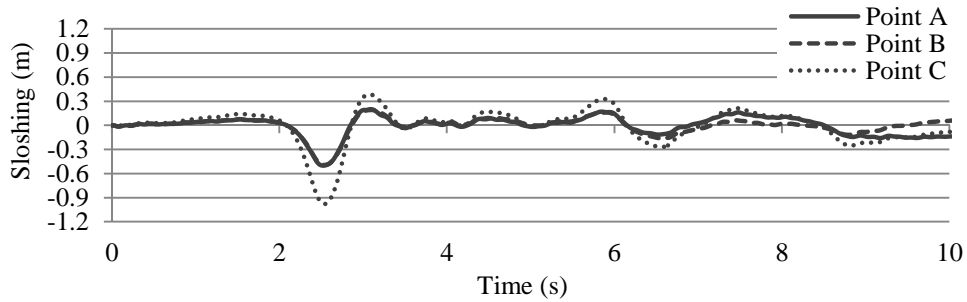


Figure 5.30: Time history of sloshing height of SX30Y80 - Northridge

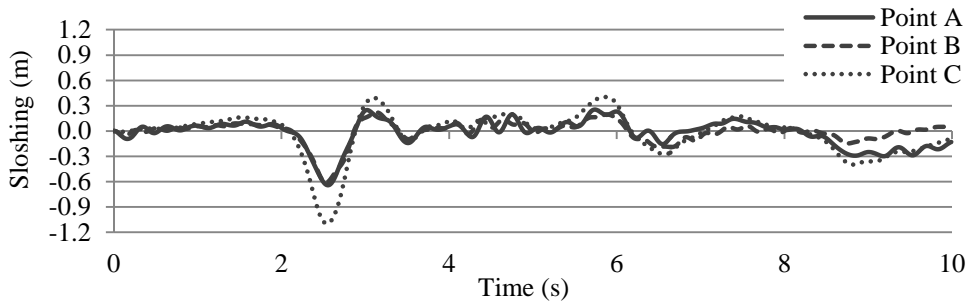


Figure 5.31: Time history of sloshing height of MX30Y80 - Northridge

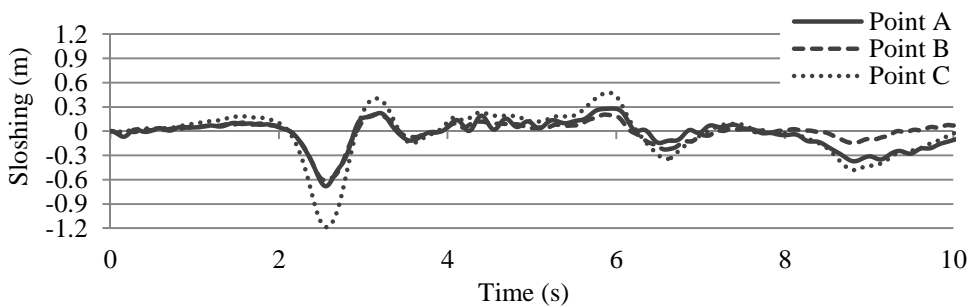


Figure 5.32: Time history of sloshing height of TX30Y80 - Northridge

Maximum sloshing heights for the 3D models, subjected to 1994 Northridge earthquake, are summarized in Table 5.10. Comparing the results of these 11 tank models, it can be concluded

that for the tanks of the same plan dimensions, sloshing heights at middle of the walls as well as those at the corners of the tanks, increase with water height. A similar trend is observed for the cases that are subjected to El-Centro record. Also, in tanks with the same water level, sloshing height decreases in  $X$  direction when the length of the wall parallel to  $X$  direction increases. A similar trend is observed for the sloshing heights in  $Y$  direction. This trend can be justified by the fact that, in tanks with the same water height, the period of the sloshing mode increases when the length of the walls increases, and as a result, the sloshing height decreases.

Table 5.10: Maximum sloshing height of 3D models subjected to Northridge earthquake

Maximum Sloshing height (mm) - (Group 1)											
Point	A	B	C		A	B	C		A	B	C
SX20Y40	-	-	-	SX20Y60	514	497	995	SX20Y80	-	-	-
MX20Y40	663	590	1120	MX20Y60	-	-	-	MX20Y80	-	-	-
TX20Y40	671	620	1180	TX20Y60	-	-	-	TX20Y80	-	-	-
Maximum Sloshing height (mm) - (Group 2)											
Point	A	B	C		A	B	C		A	B	C
SX30Y40	500	503	988	SX30Y60	501	498	984	SX30Y80	501	493	980
MX30Y40	-	-	-	MX30Y60	-	-	-	MX30Y80	642	612	1100
TX30Y40	-	-	-	TX30Y60	674	614	1192	TX30Y80	681	607	1187
Maximum Sloshing height (mm) - (Group 3)											
Point	A	B	C		A	B	C		A	B	C
SX40Y40	493	500	983	SX40Y60	-	-	-	SX40Y80	495	491	975
MX40Y40	-	-	-	MX40Y60	-	-	-	MX40Y80	-	-	-
TX40Y40	-	-	-	TX40Y60	-	-	-	TX40Y80	-	-	-

It is observed that when similar low frequency excitations, with identical acceleration and frequency content, are applied in  $X$  and  $Y$  directions, clearly, the sloshing height at the corner of the rectangular tank reaches much higher values. Waves generated in  $X$  and  $Y$  directions interact at the corner of the tank, and both waves may have their peak height with a very small phase difference. Therefore, amplitude of the wave at the corner is significantly high. It is observed that the sloshing height at the corner in some cases is almost 100% higher than the sloshing height at the middle of the walls. It is observed that for shallow tanks, at the time the maximum sloshing happens at the corner of the tank, sloshing height at point  $C$  is 96% higher than those at the middle of the walls. For medium and tall height tanks, these ratios are 71% and 75%, respectively. It should be note that these ratios are given relative to the greater value of the sloshing heights at the middle of long or short side wall.

It was observed that, for the low frequency ground motion with the high energy pulse, the ampli-

fication of the sloshing height at the corner of the tank, relative to the middle of the wall is more profound. For those cases, the sloshing height at the corner of the tank can be calculated by summation of the peak sloshing heights in  $X$  and  $Y$  directions that are obtained from the 3D models. Note that in this study, only limited number of tank models are subjected to low frequency ground motion, and then a method is recommended for calculating the sloshing height at the corner of such models. However, this method is conservative for deeper tanks.

Figure 5.33 shows the water surface for the medium height tank model (MX30Y80) subjected to Northridge earthquake both in  $X$  and  $Y$  directions. It can be observed that at the time that the maximum sloshing happens at the corner of the tank, the waves generated in  $X$  and  $Y$  directions are formed with vertical displacements in the same directions, either positive or negative.

In section 5.4.2, it is observed that the amplification of wave height at the corner of the tank against the one at the middle of the wall is profoundly related to the tank plan dimension and water height. On the other hand, in sub-section 5.4.4, it is observed that the frequency content of the external excitation also has a significant effect on the sloshing height at the corner of the tanks. It is observed that when a low frequency content earthquake is applied to the system, the sloshing height at the corner is more likely to be higher in comparison with those at the middle of the walls.

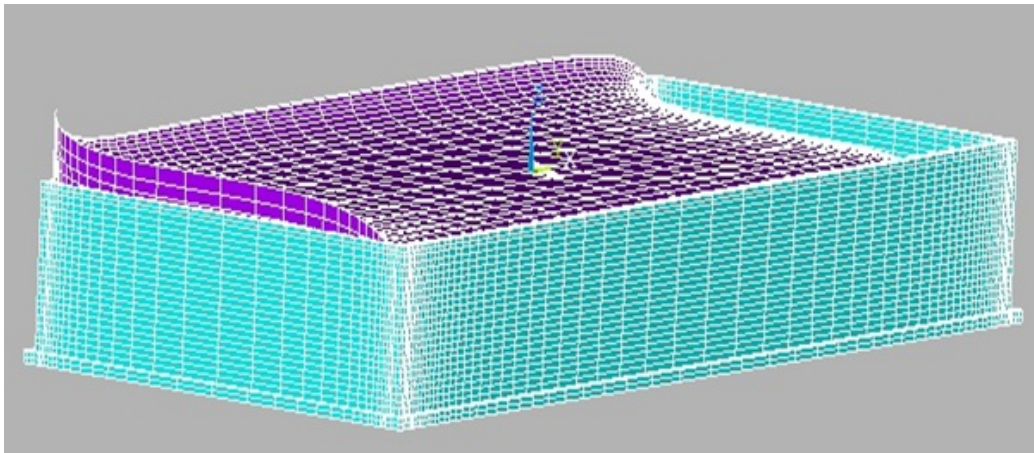


Figure 5.33: Sloshing for MX30Y80 tank model - Northridge earthquake

#### 5.4.5 Comparison of FEM Sloshing Heights with other Methods

In this study, the sloshing characteristic of the rectangular tanks are investigated using FEM, incorporating wall flexibility and liquid damping properties. It is observed that the sloshing re-

sponse of the rectangular tanks is very sensitive to 3D geometry and frequency content of the earthquake. This response is found profoundly affected by water depth and tank plan dimension.

It should be noted that, in this study, tanks are subjected only to the horizontal components of earthquake. As stated by Kana (1979), the sloshing responses of the tanks that are excited vertically are rather insignificant. Ghaemmaghami and Kianoush (2010) also confirmed that when the effect of both horizontal and vertical components of the earthquake are being investigated the effect of the vertical component is insignificant.

To verify the sloshing height calculated in this study, the vertical displacement of the water in the horizontally excited rectangular tank is also calculated by the current analytical formulation and according to Eqn. 5.2. It should be noted that, in this study, the linear wave theory is used and consequently there is a linear relation between the pressure and the sloshing wave height. (NASA-SP-106)

$$d_{max} = \left( \frac{4L}{\pi^2} \right) \left\{ \sum_{n=1}^{\infty} \left( \frac{1}{(2n-1)^2} \frac{S_a(\omega_n, \xi_n)}{g} \right)^2 \right\}^{1/2} \quad (5.2)$$

Where  $L$  is the length of the tank and  $g$  is acceleration gravity.  $S_a(\omega_n, \xi_n)$  is the spectral response acceleration at period  $T_n = \frac{2\pi}{\omega_n}$  corresponding with the damping ratio of  $\xi_n$ .

It can be seen that, as a consequence of Eqn. 5.2, the sloshing waves form due to gravity. In the absence of gravity no sloshing wave forms at the surface of the water. In addition, according to Eqn. 5.2, the maximum vertical displacement of the water is proportional to the spectral acceleration associated with the natural frequencies of each mode. These values are less than the peak horizontal ground acceleration. The value of sloshing heights at middle cross section of the wall are calculated based on response-spectrum modal superposition method and summarized in Table 5.11.

Virella et al. (2008) suggested that the sloshing response is dominated by the first mode and contribution of higher order sloshing modes can be neglected for the calculation of the sloshing pressure and surface wave amplitude. Therefore, Eqn. 5.2 can be simplified for the first fundamental mode of sloshing and is used to verify the proposed model. Figure 5.34 represents the acceleration response spectrum of the longitudinal component of scaled El-Centro earthquake, considering 0.5% damping for convective and 5 % damping for impulsive. These graphs are used to calculate the sloshing height.

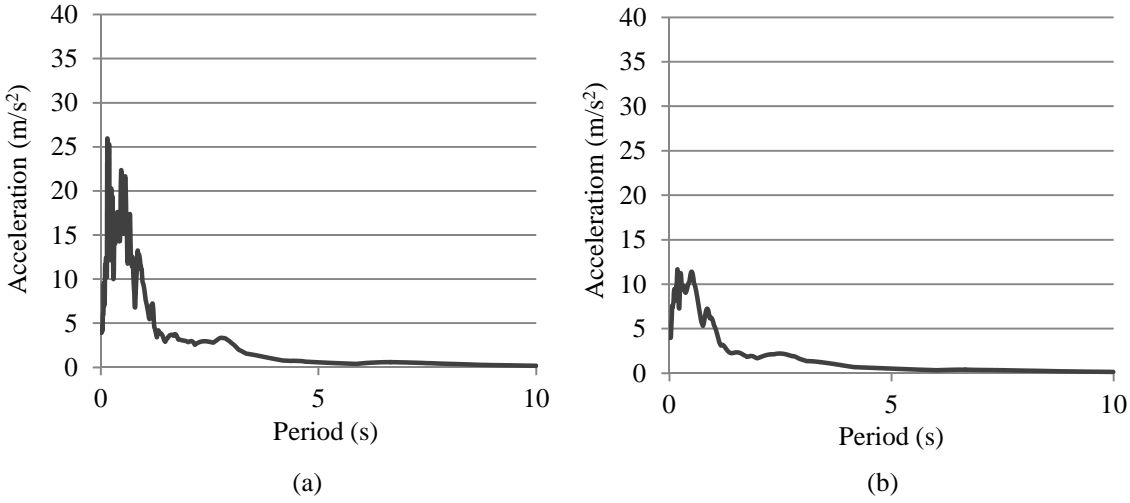


Figure 5.34: Acceleration response spectrum of scaled (N-S) El-Centro earthquake: (a) 0.5 % damping, (b) 5% damping

Housner in 1963 suggested the following formulation for calculating the sloshing height in horizontally excited rectangular tanks.

$$d_{max} = \frac{0.527\left(\frac{L}{2}\right) \coth\left(1.58\frac{2h}{L}\right)}{\frac{g}{\omega^2 \theta_h\left(\frac{L}{2}\right)} - 1} \quad (5.3)$$

In Eqn. 5.3,  $\theta_h$ , is the angular amplitude of free oscillation of the fluid surface. This equation now being employed for the calculation of the required free-board in ACI 350.3-06 code. Moreover, the design sloshing heights are calculated according to Housner's formulation and are presented in Table 5.12. The design sloshing height is calculated at the Imperial Valley location where  $S_{DS} = 1.0g$ . Importance factor,  $I$ , equal to 1.0 is used.

For all three groups of tanks explained previously, the sloshing height calculated according to finite element 3D and 2D models are compared with the results of the analytical approach (RSM) and ACI code. It should be noted that the value of the sloshing heights for the 3D models are the average of the sloshing heights in the middle cross-section of the long side walls when the N-S component of the El-Centro earthquake is applied parallel to shorter side walls plane with length symbolized as  $L$ . Those sloshing heights are average of the results of the cases that have identical shorter wall dimension. For the 2D models, the sloshing heights are calculated in the direction

Table 5.11: Analytical sloshing height

Maximum sloshing height									
(mm)									
Point	$L$	$A$	$L$	$A$	$L$	$A$	$L$	$A$	
	(m)		(m)		(m)		(m)		
Shallow	S1	20	229	S2	30	186	S3	40	141
Medium	M1	20	188	M2	30	293	M3	40	169
Tall	T1	20	212	T2	30	352	T3	40	252

Table 5.12: Design sloshing height according to ACI 350.5-06

Maximum sloshing height										
(mm)										
Point	$A$	$A$	$A, B$	$B$	$B$					
	$L$	$L$	$L$	$L$	$L$	$L$	$L$	$L$	$L$	$L$
	(m)		(m)		(m)		(m)		(m)	
Shallow	20	660	30	491	40	385	60	266	80	192
Medium	20	802	30	647	40	526	60	369	80	280
Tall	20	885	30	772	40	660	60	487	80	384

parallel to the  $X$  coordinate, when the N-S component of the El-Centro earthquake is applied in  $X$  direction. For 2D models as well the length of the tank wall is symbolized as  $L$ .

The comparisons are presented in Figures 5.35, 5.36, and 5.37 for group 1 ( $L = 20m$ ), group 2 ( $L = 30m$ ), and group 3 ( $L = 40m$ ) respectively. As discussed previously, results show that 3D models generally estimate higher values in comparison with 2D models. This directs that 3D geometry has a significant effect on the sloshing response of the tank. It can be perceived that, for group 1 of the tanks, ACI code overestimates the value of vertical displacement of the water. The results also confirmed that response-spectrum method (RSM) underestimates value of sloshing in comparison with both 3D and 2D models.

It should be noted that the amplification factor,  $\alpha$ , introduced in the section 5.4.1 can be employed to calculate the design sloshing height at the middle of the tank walls, and is applicable to the values of the sloshing height estimated according to ACI code. However, the amplification coefficient  $\beta$ , introduced in section 5.4.2, seems to calculate very conservative values for the sloshing height at the corner of the tanks, and can be modified as follows to estimate the design sloshing height:

- For  $B/L \geq 2.0$ ,  $\beta = 1.3$
- For  $B/L < 2.0$ ,  $\beta = 1.5$

Note that for the low frequency ground motion, the amplification of the sloshing height at the corner of the tank, relative to the middle of the wall is more profound. For these cases, a conservative method to estimate the peak sloshing height at the corner of the rectangular tank is to use the summation of the peak sloshing heights in  $X$  and  $Y$  directions. Similarly, this method is applicable to the sloshing heights estimated according to ACI code. The ACI sloshing heights should be amplified by the amplification coefficient  $\alpha$  to consider the effects of 3D geometry.

Finally, the sloshing height values calculated by FEM are compared with the experimental results of shaking table test conducted by Koh et al. (1998). The test was directed using 6-DOF shaking table on a three-dimensional tank model made of acrylic plates with density of  $1200 \text{ kg/m}^3$ . The modulus of elasticity equals to  $2.9 \times 10^9 \text{ N/m}^2$  and Poisson's ratio as 0.35. The measured peak table peak acceleration was 0.22g. The scaled (N-S) El-Centro earthquake was used as the input ground motion in the direction perpendicular to the long side wall ( $X$  direction). To determine the viscous damping ratio, the test was first completed on the empty tank, and this ratio was found to be nearly 5%. Two water level gauges were placed at the middle cross section of the longer side wall to measure the vertical displacement of the free surface water.

In this study, a finite element model of the tank tested experimentally is analyzed. The tank has the following dimensions.

$$L_x = 1.1 \text{ m} \quad L_y = 0.57 \text{ m} \quad H_w = 0.9 \text{ m} \quad H_L = 0.7 \text{ m} \quad t_w = 0.035 \text{ m}$$

Figure 5.38 shows the time history of the wave height at the middle cross section of the long side wall for both experimental results and numerical. The sloshing heights at the middle cross section of the long side wall ( $X$ ) calculated using FEM are in a satisfactory agreement with the experimental results. The slight difference can be justified as a result of discrepancies in the input data of the ground motion for the shaking table. Moreover, as a result of increase in energy dissipation during the experiment which leads to changes in fluid damping properties, the sloshing height calculated by FE is higher than the experimental results.

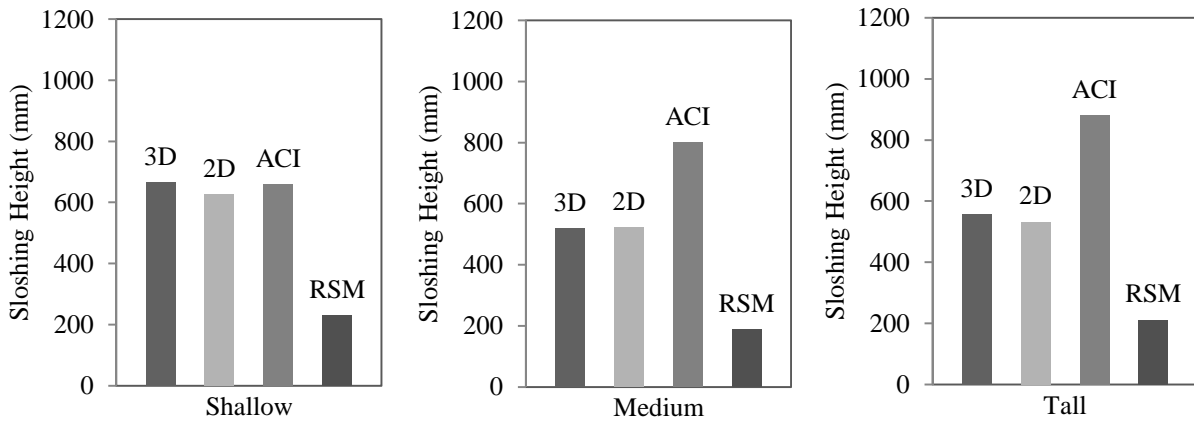


Figure 5.35: Sloshing height for the tanks with  $L = 20$  m (Group 1)

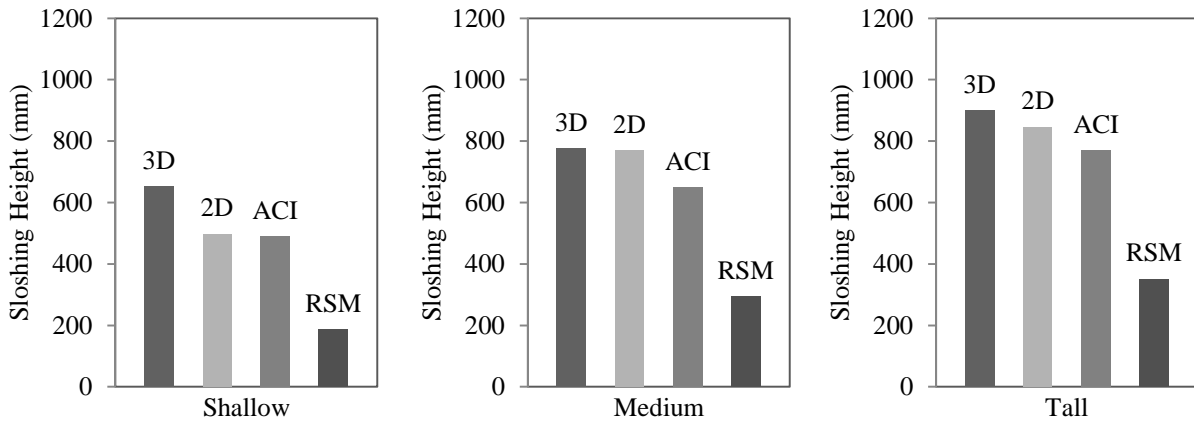


Figure 5.36: Sloshing height for the tanks with  $L = 30$  m (Group 2)

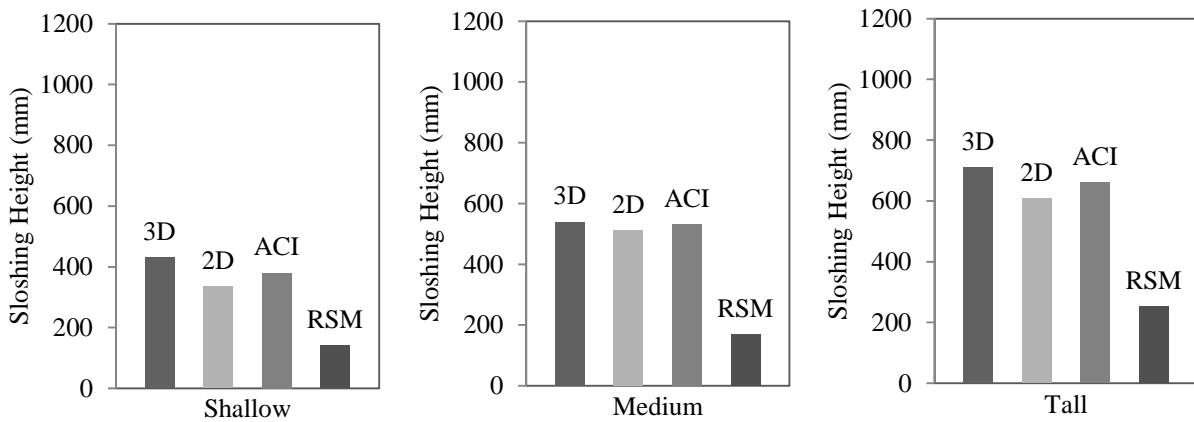


Figure 5.37: Sloshing height for the tanks with  $L = 40$  m (Group 3)

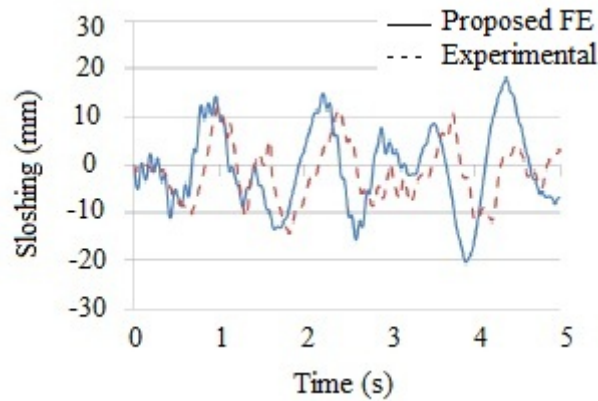


Figure 5.38: Time history of sloshing for the small tank comparing FEM and experimental results

## 5.5 Hydrodynamic Pressure on the Walls

### 5.5.1 Vertical Pressure Distribution

The hydrodynamic pressures along the height of the walls are calculated for all tanks considered in this study. The hydrodynamic pressures are calculated at the middle cross section of the long side wall and at the middle cross section of the shorter side wall. These values are combined by both impulsive and convective components of the hydrodynamic pressure. The results are presented for 3D and 2D models to investigate the effect of the 3D geometry condition on the response of the rectangular tanks. Among different tanks under investigation, the results are presented for some of the tanks.

Figure 5.39 shows the hydrodynamic pressure distribution along the height of a shallow tank model named as SX30Y60. It should be noted that this case represents the same shallow tank as discussed by Ghaemmaghami (2010). The tank wall has thickness of  $0.6\text{m}$ , and the tank is modelled by appropriate flexible boundary conditions. The values of hydrodynamic pressures are calculated along the height of the tank. According to Figure 5.39, the peak hydrodynamic pressure along the height of the wall seems to be amplified by 27% in 3D model in comparison with the peak hydrodynamic pressure in 2D model. During the 20sec of the analysis, the maximum hydrodynamic pressure at the bottom of the 3D tank is  $22\text{kPa}$ . The hydrodynamic pressure at the free water surface of the 3D model is  $8.0\text{kPa}$ . On the other hand, for the 2D model, peak hydrodynamic pressure at the bottom of the tank and at the free surface are  $19\text{kPa}$  and  $7.4\text{kPa}$ ,

respectively. It is observed that in the 3D model, the hydrodynamic pressure at the bottom of the tank is amplified by 18% in comparison with that of 2D model. Also, the hydrodynamic pressure at the free water surface of the 3D model is amplified by 7% in comparison with 2D model. It should be noted that, for this tank model,  $B/L$  and  $L/H_L$  ratios are 2.0 and 5.45, respectively.

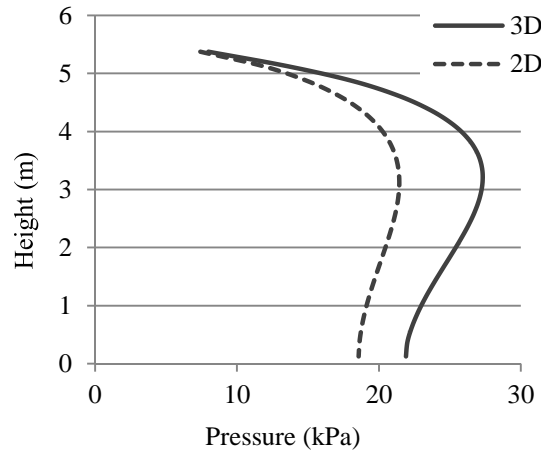


Figure 5.39: Vertical hydrodynamic pressure distribution for SX30Y60 for 2D and 3D models

Figures 5.40 and 5.41 show the hydrodynamic pressure distribution along the height of the tanks with water depth of 8.0m and 11.0m, respectively. As shown in Figure 5.40, for MX30Y60, the impulsive and convective component of the pressure are also amplified due to 3D geometry. The maximum the hydrodynamic pressure at the bottom of the 3D tank model is 31 kPa. Moreover, the maximum pressure at the free surface water is 9.7 kPa. For the 2D model, the hydrodynamic pressure at the bottom of the tank and at the free water surface are 11.6 and 30 kPa, respectively. It should be noted that for the 3D model, the hydrodynamic pressure at the tank bottom is increased by 4% in comparison with 2D model. Also, the at the free surface of the water is minus 17%. The maximum hydrodynamic pressure along the height of this medium tank model is amplified by 23%, in comparison with the peak hydrodynamic pressure along the height of the 2D model. It should be noted that, for tank model MX30Y60,  $B/L$  and  $L/H_L$  ratios are 2.0 and 3.75, respectively.

Figure 5.41 shows the pressure distribution for the tank model TX30Y60 with  $H_L = 11.0m$ . It should be noted that, for this tank model,  $B/L$  and  $L/H_L$  ratios are 2.0 and 2.73, respectively. In this case, for the 3D model, the maximum hydrodynamic pressure at the bottom of the tank and at the free water surface are 36 kPa and 14 kPa, respectively. As shown in this figure, the maximum hydrodynamic pressure at the bottom of the tank in the 3D tank are increased by 3% against 2D tank model. Comparing the results of 3D models with the 2D models, the hydrodynamic pressure at the free water surface drops by 13%. It should be noted that the maximum hydrodynamic

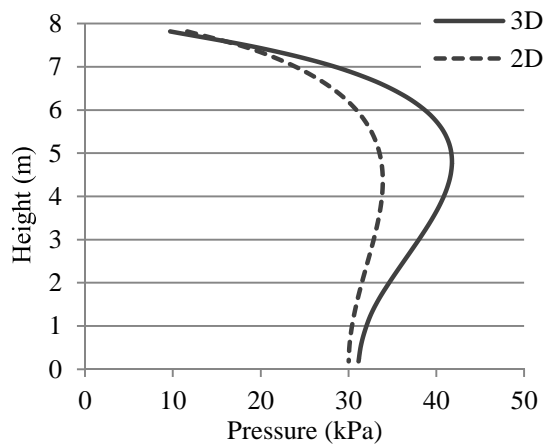


Figure 5.40: Vertical hydrodynamic pressure distribution for MX30Y60 for 2D and 3D models

pressure along the height of the 3D model is 41% higher than that of the 2D model.

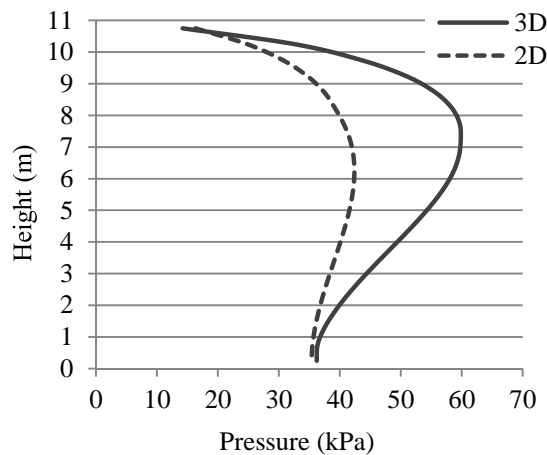


Figure 5.41: Vertical hydrodynamic pressure distribution for TX30Y60 for 2D and 3D models

The pressure distributions are also presented for three other tank plan dimensions with larger values of  $B/L$  ratio. These tanks have longer side wall length of  $80m$ ; whereas, the other walls are  $20m$ . Again the results are available for different water depth level. The tanks are named as SX20Y80, MX20Y80 and TX20Y80 with water level of  $5.5$ ,  $8.0$  and  $11.0m$  respectively. It should be noted that, for these tanks,  $B/L$  ratios equal to  $4.0$ .  $L/H_L$  ratios are  $3.64$ ,  $2.5$  and  $1.82$  for SX20Y80, MX20Y80 and TX20Y80, respectively.

Figure 5.42 shows the hydrodynamic pressure distribution for the tank model SX20Y80. For the 3D model, the hydrodynamic pressure at the bottom of the tank is  $21kPa$  and at free surface is  $7.7kPa$ . For the 2D model, hydrodynamic pressure at the bottom and at the free surface are  $19$  and

7.2 kPa, respectively. As can be observed, the hydrodynamic pressure at the bottom is amplified by 13% and at the free water surface is increased by 7%. The peak hydrodynamic pressure along the height of wall in the 3D model is 26 kPa and is 21% higher than that for 2D model.

Figures 5.43 and 5.44 show the pressure distribution along the height of MX20Y80 and TX20Y80, respectively. As is shown in Figure 5.43, for the tank with  $H_L = 8.0\text{ m}$  (MX20Y80) the hydrodynamic pressure at the surface of the water in the 3D model is 9.6 kPa; on the other hand, for the 2D model, it is calculated as 11 kPa and is decreased by 16%.

For tank model TX20Y80, hydrodynamic pressure at the free water surface is estimated as 13 kPa for the 3D and is 23% less in comparison with the 2D model. The hydrodynamic pressure at the bottom of the 3D tank model is 32 kPa and is 10% lower than that for the 2D model. The peak hydrodynamic pressure along the height of 3D tank models is 35 kPa for case MX20Y80 and 52 kPa for TX20Y80 which are increased by 2 % and 18%, respectively, in comparison with the 2D models.

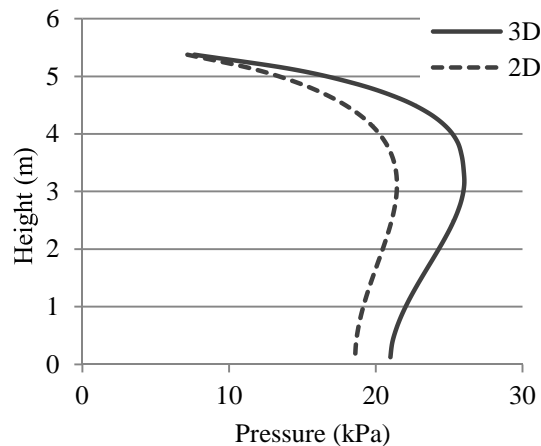


Figure 5.42: Vertical hydrodynamic pressure distribution for SX20Y80 for 2D and 3D models

Summarizing the results, the peak hydrodynamic pressures along the height of the tank walls are compared for all of tank configurations summarized in Table 5.1. Figure 5.45 shows the ratios of the peak hydrodynamic pressures along the height of the tank walls in 3D models in comparison with the 2D models, against  $L/H_L$  ratio. In this study, it is observed that the 3D models calculate higher value for the peak hydrodynamic pressure along the height of the walls with a maximum difference of 46%.

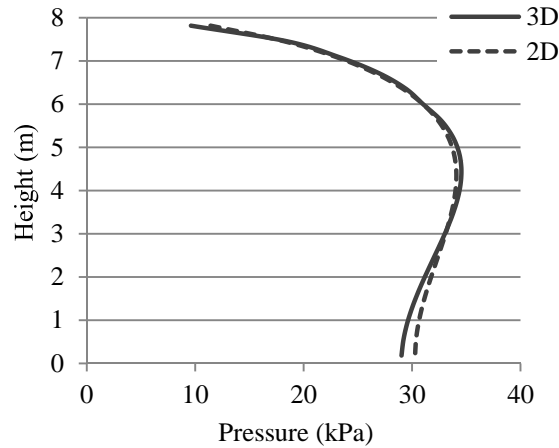


Figure 5.43: Vertical hydrodynamic pressure distribution for MX20Y80 for 2D and 3D models

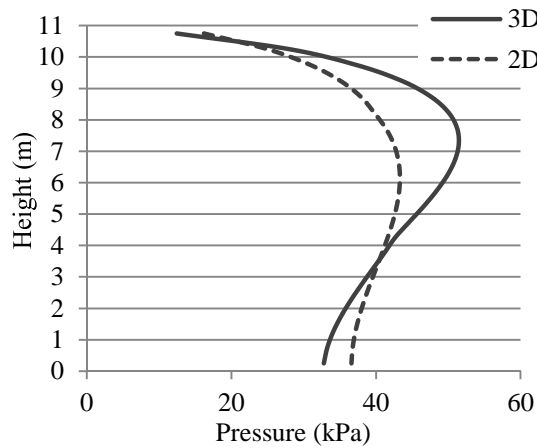


Figure 5.44: Vertical hydrodynamic pressure distribution for TX20Y80 for 2D and 3D models

## 5.5.2 Lateral Hydrodynamic Pressure Distribution

In this section, the lateral distribution of the hydrodynamic pressure on the tank wall is presented for shallow tank model SX30Y60. The hydrodynamic pressures is accompanied by both impulsive and convective components. Dimension of the tank is as follows:

$$L_X = 15m \quad L_Y = 30m \quad H_L = 5.5m \quad H_W = 6.0m \quad t_W = 600mm$$

It should be noted that in the 3D tank model, the hydrodynamic pressure distribution varies along the height of the tank wall as well as in the horizontal direction over the tank wall. If the tank is subjected to external acceleration in the direction perpendicular to the longer wall, hydrodynamic pressure at the corner of the tank is lower than that at the middle cross section of the wall. Figure

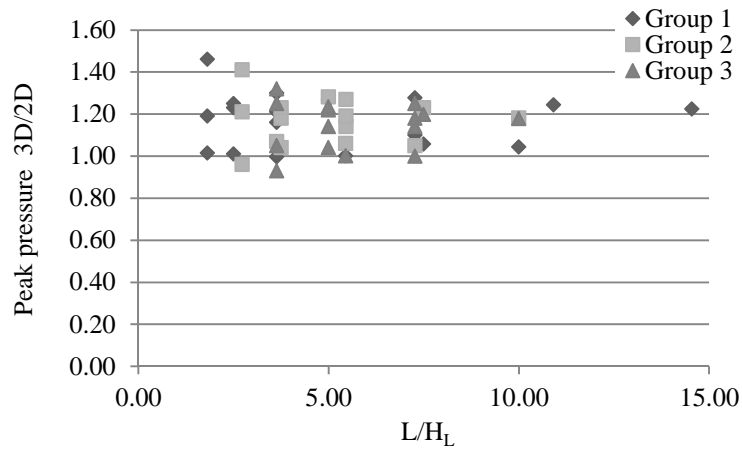


Figure 5.45: Increase in 3D response in comparison with 2D in the form of peak hydrodynamic pressure against  $L/H_L$

5.46 illustrates the 3D hydrodynamic pressure distribution.

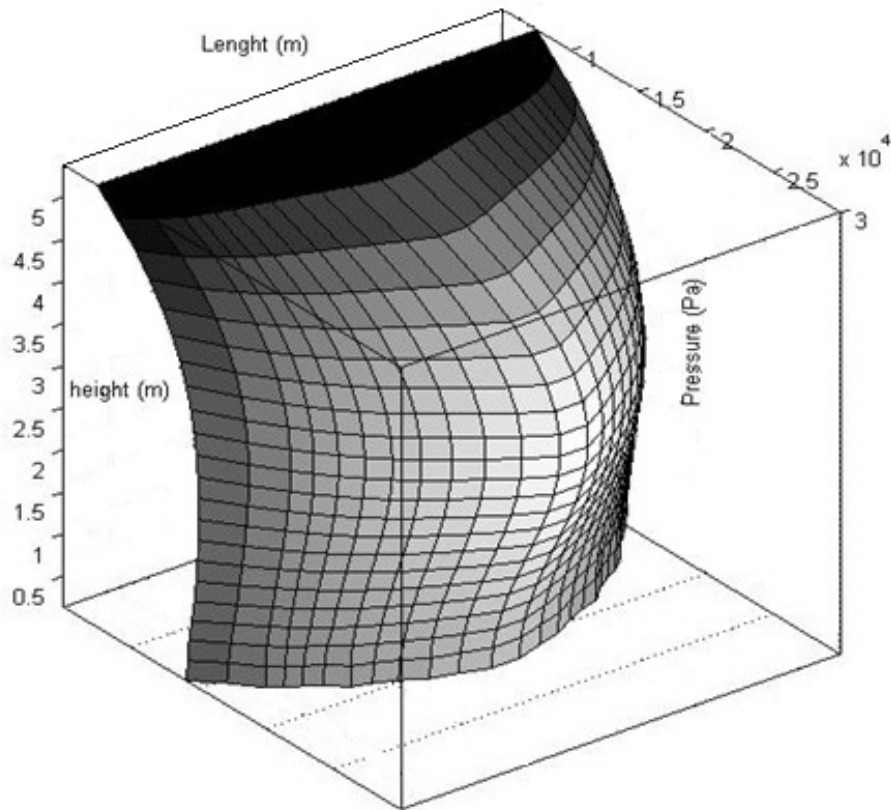


Figure 5.46: Hydrodynamic pressure distribution on the 3D tank model (case SX30Y60)

### 5.5.3 Comparison of FEM Hydrodynamic Pressure with Analytical Approach

In this study, the hydrodynamic pressures acting on the wall of the rectangular tanks are calculated introducing impulsive wave absorbcency boundary condition and fluid viscous damping conditions. In current analytical method, the impulsive pressure distribution can be calculated using potential function method. As stated before, this method ignores both flexible boundary condition and fluid viscosity. The following equation derived by Haroun and Housner (1981) will be used to verify the hydrodynamic pressure distribution along the rigid tank wall:

$$P = \sum_{n=1}^{\infty} \frac{2(-1)^n \rho_l}{\lambda_{i,n}^2 H_l} \tanh(\lambda_{i,n} L_x) \cos(\lambda_{i,n} y) \ddot{u}(t) \quad (5.4)$$

Where  $\lambda_{i,n} = (2n - 1) \pi$ , and  $\ddot{u}(t) = \ddot{u}_g(t)$ . For the rigid boundary condition, the acceleration along the height of the wall is the same as the acceleration of the ground.

To verify the proposed model, the results of the FEM calculations of the rigid tanks are compared with the analytical solution. It should be noted that the rigid tanks are modelled in 2D geometry and energy dissipation is ignored. These tanks have width of 30m, and water depth of 5.5, 8.0 and 11 m for shallow (s), Medium (M), and tall (T) tank, respectively. The comparison of impulsive pressure is shown in Figure 5.47. These comparisons show that FEM results are in a good agreement with analytical solution for the 2D rigid tanks.

## 5.6 Base Reactions

In this section, the reactions of the flexible tank models are obtained in 3D space and comparisons are made with 2D results. The base shear and peak moments at the bottom of the tanks are calculated. The values for the peak base shear and moment at the bottom of the 3D tank walls are calculated in both  $X$  and  $Y$  directions. These values, for the three-dimensional models, are divided by the length of the walls to estimate the average base shear and moment on a 1 m strip of the wall. The peak values are summarized in Tables 5.13, 5.14, and 5.15 for shallow, medium and tall tanks, respectively.

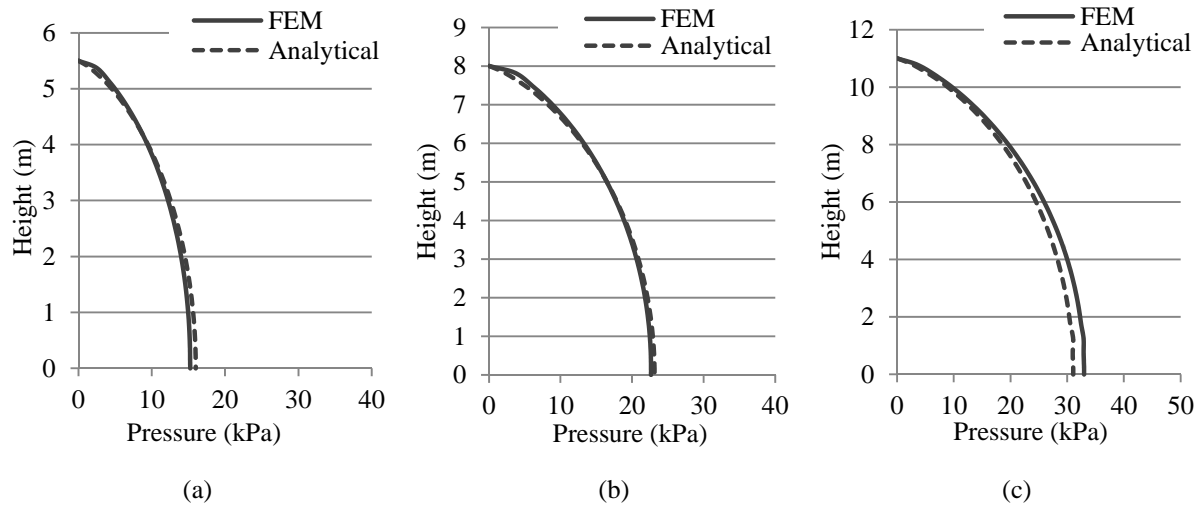


Figure 5.47: Comparison of the hydrodynamic pressure distribution: (a) Shallow tank, (b) Medium tank, (c) Tall tank

Table 5.13: Peak base force and moment at base of walls for the shallow tanks ( $H_L = 5.5\text{ m}$ )

	Case	$F_X$ kN/m	$M_Y$ kN.m/m	$F_Y$ kN/m	$M_X$ kN.m/m
Group 1	SX20Y40	397.02 (0.98)*	683.19 (1.25)	378.52 (1.33)	1082.35 (0.83)
	SX20Y60	453.58 (1.12)	638.83 ( 1.17)	518.63 (1.38)	1864.38 (0.68)
	SX20Y80	433.08 (1.07)	620.99 ( 1.13)	607.28 (1.47)	2820.13 (0.67)
Group 2	SX30Y40	463.68 (1.04)	707.15 ( 0.75)	366.35 (1.29)	1010.69 ( 0.78)
	SX30Y60	435.48 ( 0.98)	775.48 ( 0.82 )	466.63 (1.24)	2167.48 (0.79)
	SX30Y80	492.39 (1.11)	737.16 (0.78)	575.88 (1.40)	3249.72 (0.78)
Group 3	SX40Y40	532.61 ( 1.07)	978.57 (0.63)	354.61 (1.24)	1058.00 (0.81)
	SX40Y60	579.41 (1.17)	1152.76 (0.74)	450.86 (1.20)	2108.80 (0.77)
	SX40Y80	551.33 (1.11)	1203.22 (0.77)	517.88 (1.26)	3428.37 (0.82)

\*Values in bracket shows the ratio of the 3D response over the 2D response

Table 5.14: Peak base force and moment at base of walls for the medium height tanks ( $H_L = 8.0m$ )

	Case	$F_X$ kN/m	$M_Y$ kN.m/m	$F_Y$ kN.m/m	$M_X$ kN/m
Group 1	MX20Y40	674.18 (1.01)★	1648.97 (1.05)	567.81 (1.25)	1765.31 (1.06)
	MX20Y60	665.04 (0.93)	1580.29 (1.20)	753.36 (1.21)	3570.13 (0.96)
	MX20Y80	671.91 (0.94)	1559.05 (1.19)	895.99 (1.29)	5267.38 (0.82)
Group 2	MX30Y40	761.70 (0.87)	1686.58 (1.04)	514.42 (1.13)	1599.17 (0.96)
	MX30Y60	748.91 (0.86)	1670.61 (1.03)	621.8 (1.00)	3153.84 (0.85)
	MX30Y80	750.73 (0.86)	1671.38 (1.03)	742.66 (1.07)	4702.26 (0.73)
Group 3	MX40Y40	841.11 (1.05)	2553.27 (0.86)	499.26 (1.10)	1531.47 (0.92)
	MX40Y60	821.23 (1.03)	2689.49 (0.91)	683.92 (1.10)	3202.46 (0.86)
	MX40Y80	816.65 (1.02)	2772.19 (0.94)	795.79 (1.14)	4807.39 (0.75)

★Values in bracket shows the ratio of the 3D response over the 2D response

Table 5.15: Peak base force and moment at base of walls for the tall height tanks ( $H_L = 11.0m$ )

	Case	$F_X$ kN/m	$M_Y$ kN.m/m	$F_Y$ kN.m/m	$M_X$ kN/m
Group 1	TX20Y40	1380.71 (1.03)★	7371.25 (1.18)	1233.46 (1.20)	6149.21 (2.15)
	TX20Y60	1560.97 (1.16)	7423.39 (1.19)	1626.84 (1.32)	6104.98 (1.14)
	TX20Y80	1408.58 (1.05)	6916.10 (1.11)	2041.77 (1.41)	7192.02 (0.84)
Group 2	TX30Y40	1600.89 (1.05)	6900.96 (1.39)	1160.92 (1.13)	5101.69 (1.78)
	TX30Y60	1783.87 (1.18)	6325.41 (1.28)	1517.77 (1.23)	5481.83 (1.02)
	TX30Y80	1593.48 (1.05)	5911.97 (1.19)	1869.40 (1.29)	8605.22 (1.01)
Group 3	TX40Y40	1790.52 (1.09)	6376.70 (1.23)	980.80 (0.95)	4754.96 (1.66)
	TX40Y60	1940.92 (1.18)	6235.14 (1.20)	1193.26 (0.97)	6308.68 (1.17)
	TX40Y80	1743.62 (1.06)	5972.44 (1.15)	1517.41 (1.05)	9984.14 (1.17)

★Values in bracket shows the ratio of the 3D response over the 2D response

### 5.6.1 Base Shear

Three cases with the similar plan dimensions are chosen to represent the time histories of the structural responses. Figures 5.48, 5.49 and 5.50 show the time history of the base shear in the direction perpendicular to the long side wall for the SX40Y80, MX40Y80 and TX40Y80 tank models, respectively. The tanks have plan dimension of  $40m \times 80m$ .

Figure 5.48 shows that, in 3D model of SX40Y80, the maximum base shear is  $551 kN/m$ . However, the peak base shear in 2D model reduces to  $496 kN/m$  and happens at the similar time. In this case, base shear is increased by 11% due to 3D geometry condition.

In Figure 5.49, time history of the base shear for both 3D and 2D models are shown for tank model MX40Y80. The peak base shear for the 3D model is  $816 kN/m$ . This is amplified by 2% in comparison with the peak shear of  $800 kN/m$  for the 2D model.

Similarly, as shown in Figure 5.50, the base shear of tank model TX40Y80 is higher in the 3D model, in comparison with 2D model, and is amplified by 6%. Peak shear happened at 2.38 second of excitation for both models and is  $1743 kN/m$  and  $1637 kN/m$  for the 3D and 2D models, respectively.

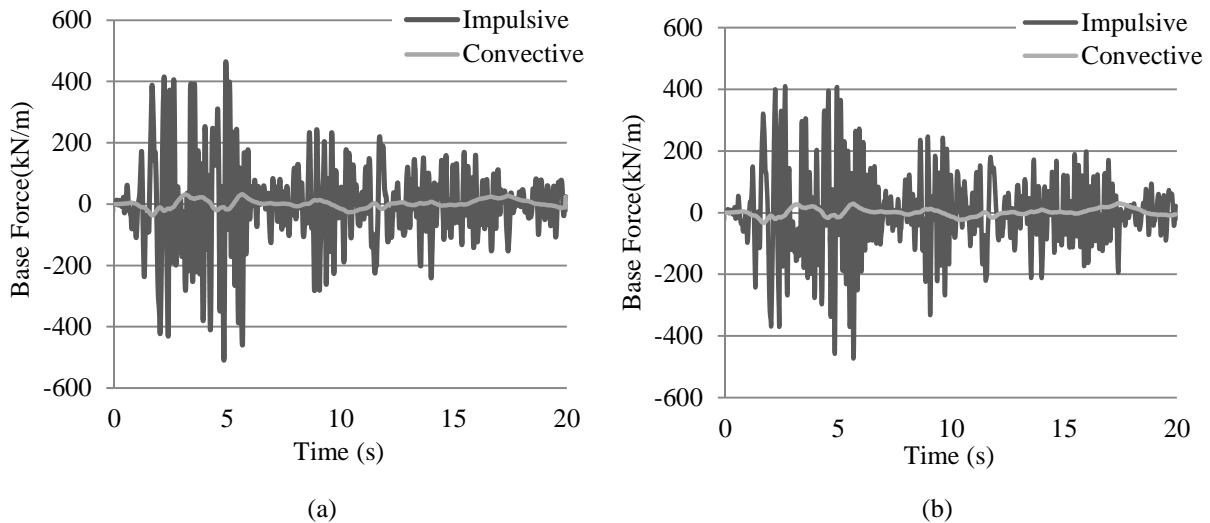


Figure 5.48: Time history of the base shear of SX40Y80: (a) 3D model, (b) 2D model

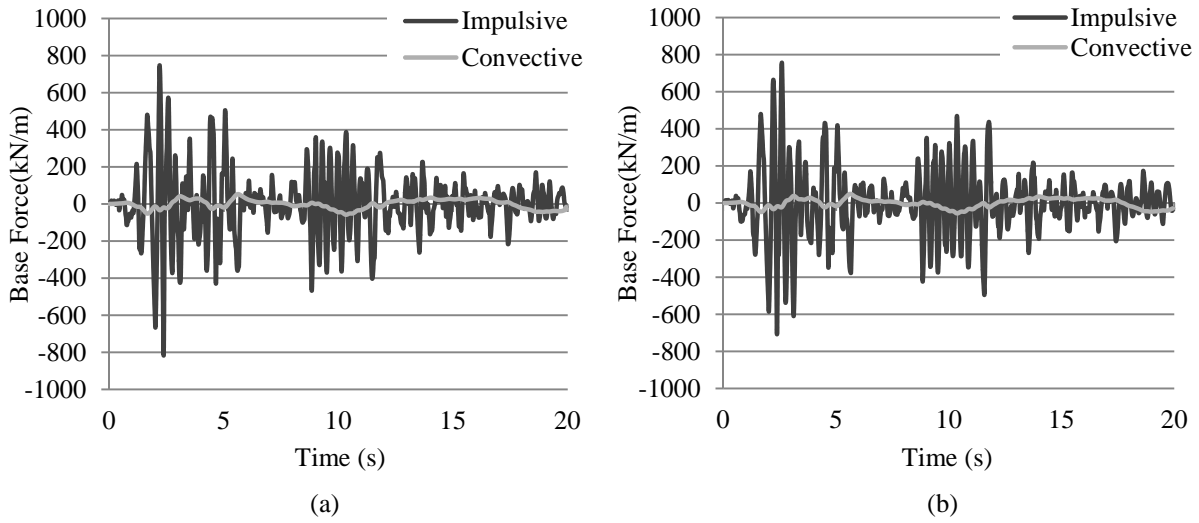


Figure 5.49: Time history of the base shear of MX40Y80: (a) 3D model, (b) 2D model

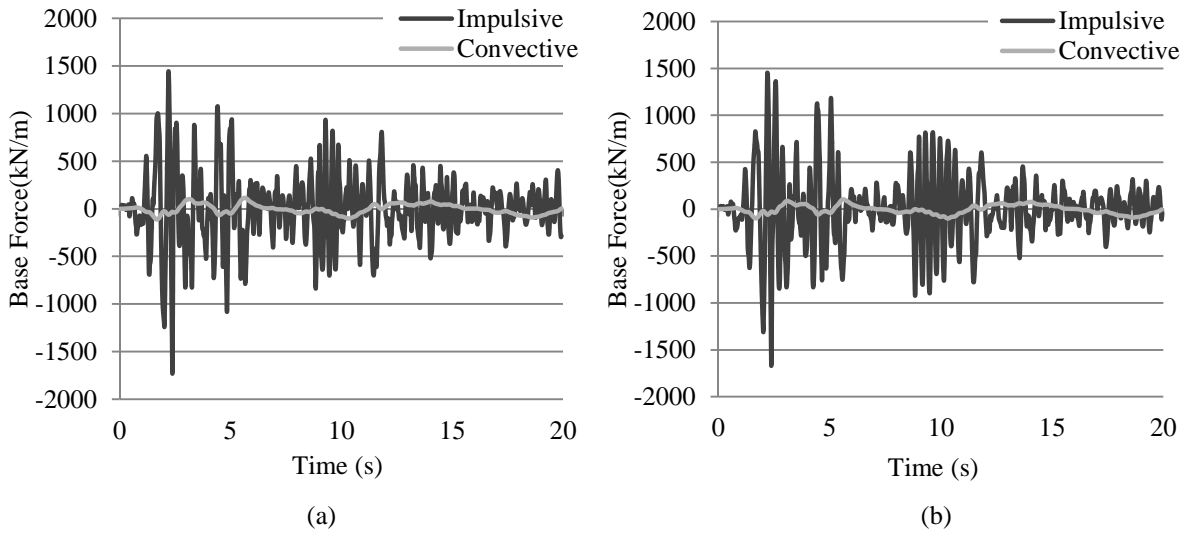


Figure 5.50: Time history of the base shear of TX40Y80: (a) 3D model, (b) 2D model

It is observed that the 3D models estimated much higher values for base shear in comparison with the 2D models; particularly, when the analysis is done on the cross section parallel to long side wall. Basically, when the tank is modelled in 2D geometry for a plane-strain section, the effect of the walls parallel to the direction of the excitation is ignored. However, especially when the  $B/L$  ratio is smaller than 1.0, this fact can not be ignored. The inertia forces of the long side walls is relatively high to be ignored.

In order to consider the effect of three-dimensional geometry, the amplification coefficient  $f$ , can

be introduced to amplify the base shear:

- For  $B/L \geq 1.0$ ,  $f = 1.3$
- For  $B/L < 1.0$ ,  $f = 1.5$

where  $B$  and  $L$  are dimension of the tank wall perpendicular and parallel to direction under investigation, respectively.

Figure 5.51 shows the changes in the ratio of the peak base force values for 3D models over 2D models, against  $L/H_L$  ratios. It can be observed that the 3D models result in higher values as compared with 2D models.

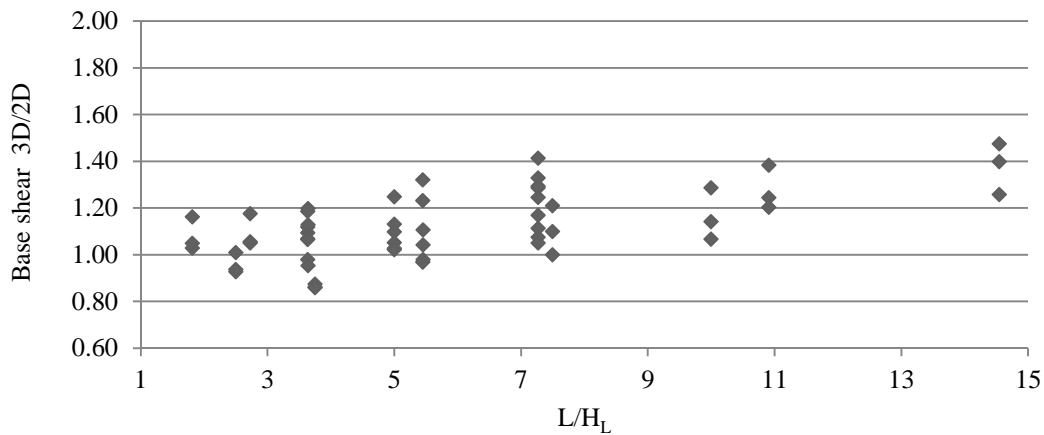


Figure 5.51: 3D/2D peak base shear against  $L/H_L$

## 5.6.2 Overturning Moment

For the 3D and 2D rectangular tank, the overturning moments are calculated at the ground level. Values of the overturning moment are summarized in Tables 5.48, 5.49 and 5.50 for the 3D tank models. Among all the tanks under investigation, three tank models with plan dimension of  $20 \times 60 \text{ m}^2$  are selected to present the time histories of the overturning moments.

For the 3D tank models, the overturning moment is calculated about  $Y$  axis, when the N-S component of El-Centro earthquake is applied perpendicular to  $Y$  axis. The results of the overturning moment at the ground level in the 2D models are also presented for the cases that the N-S component of the ground motion is applied to the tanks with  $L = 20 \text{ m}$ . Figures 5.52, 5.53 and

5.54 illustrate the time histories of the moments for the tank models SX20Y60, MX20Y60 and TX20Y60, respectively.

For the 3D model of SX20Y60, the value of the absolute maximum value of impulsive overturning moment is  $602 \text{ kN.m/m}$ . However, the impulsive overturning moment in the 2D model is  $498 \text{ kN.m/m}$ . In comparison with the 2D model, the impulsive component of the overturning moment at the ground level for the 3D models is increased by 21%. The peak convective component of the moment for the 3D shallow model is  $153 \text{ kN.m/m}$  and for the 2D models, is  $134 \text{ kN.m/m}$ . The convective component is as well increased by 14%.

Figure 5.53 shows the time history of the impulsive and convective components of the moment for the medium height tank model (MX20Y60). For this case, the total moment is calculated 20% higher for the 3D model. The peak impulsive moment for the 3D and 2D model are  $1597 \text{ kN.m/m}$  and  $1361 \text{ kN.m/m}$ , respectively, both happening at  $2.38 \text{ sec}$ . However, the absolute maximum value of convective component are estimated similar value of  $130 \text{ kN.m/m}$  for 3D and 2D models. In comparison with the 2D model, it is observed that the impulsive and convective components of the overturning moment in the 3D model are increased by 17% and 0%, respectively.

Moreover, for the tank model TX20Y60, the results are shown in Figure 5.54. Both 3D and 2D models follow a similar trend for the moment; however, the peak moment for the 3D model is 19% higher than that of 2D model. The peak impulsive moment is  $7284 \text{ kN.m/m}$  for the 3D model happening at  $2.38 \text{ sec}$ . For the 2D model, however, the impulsive moment is  $6283 \text{ kN.m/m}$ . On the other hand, the convective pressure is calculated as  $421 \text{ kN.m/m}$  for the 3D model and is 25% less than that of 2D model.

Figure 5.55 illustrates the ratio of the maximum base moment values for 3D models over 2D models against length to height ratios.

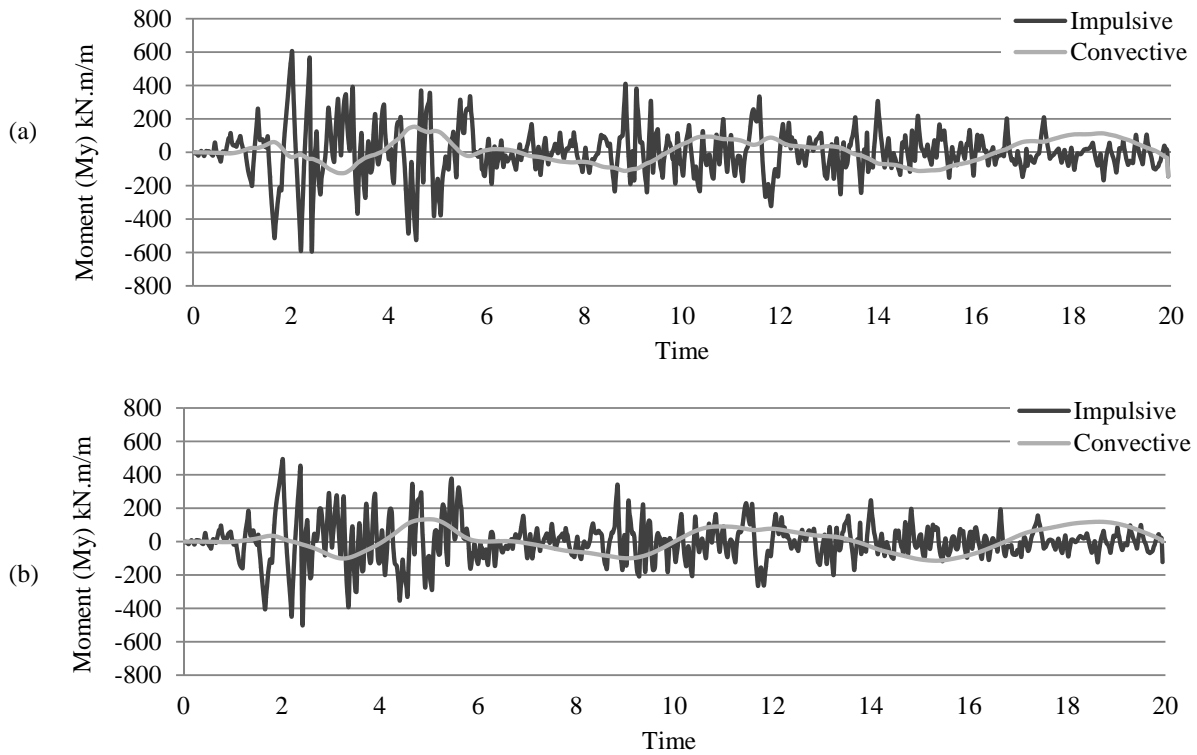


Figure 5.52: Time history of impulsive and convective component of moment ( $M_y$ ) of SX20Y60: (a) 3D model, (b) 2D model

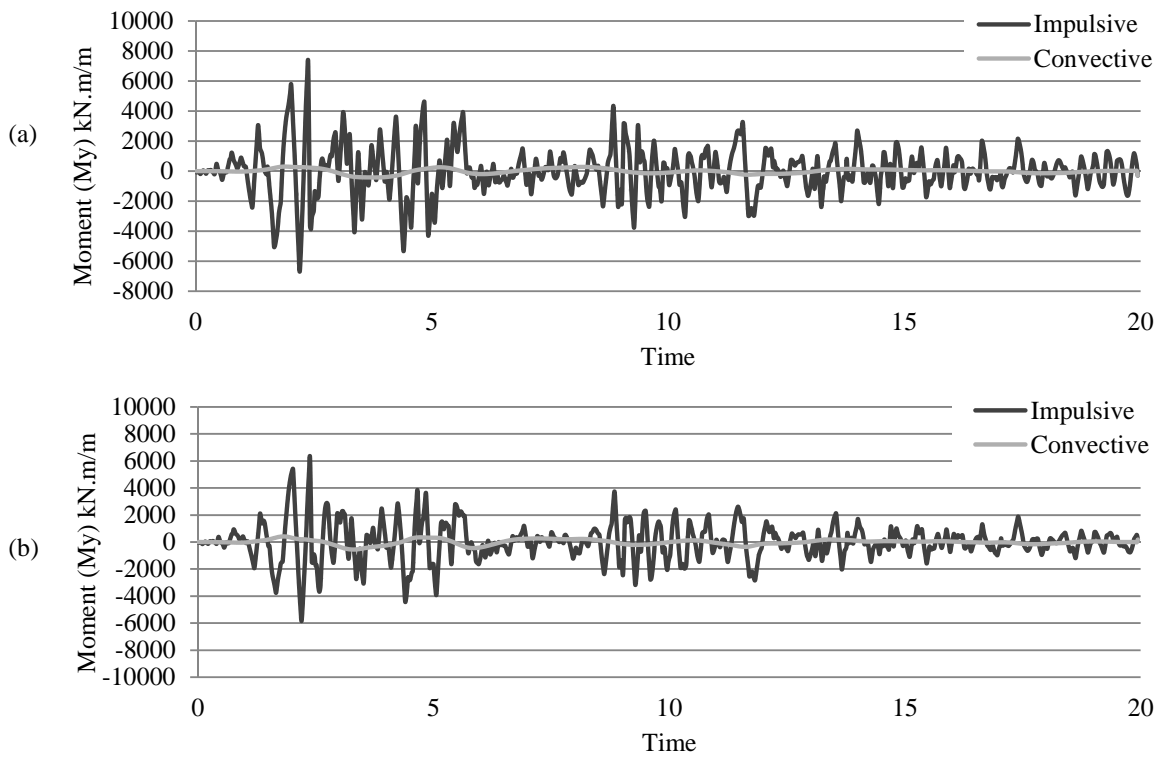


Figure 5.54: Time history of impulsive and convective component of moment ( $M_y$ ) of TX20Y60: (a) 3D model, (b) 2D model

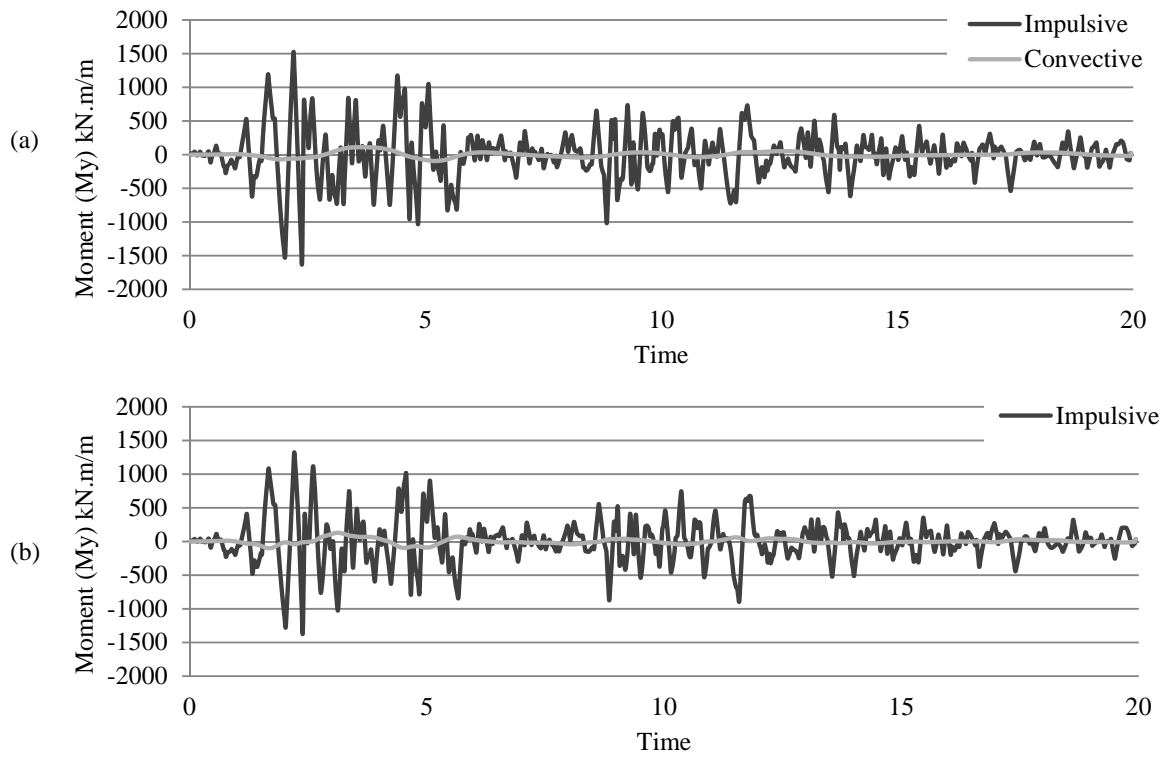


Figure 5.53: Time history of impulsive and convective component of moment ( $M_y$ ) of MX20Y60: (a) 3D model, (b) 2D model

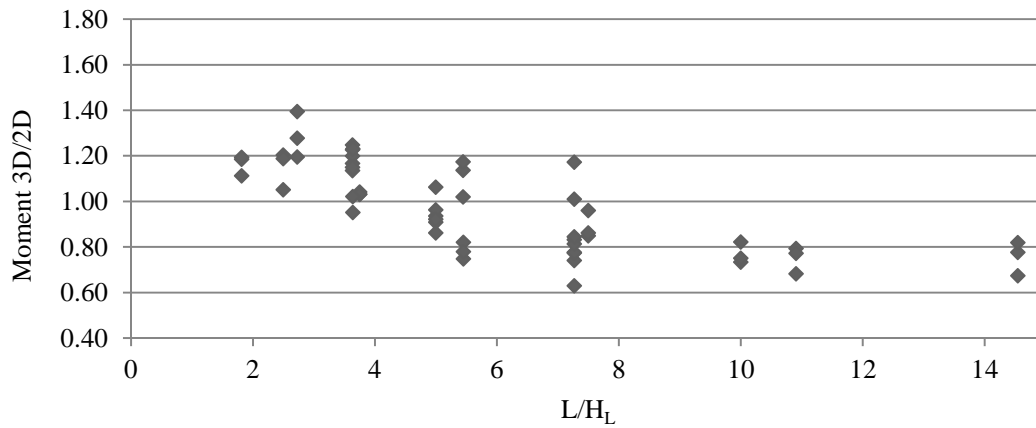


Figure 5.55: 3D/2D peak overturning moment against  $L/H_L$

# Chapter 6

## Summary, Conclusions, Recommendations and Future Studies

### 6.1 Summary

In spite of a wide range of studies on the dynamic response of the liquid containing structures, many design issues remain unsolved. Additional factors that need attention include; wall flexibility, three-dimensional geometry, direction and frequency content of the ground motion and the full time-domain simulation. It should be noted that, in the current practice, two-dimensional models are employed to estimate the dynamic response of the rectangular tanks. On the other hand, 3D modelling represents more realistic simulation of the tank behaviour. In this context, the primary objective of the present work is to investigate some of such effects to improve the design procedure of the seismically excited rectangular tanks.

Goals are set to find a simplified method to introduce the effect of three-dimensional geometry on the sloshing height and to introduce the effect of 3D geometry on the hydrodynamic pressure and structural responses. Moreover, goals are to investigate the effect of frequency content of the ground motion on the sloshing height. The result of the present work can be used for code applications.

In this study, flexibility of the wall is addressed to predict the dynamic response of 3D rectangular tanks. It should be noted that this study is limited to the linear elastic analysis of the open-top rectangular tanks that are anchored at the base and filled with water. In this study, tanks walls

are considered to have constant thickness over the height of the walls and the un-cracked section properties are used. It should be noted that the behaviour of tank with cracked section properties result in minor changes in convective terms and the sloshing behaviour is almost independent of the flexibility characteristics of the side walls. In this study, tanks are assumed to be rigidly attached to rock foundation and soil-structure interaction effect is ignored.

In this study, small wave amplitude or linear wave theory is used for evaluating the seismic performance of the LCS. However, there are some assumptions and limitations in this theory for simulating the actual behaviour of the sloshing. Note that the vertical component of the ground acceleration only causes insignificant effect on the surface elevation and hydrodynamic pressure; as a result, the effects of the vertical component of the ground motions are ignored in this study.

Parametric studies are conducted to investigate the effect of parameters such as tank plan dimensions, water depth and frequency content of the earthquake on the dynamic response of 3D tank models. The results of the modal analysis, as well as time history analysis of the rectangular tanks, are offered for twenty seven tank models. For time history analysis, tanks are subjected to the horizontal components of the 1940 El-Centro earthquake. It should be noted that the components of the ground motion are scaled in such a way to have the peak ground acceleration (PGA) of  $0.4g$  in N-S direction and  $0.27g$  in E-W direction and these components are applied in  $X$  and  $Y$  directions, respectively. To investigate the effect of the frequency content of the ground motion, three tank models are subjected to three different earthquake records, namely 1994 Northridge, 1940 El-Centro and 1957 San-Francisco earthquakes with identical PGA. In addition, eleven 3D tank models are subjected to a low frequency content earthquake record, namely 1994 Northridge, and the sloshing heights are calculated at the corners and are compared to the ones at the middle cross section of the walls.

For this purpose, finite element method is used to predict the response of the seismically excited rectangular water tanks. The finite element program, ANSYS, with fluid-structure interaction analysis capabilities is used for dynamic modal and time history analysis.

The natural frequencies of the first convective and impulsive mode of vibration are calculated for both 2D and 3D models. The sloshing heights calculated by 3D models are compared with the corresponding sloshing heights that are calculated by 2D models. The analysis results of the 2D and 3D models in the form of the hydrodynamic pressure and structural responses are discussed. Lateral hydrodynamic pressure distribution is also presented. A detailed comparison between current finite elements results and other methods and experimental results available in literature is given.

## 6.2 Conclusions

Based on the studies reported in this thesis, the following conclusions are drawn:

1. The natural frequencies of the first sloshing mode and the impulsive mode yield similar values for the 2D and 3D models. For the 2D models, comparison of the results from FEM and ACI code and potential function (PF) approach shows that the FE results are in a good agreement with the analytical value and ACI results for the convective component. The value of the convective mode period is slightly higher for the FEM as compared to ACI. This is due to flexibility of the wall. However, for the impulsive modes, discrepancies are observed before the results of FEM with the ACI 350.6-06 standard. This is also due to effect of wall flexibility for the coupled system considered in the proposed method.
2. Sloshing heights of the 3D models are higher in comparison with the 2D models. It is observed that this difference depends on factors such as tank plan dimensions and water level. If  $L$  and  $B$ , respectively, represent the length of the wall parallel and perpendicular to the direction of the ground motion and  $H_L$  the depth of the contained liquid; it is observed that the sloshing response is very sensitive to  $L/H_L$  ratio. However, as this ratio reaches the value of 10 and beyond, the sloshing response of the 2D tank model becomes very close to that of 3D tank model. It is observed that for the cases with  $L/H_L$  ratio smaller than 10, the sloshing height of the 3D model is higher than that of 2D models. For the cases with  $B/L$  ratio greater than 2.0, the response is 10% higher, and for the cases that  $B/L$  ratio is smaller than 2.0, the sloshing height in the 3D model is 20% higher than the 2D model.
3. Sloshing height at the corner of the 3D tanks found to be much higher than other locations. This is due to interaction of the waves formed in  $X$  and  $Y$  directions. The amplification of the wave at the corner of the tank relative to those at the middle of the walls found to be very sensitive to tank plan dimensions and water level. Comparing the results of the sloshing heights of 27 tank models subjected to an intermediate frequency content earthquake record such as 1940 El-Centro earthquake, it is found that the maximum sloshing at the corner of the rectangular tank is up to 60% higher than the greater value of the peak sloshing height at the middle of the shorter side or longer side walls. In the 3D models, it is found that the amplification of the sloshing height at the corner relative to the sloshing height at the middle of the wall is sensitive to the tank plan dimension. For the cases with  $B/L$  ratio greater than 2.0, the response at the corner is amplified up to 40%. Also, for the cases with  $B/L$  ratio smaller than 2.0, the response is amplified up to 60%.

4. It was observed that the sloshing height at the middle of the wall is very sensitive to the frequency content of the ground motion. For the records of the identical peak acceleration, higher sloshing height occurred when the centre of gravity of the power spectrum function is located at lower frequency and closer to the natural frequency of the sloshing mode.
5. It is found that the occurrence of constructive wave interference at the corner of the tank is sensitive to frequency content of the ground motion. When the low frequency content earthquake record is applied, at the time that the peak sloshing happens at the corner of the tanks, the sloshing height at the corner of the tank is almost 100% higher than that at the middle of the wall for shallow height tank models. The amplification is found to be 71% and 75% for the medium height and tall height tank models, respectively. It was observed that, for the low frequency ground motion with the high energy pulse, the amplification of the sloshing height at the corner of the tank, relative to the middle of the wall is more profound. For those cases, the sloshing height at the corner of the tank can be calculated by summation of the peak sloshing heights in  $X$  and  $Y$  directions that are obtained from the 3D models. Note that in this study, only a limited number of tank models are subjected to the low frequency ground motion, and then a method is recommended for calculating the sloshing height at the corner of such models. However, this method is conservative for deeper tanks.
6. The hydrodynamic pressure along the height of the flexible walls tend to be amplified due to 3D geometry. The effect of the 3D geometry is more significant on impulsive behaviour of the tall tank models in comparison with the shallow tank models; also, it is very sensitive to  $L/H_L$  ratio. The peak hydrodynamic pressure along the height of the tank wall is amplified up to 46%. It is also observed that the hydrodynamic pressure changes in the longitudinal direction, as well. It is observed that when the tank wall is subjected to ground motion perpendicular to its plane, the pressure at a location closer to the corner is lower than the pressure at the middle of the wall.
7. The 3D geometry may cause a significant increase in time domain response of the structure. Structural reactions of the 3D model are found to be greater than that for the 2D models. For tanks with  $B/L$  ratio smaller than 1, the amplification is up to 50%, and for the tanks with  $B/L$  ratio greater than 1, it is 30%. In other words, it is observed that the 2D models, significantly, underestimate the base shear parallel to the long side walls as compared with 2D models.

## 6.3 Code Recommendations

In order to consider the effect of three-dimensional geometry, the amplification coefficient  $\alpha$ , can be applied to the sloshing height obtained from 2D model:

- For  $B/L \geq 2.0$  and  $L/H_L \geq 10.0$ ,  $\alpha = 1.0$
- For  $B/L \geq 2.0$  and  $L/H_L < 10.0$ ,  $\alpha = 1.2$
- For  $B/L < 2.0$  and  $L/H_L < 10.0$ ,  $\alpha = 1.3$

From the results of the sloshing heights of the rectangular water tanks subjected to the El-Centro earthquake, it is concluded that in order to calculate the peak sloshing height at the corner of a rectangular tank, amplification coefficient  $\beta$ , can be applied to the sloshing heights conducted from the 2D models. Note that the coefficient,  $\beta$ , shall be applied to the greater value of the sloshing in  $X$  and  $Y$  directions:

- For  $B/L \geq 2.0$ ,  $\beta = 1.3$
- For  $B/L < 2.0$ ,  $\beta = 1.5$

The coefficient  $\beta$  is applicable to the results of the sloshing heights calculated according to ACI 350.5-06 code for seismic design of liquid containing concrete structures. The ACI sloshing heights should be amplified by the corresponding amplification coefficient  $\alpha$  to consider the effect of 3D geometry.

It is observed that when similar low frequency excitations, with identical acceleration and frequency content, are applied in  $X$  and  $Y$  directions, the sloshing height at the corner of some tanks is almost 100% higher than the sloshing heights at the middle of the walls. For these cases, a conservative method to estimate the peak sloshing height at the corner of the rectangular tanks is to use the summation of the peak sloshing heights in  $X$  and  $Y$  directions.

## 6.4 Future Studies

In this study, a limited number of parameters are investigated. Other studies can be carried out to investigate the effects of parameters such as liquid properties, as well as variation of the tank

wall thickness over the wall height.

In this study, only a limited number of tank models are subjected to the low frequency ground motion, and then a method is recommended for calculation of the sloshing height at the corner of such models. However, the method is conservative for deeper tanks. In future studies, more tank models can be developed and analyzed in order to develop a more detailed comparison.

Since this study is based on linearized wave theory, the effect of non-linear sloshing wave can also be considered in the future work. A nonlinear surface boundary condition will lead to more accurate results beyond the parameters used in current study.

Moreover, the effect of soil-structure interaction can be investigated. Also, additional tank models with top roofs can be studied to simulate the resulting pressure on tank roofs due to impact of the free surface sloshing.

# Bibliography

ACI 350.3-06. (2006). Seismic design of liquid-containing concrete structures (ACI 350.3-06) and commentary (350.3R-06). American Concrete Institute (ACI) Committee 350, Environmental Engineering Concrete Structures, Farmington Hills, Mich.

American Lifelines Alliances, (2004). Seismic Design Standards for Above ground Steel Storage Tanks, Federal Emergency Management Agency (FEMA) and the American Society of Civil Engineers (ASCE).

American Society of Civil Engineering (ASCE). (2005). Minimum design loads for buildings and other structures, ASCE Standard ASCE/SEI 7-05

Anrade W.P. (1999). Implementation of second order absorbing boundary condition in frequency domain computations, PhD Thesis. Texas: The University of Texas of Austin.

Anshel J.S. (1999). Kobe earthquake of January 17, 1995. Lifeline performance, ASCE Publication.

ANSYS Inc. ANSYS help manual (Version 11.1). (2004). Global headquarters, Southpointe, 275 Technology drive, Canonsburg, PA 15317

ANSYS Inc. ANSYS software (Version 12.1). (2010). Global headquarters, Canonsburg, Pennsylvania.

Bathe, K. J. (1996). Finite Element Procedures, Prentice-Hall, Englewood Cliffs.

Bowles, J.E. (1996). Foundation analysis and design. McGraw-Hill International Editions, 5th ed. Civil Engineering Series.

Clough, R.W. and Tocher, J.L. (1965). Finite element stiffness matrices for analysis of plate bending, Conference on Matrix Methods in Structural Mechanics, AFFDL-TR-66-80.

- Cho, K.H., Kim, M.K. and Lim, M.Y. (2004). Seismic responses of base-isolated liquid storage tanks considering fluid-structure-soil interaction in time domain, *Soil Dynamics and Earthquake Engineering*, **24**: 839-852
- Cho, J.R., Lee, H.W. and Ha, S.Y. (2005). Finite element analysis of resonant sloshing response in 2-D baffled tank, *Journal of Sound and Vibration*, **288**:5,829–845.
- Doganun, A. ,Durmus, A. and Ayvaz, Y. (1997). Earthquake analysis of flexible rectangular tanks using the lagrangian fluid finite element, *Euro. J Mech.-A/Solids*, **16**,165-182
- Eurocode 8. (1998). Design provisions for earthquake resistance of structures, European committee for standardization, Brussels
- Fox, D. W. and Kuttler, J. R. (1983). Sloshing Frequencies, *Journal of Applied Mathematics and Physics*. **34**,668-696.
- Ghaemian, M. and Ghobarah, A. (1997). Nonlinear seismic response of concrete gravity dams with dam-reservoir interaction, *Journal of engineering structures*, **21**:4,306-315
- Ghaemian, M. (1998). Staggered solution schemes for dam-reservoir interaction, *Journal of Fluids and Structures*
- Ghaemmaghami, A.R. and Kianoush, M.R. (2009). Effect of wall flexibility on dynamic response of concrete rectangular tanks under horizontal and vertical ground motions. *ASCE Journal of Structural Engineering*, **136**:4,441-450
- Haroun, M.A. and Housner, G.W. (1981). Earthquake response of deformable liquid storage tanks, *Journal of Applied Mechanics, ASME*, **48**,411–418.
- Haroun, M.A. (1983). Vibration Studies and Tests of Liquid Storage Tanks. *Earthquake Engineering and Structural Dynamics*, **11**,190-206.
- Haroun, M.A. (1984). Stress Analysis of Rectangular Walls under Seismically Induced Hydrodynamic Loads. *Bulletin of the Seismological Society of America*, **74**(3),1031-1041.
- Haroun, M.A. and Ellaithy, M.H. (1985). Seismically induced fluid forced on elevated tanks, *Journal of Technical Topics in Civil Engineering*, **111**,1-15
- Haroun, M.A. and Tayel, M.A. (1985). Response of tanks to vertical seismic excitations, *Earthquake Engineering and Structural Dynamics*, **13**,583–595.

- Haroun, M.A. and Abou-Izzeddine, W. (1992). Parametric study of seismic soil–tank interaction. I: horizontal excitation, *ASCE Journal of Structural Engineering*, **118:3**,783–797.
- Hoskins, L.M. and Jacobsen, L.S. (1934). Water pressure in tank caused by a simulated earthquake, *Bulletin of the seismological society of America*, **24:1**,21-34
- Housner, G.W. (1957). Dynamic pressure on accelerated fluid containers, *Bulletin of the seismological society of America*, **47:1**,15-37
- Housner, G.W. (1963). The dynamic behaviour of water tanks, *Bulletin of the Seismological Society of America*, **53:2**,381–387.
- Ibrahim, R.A. 2005. Liquid sloshing dynamics. Cambridge University Press.
- Jaiswal, O.R., Rai, D. and Jain S.K. (2004). Review of Code Provisions on Seismic Analysis of Liquid Storage Tanks, Indian Institute of Technology Kanpur, IITK-GSDMA-EQ04-V1.0
- Jennings, P.C. and Kuroiwa, J.H. (1968). Vibration and soil-structure interaction tests of a ninestory reinforced concrete building, *Bulletin of Seismological Society of America*, **58**,891-916
- Karamanos S.A., Patkas, L.A. and Platyrrachos, M.A. (2006). Sloshing effects on the seismic design of horizontal-cylindrical and spherical industrial vessels, *ASME J. of Pressure Vessel Technology*, **128:3**,328-340.
- Kawasumi, H. (1968). General Report on the Niigata Earthquake of 1964, Tokyo Electrical Engineering College Press, Tokyo, Japan.
- Kianoush, M.R., and Chen, J.Z. (2006). Effect of vertical acceleration on response of concrete rectangular liquid storage tanks, *Engineering Structures*, **28:5**,704–715.
- Kianoush, M.R., Mirzabozorg, H. and Ghaemian, M. (2006). Dynamic Analysis of Rectangular Liquid Containers in Three-Dimensional Space, *Canadian Journal of Civil Engineering*, **33**:501-507
- Kim, J.K., Koh, H.M. and Kwahk, I.J. (1996). Dynamic response of rectangular flexible fluid containers, *ASCE Journal of Engineering Mechanics*, **122:9**,807–817.
- Koh, H.M., Kim, J.K. and Park, J.H. (1998). Fluid–structure interaction analysis of 3D rectangular tanks by a variationally coupled BEM–FEM and comparison with test results, *Earthquake Engineering and Structural Dynamics*, **27**,109–124.

- Livaoglu, R. (2008). Investigation of seismic behaviour of fluid-rectangular tank-soil/foundation systems in frequency domain, *Soil Dynamics and Earthquake Engineering*, **28:2**,132-146.
- Lysmer J, and Kuhlmeyer R.L. (1969). Finite dynamic model for infinite media, *ASCE. Eng Mech Div J*, **95**,859–77.
- Mikishev, G.N. and Dorozhkin, N.Y. (1961). An experimental investigation of free oscillations of a liquid in containers, *Izvestiya Akademii Nauk SSSR, Otdelenie Tekhnicheskikh Nauk, Mekhanika I Mashinostroenie*, **4**,48–83.
- Mcverry, G.H. (1979). Frequency domain identifications of structural models from earthquake records. Report No. EERL 79-02, California Institute of Technology.
- Minowa C. (1980). Dynamic analysis for rectangular water tanks. *Recent Advances in Lifeline Earthquake Engineering in Japan*, 135–142.
- Minowa C. (1984). Experimental studies of seismic properties of various type water tanks. *In: Proceedings of eighth WCEE*, San Francisco: 945–52.
- Mirzabozorg, H., Khaloo, A.R. and Ghaemian, M. (2003). Staggered solution scheme for three-dimensional analysis of dam reservoir interaction, *Dam Engineering*, **14:3**,147–179.
- Modi, V.J. and Akinturk, A. (2002). An efficient liquid sloshing damper for control of wind-induced instabilities, *Journal of Wind Engineering and Industrial Aerodynamics*, **90**,1907–1918.
- Munshi, J.M. (2002). Design of liquid-containing concrete structures for earthquake forces, Portland Cement Association, ISBN 0-89312-219-X.
- NASA special publications. (1966). The dynamic behaviour of liquid in moving containers. NASA SP-106, Washington, D.C.
- National Research Council (U.S.). (1968). The great Alaska earthquake of 1964, Committee on the Alaska Earthquake , Volume 1, Part 1, 285.
- NBC. (2010). National Building Code of Canada. Institute for Research in Construction, National Research Council of Canada, Ottawa, Ontario.
- New Zealand Standards Association. (2010). NZS3106: The New Zealand Code of Practice for Concrete Structures for the Storage of Liquids.

- Noji T., Yoshida H., Tatsumi E., Kosaka H. and Hagiuda H. (1988). Study on vibration control damper utilizing sloshing of water, *Journal of Wind Engineering and Industrial Aerodynamics*, **37**,557– 66.
- Panigrahy, P.K., Saha, U.K. and Maity, D. (2009). Experimental studies on sloshing behaviour due to horizontal movement of liquids in baffled tanks, *Ocean engineering*, **36**,213-222
- Park, J.H., Koh, H.M. and Kim, J. (1992). Liquid–structure interaction analysis by coupled boundary element – finite element method in time domain. *In Proceedings of the 7th International Conference on Boundary Element Technology*, Albuquerque, New Mexico, 1992. Edited by C.A. Brebbia and M.S. Ingber. Computational Mechanics Publication BE-TECH/92, Computational Mechanics Publications, Southampton, UK. 89–92.
- Patkas, L.A. and Karamanos S.A. (2007). Variational solutions for externally induced sloshing in horizontal-cylindrical and spherical vessels, *ASCE J. of Engineering Mechanics*, **133**:6, 641-655.
- Rai, D.C. (2002). Seismic retrofitting of R/C shaft support of elevated tanks. *Earthquake Spectra*, **18**: 745-760
- Rashed, A.A. and Iwan W.D. (1984). Hydrodynamic pressure on short-length gravity dams, *ASCE Journal of Engineering Mechanics*, **110**:9,1264-1283
- Seed, H.B. and Lysmer, J. (1975). Soil-structure interaction analysis for seismic response, *ASCE Journal of Geotechnical Engineering*, **102**:6,439-457
- Sezen, H. and Whittaker, A.S. (2006). Seismic performance of industrial facilities affected by the 1999 Turkey earthquake, *ASCE Journal of Performance of Constructed Facilities*, **20**:1,28-36
- Song C.H. and Wolf J.P. (1994). Dynamic stiffness of unbounded medium based on solvent damping extraction method. *Earthquake Engineering and Structural Dynamics*, **23**,1073–86.
- Stover, C.W. and Coffman, J.L. (1993). U.S. Geological Survey Professional Paper 1527, United States Government Printing Office, Washington.
- Subhash, S. and Bhattachryya, S.K. (1996). Finite element analysis of fluid-structure interaction effect on liquid retaining structures due to sloshing, *Computers and Structures*, **59**:6,1165- 1171.
- Sung, T.Y. (1953). Vibrations in semi-infinite solids due to periodic surface loading, *ASTM STP*. **156**,35-68

Tavakkoli Avval, I., Kianoush M.R. and Ghaemmaghami A.R. (2012). Sloshing Characteristic of Rectangular Concrete Tanks under Seismic Loading, *Proc. 3rd Int. Struc. Speciality Conference*, Edmonton, Alberta

United Nations International Strategy for Disaster Reduction (UNISDR) (2004). Living with risk: a global review of disaster reduction initiatives, UNISDR, 17-18

U.S. Geological Survey. (2012). Official website, [www.USGS.gov](http://www.USGS.gov), USGS Headquarters, Virginia.

Veletsos, A.S. and Tang, Y. (1986). Dynamics of vertically excited liquid storage tanks, *ASCE Journal of Structural Engineering*, **112:6**,1228–1246.

Veletsos, A.S. and Yang, J.Y. (1977). Earthquake response of liquid storage tanks, advances in civil engineering through mechanics, *ASCE Proceedings of the second engineering mechanics specially conference*, Raleigh, NC: 1-24.

Veletsos, A.S. and Shivakumar, P. (1997). Tanks containing liquid or solids. A handbook in computer analysis and design of earthquake resistant structures. Computational mechanical publications: 725-774

Virella, J.C., Prato, C.A. and Godoy L.A. (2008). Linear and nonlinear 2D finite element analysis of sloshing modes and pressure in rectangular tanks subjected to horizontal harmonic motions, *Journal of Sound and Vibration*, **312:3**,442-460

Warburton, G.B. (1982). Optimum absorber parameters for various combinations of response and excitation parameters, *Earthquake Engineering and Structural Dynamics*, **10**,381–401.

Westergaard, H.M. (1938). Water pressure on dams during earthquakes, *American society of civil engineers*. **98**,418-433

Wilson E.L. (2002). Three-dimensional static and dynamic analysis of structures- a physical approach with emphasis on earthquake engineering, 3rd Edition, Berkeley, California, USA: Computers and Structures, Inc.

Wolf J.P., and Song C.H. (1995). Doubly asymptotic multi-directional transmitting boundary for dynamic unbounded medium-structure-interaction analysis, *Earthquake Engineering and Structural Dynamics*, **24:2**,175-188

Wolf J.P. and Song C.H. (1996). Finite element modeling of unbounded media, *The 11th world*

*conference on earthquake engineering*, San Francisco 1996, **70**,1-9.

Yang, J.Y. (1976). Dynamic behaviour of fluid–tank systems. PhD. thesis, Department of Civil Engineering, Rice University, Houston, Tex.

Zienkiewicz, O. C. (1977). *The Finite Element Method*, McGraw-Hill Company, London.